CHALMERS

Design of Rim Driven Waterjet Pump for Small Rescue Vessel

Master's Thesis in Nordic Master in Maritime Engineering

Thor Peter Andersen

Department of Shipping & Marine Technology
Division of Marine Design
Chalmers University of Technology

Department of Mechanical Engineering
Division of Fluid Mechanics, Coastal and Maritime Engineering
The Technical University of Denmark

Gothenburg, Sweden 2014
Master's Thesis 2014:6

This page is intentionally left blank.

MASTER'S THESIS IN THE NORDIC MASTER IN MARITIME ENGINEERING

Design of Rim Driven Waterjet Pump for Small Rescue Vessel

Thor Peter Andersen

Department of Shipping and Marine Technology
Division of Marine Design
Chalmers University of Technology
Gothenburg, Sweden 2014

.

Design of Rim Driven Waterjet Pump for Small Rescue Vessel

Thor Peter Andersen

Master's Thesis, X-14/302

Department of Shipping and Marine Technology
Division of Marine Design
Chalmers University of Technology
SE-412 96 Gothenburg
Sweden
Telephone: +46 (0)31-772 1000

Gothenburg, Sweden 2014

Design of Rim Driven Waterjet Pump for Small Rescue Vessel
Master's Thesis in the Nordic Master in Maritime Engineering
Thor Peter Andersen
Department of Shipping and Marine Technology
Division of Marine Design
Chalmers University of Technology
&
Department of Mechanical Engineering
Division of Fluid Mechanics, Coastal and Maritime Engineering
The Technical University of Denmark

Abstract

The hydrodynamic design and performance analysis of a pump with an electromagnetic rim driven impeller and with an open centerline is performed. The pump is the driving force of a waterjet system for a small rescue vessel. The rim-engine driving the pump is already developed and generates dimensional constraints for the pump design. The purpose of the open centerline is to avoid entanglement, and thereby downtime, if ropes are sucked into the system. The rescue boat is used to tow multiple life rafts and a high bollard pull force of 4 kN is therefore required, a top speed of approximately 20 knots is desired. The design work have been carrier out using TurboDesign1 and the performance is analysed using computational fluid dynamics, specifically Menters SST $k-\omega$ turbulent flow model in Ansys Fluent. Three pump configurations are analysed and compared in order to study the effect of the open centerline and if a pump design without guide vanes is feasible. The performance analysis shows that a pump without guide vanes is unable to provide the required thrust and thereby not feasible. The thesis concludes that the final concept design for the rim driven hubless pump is able to deliver the force needed to reach a top speed of 25 knots. The required force for the bollard pull condition is, however, not achieved due to cavitation in the pump. A maximum efficiency of approximately 70% is reached. This is an acceptable efficiency, but it is low compared to similar standard waterjet pumps. The low efficiency reduces the cavitation properties of the pump, compared to regular pumps with similar dimensions, as the loading of the blades must be higher to achieve a force production similar to a standard pump. A goal of the future work should be to improve the cavitation properties of the system. There are several ways to improve the cavitation properties, however, the most efficient measure is a redesign of the inlet duct and an increased impeller diameter, meaning a redesign of the electromagnetic engine driving the pump.

This page is intentionally left blank.

Design of Rim Driven Waterjet Pump for Small Rescue Vessel
Master's Thesis in the Nordic Master in Maritime Engineering
Thor Peter Andersen
Department of Shipping and Marine Technology
Division of Marine Design
Chalmers University of Technology
&
Department of Mechanical Engineering
Division of Fluid Mechanics, Coastal and Maritime Engineering
The Technical University of Denmark

Resume

I denne afhandling er det hydrodynamiske design af en rem dreven pumpe med åben centerlinje fuldført. Endvidere er en analyse af ydeevnen udført.

Pumpen skal drive et waterjet system på et mindre hurtiggående redningsfartøj. Pumpen designes til en nyudviklet elektromagnetisk remmotor. Formålet med den åbne centerlinje er at undgå at reb vikler sig ind i pumpen i tilfælde af at dette suges ind i systemet. Derved undgås downtime på grund af reb i pumpen. Redningsfartøjet skal kunne trække op til flere sammentøjrede redningsflåder, derfor er en høj trækkraft ved lav fart en nødvendighed. Pumpen designes derfor således, at en trækkraft på 4 kN produceres af waterjet systemet. Tophastigheden skal mindste være 20 knob. Designet af pumpen er udført ved brug et pumpe design software kaldet TurboDesign1 og analysen af pumpens ydeevne er udført ved hjælp af numerisk fluid mekanik, specifikt ved brug af Menters SST $k-\omega$ turbulens model i Ansys Fluent. Tre forskellige konfigurationer af pumpen er testet for at undersøge effekten af at have en åben centerlinje, og om det er muligt at opnå en acceptabel ydeevne med et design uden statorblade. Analysen af ydeevnen viser, at en pumpekonfiguration uden statorblade ikke kan producere den nødvendige trækkraft. Det konkluderes at redningsfartøjet kan opnå en hastighed omkring 25 knob ved brug af det endelige konceptuelle design. Resultaterne viser dog, at den nødvendige trækkraft ikke opnås, da pumpen oplever kavitation i denne tilstand. En maksimal effektivitet på omkring 70% er opnå et med det endelige pumpe design. Dette er en acceptabel effektivitet på trods af at den er lav sammenlignet med en standard waterjet pumpe af samme dimensioner. Den lave effektivitet er imidlertid grunden til, at pumpen opleves store kavitationsudfordringer når den maksimale trækkraft skal opnås. Pumpebladene skal belastes hårdere for at producere den samme trækkraft som en standard pumpe, og der opleves derfor mere kavitation ved denne tilstand. Det fremtidige arbejde indebær en forbedring af pumpen, således at kavitation ikke er et udslagsgivende problem for den maksimale trækkraft. Pumpedesignet kan ændres på flere punkter, men en ændring af pumpens diameter er den mest effektive metode til at opnå den ønskede effekt. Dette vil dog medføre en konstruktionsændring af den remdrevne motor, der driver pumpen.

This page is intentionally left blank.

Preface

This master thesis is the final project of Thor Peter Andersen on the master study program Nordic Master in Maritime Engineering at the Technical University of Denmark (DTU) and Chalmers University of Technology. The project is carried out at Chalmers: Department of Shipping and Marine Technology, in cooperation with DTU Department of Mechanical Engineering and Rolls-Royce AB, Kristinehamn.

This thesis consist of a significant amount of coloured figures, it is therefore recommended to be read in a coloured version.

Acknowledgements

Supervisors

Rickard Bensow, Chalmers Shipping and Marine Technology

For supervising within hydrodynamics and thesis structure.

Poul Andersen, DTU Mechanical Engineering

For supervising within hydrodynamics and thesis structure.

Reima Aartojärvi, Rolls-Royce AB Kristinehamn

For supervising within waterjet pump design and hydrodynamics.

Others

Urban Svennberg, Rolls-Royce AB Kristinehamn

For great help in setting up and understanding the required CFD analyses.

Fredrik Falkman, The Swedish Sea Rescue Society

For providing an interesting project and information about the operation of the rescue boat.

Thor Peter Andersen, Gothenburg 2014/05/28

This page is intentionally left blank.

Contents

1 Introduction **1**
- 1.1 Background . . . 1
- 1.2 Objective . . . 2
  - 1.2.1 Technical Specifications . . . 3
- 1.3 Method . . . 4
- 1.4 Limitations . . . 5
- 1.5 Changes form a Regular to a Rim Driven Waterjet Pump. . . . 6
- 1.6 Outline of the Thesis . . . 8

2 The Rescue Boat **9**
- 2.1 Thrust Prediction . . . 10

3 The Waterjet Propulsion System **13**
- 3.1 Processes of The Waterjet System . . . 13
- 3.2 Thrust . . . 14
- 3.3 The Pump . . . 15
  - 3.3.1 The Pump Configuration Cases . . . 16

4 The Design Process **17**

5 Design Tools and Methods **21**
- 5.1 TurboDesign1 . . . 21
  - 5.1.1 Potential Flow Theory . . . 21
  - 5.1.2 Design Parameters . . . 22
- 5.2 Computational Fluid Dynamics Analysis . . . 23
  - 5.2.1 Steady State Analysis . . . 23
  - 5.2.2 Transient Analysis . . . 23
  - 5.2.3 SST $k-\omega$ Turbulent Flow Model . . . 24
  - 5.2.4 Mixture Flow Model . . . 24
  - 5.2.5 Schemes . . . 24

5.2.6 Solver Algorithm . . . 25
5.2.7 The Computational Mesh . . . 25
5.2.8 y-plus . . . 25
5.2.9 Convergence . . . 25
5.2.10 The CFD Code - Ansys Fluent . . . 26
5.2.11 Postprocessing . . . 26

6 Energy Model **27**
6.1 Assumptions . . . 27
6.2 The Model . . . 28
6.2.1 The Head Losses . . . 30
6.3 Key Results . . . 33
6.3.1 Maximum Efficiency Prediction . . . 35
6.3.2 Engine Load . . . 35
6.4 Discussion of Model . . . 36

7 Steady Flow CFD Pump Model **37**
7.1 The Computational Grid . . . 38
7.1.1 Simplified Grid Dependency Study . . . 38
7.2 Boundary Conditions . . . 40
7.3 Calculation Settings . . . 40
7.4 Discussion of the Model . . . 41

8 Transient Flow CFD Pump Model **43**
8.1 The Computational Grid . . . 44
8.2 Boundary Conditions . . . 44
8.3 Calculation Settings . . . 45
8.4 Multiphase Flow Model . . . 46
8.4.1 Settings . . . 46
8.5 Discussion of the Model . . . 47

9 Blade and Pump Design **49**
9.1 Constant Design Parameters . . . 49
9.1.1 The Meridional Channel Shape . . . 49
9.1.2 The Thickness Distribution . . . 50
9.1.3 Fluid Properties and Design Specifications . . . 51
9.1.4 Number of Blades . . . 53
9.2 Non-Constant Design Parameters . . . 53
9.2.1 Vorticity Distribution . . . 53
9.2.2 Blade Loading . . . 54
9.2.3 Stacking Condition . . . 56
9.3 Leading and Trailing Edge Modification . . . 56
9.4 The Final Pump Concept . . . 57

10 Performance of the Final Pump Concept **59**
10.1 Convergence Study 59
10.2 Performance Results 61
10.2.1 The Efficiency Definition 62
10.2.2 Steady Analysis 64
10.2.3 Transient Analysis 73
10.2.4 Cavitation Analysis 78
10.3 Discussion 81
10.4 Rope in Pump Discussion 82

11 Conclusion **85**
11.1 Future Work 86

Bibliography **90**

A Savitsky's Thrust Prediction Method **91**

B Mathematical Model Matlab Script **95**

C Meshing Settings **103**

D CFD Convergence Study **107**

This page is intentionally left blank.

List of Figures

1 Illustration with key pump expressions. xiii
2 Illustration with key blade expressions. xiii

1.1 The figure contains a picture of the issue with rope entanglement (figure 1.1a) and a picture of a rim driven hubless thruster (1.1b). 2
1.2 Comparison of regular waterjet (figure 1.2a) and the Rim-Jet (figure 1.2b). 6

2.1 The initial boat design. 9
2.2 The thrust curve produced by the Savitsky prediction method and the same curve corrected with a 20% seamargin. 11
2.3 Trim curve produced by the Savitsky prediction method. 11

3.1 Waterjet principle model: Point 0. Free stream, Point 1. Stream tube inlet, Point 2. Duct inlet, Point 3. Pump inlet, Point 4. Pump center Point 5. Pump outlet, Point 6. Nozzle outlet and Point 7. Jet minimum diameter. 13
3.2 Comparison of regular waterjet (figure 1.2a) and the Rim-Jet (figure 1.2b). 15
3.3 Sketches of the three pump cases. 16

4.1 Illustration of the iterative design process. 17

5.1 Meridional plot of the channel shape. The hub is included as it is a requirement for the input to TD1. 22

6.1 Waterjet principle model: Point 0. Free stream, Point 1. Stream tube inlet, Point 2. Duct inlet, Point 3. Pump inlet, Point 4. Pump center Point 5. Pump outlet, Point 6. Nozzle outlet and Point 7. Jet minimum diameter. 27
6.2 Plot of the inlet loss factor polynomial. 32
6.3 Plot specifying the head rise required to produce the necessary thrust. . 34
6.4 Plot of performance prediction for pumps of varying type. Source: [Brennen, 1994, p32, figure 2.8]. 35

7.1 Steady flow simulation set-up. Blue: Stationary walls. Green: Rotating impeller blade and shroud. Yellow: Free flow pipe. 37
7.2 example of computational domains. 38
7.3 Example of computational mesh. 39

8.1 Unsteady flow analysis set-up. 43
8.2 The figure visualises the mesh used for the transient analysis of the unsteady flow through the pump. 44

9.1 Meridional plot of the channel shape. The hub is included as it is a requirement for the input to TD1. 50
9.2 Plot of the thickness distribution in three spanwise positions. The leading and trailing edge is modified at a later stage. 51
9.3 The contour figure showing the axial velocity field entering the guide inlet. The orange blade is a guide vane and the grey is the nozzle wall. The direction of the look into the pump is upstream. 52
9.4 Vorticity distribution for the impeller and guide vane blade. 54
9.5 Plot of the resulting blade loading for the impeller blade. 55
9.6 Plot of the resulting blade loading for the guide vane. 55
9.7 Figure explaining the use of the edge defining ratio. source: [TD1, 2012b] 56
9.8 The impeller blade and guide vane blade with modified leading and trailing edges are shown free and in connection with the final pump Case 1. configuration. The rotation of the impeller follows the right hand rule around the z-axis (blue arrow in the right hand corner of figure 9.8c). . . 57

10.1 Plot of convergence study of Case 1. It is evident from the figure that the torque of the system is constant though with small fluctuations. Please note that this figure is based solely on the last 200 iterations displayed. . 60
10.2 Computational history for the bollard pull condition. 61
10.3 The three pump configurations are displayed in 3D. The rotation is following the right hand rule for the flow direction (towards the nozzle). Note that the impeller is upstream of the guide vanes. 62
10.4 Plot of the produced head rise and axial efficiency at given flow rates for the case 1 pump configuration. 65
10.5 Figure 10.5a displays head rise produced and required. Figure 10.5b display the torque requirements and the maximum limit 67
10.6 Picture of Case 3. pump configuration with the pressure distribution as contours. 67
10.7 Figure 10.7a displays total impeller efficiency of the impeller for Case 1. and 3. Figure 10.7b displays axial impeller efficiency of the impeller for Case 1. and 3. 68
10.8 Case 1. pressure at the pump inlet (point 3 figure 3.1). The pressure is given relative to atmospheric pressure, here the vapour pressure is $-99\,\mathrm{kPa}$. 70

10.9 Figure 10.9a and 10.9b displays the results of the CFD evaluation of the pump (Case 1.) operating at the two points of equilibrium. 70

10.10The pressure distribution of the Case 1. pump configuration at the two points of head rise equilibrium. 71

10.11Plot of the produced head rise and axial efficiency at given flow rates for the transient analysis of Case 1. 73

10.12The fluctuating pressure in the pump is apparent, especially at the guide vane. 74

10.13Figure 10.13a displays the head rise production. Figure 10.13b displays torque requirements. 75

10.14Figure 10.14a displays the total impeller efficiency. Figure 10.14b displays axial efficiency. 76

10.15The backflow observed in the operational points of low flow rate is visualized. 77

10.16The fluctuating pressure in the pump is visual, especially at the guide vane. 79

10.17The fluctuating pressure in the pump is visual, especially at the guide vane. 80

10.18Figure of the flow through the pump at the bollard pull condition with steamlines visualizing the flow through the pump. Note the swirl in the centerline. The figure is based on the transient cavitation analysis. 82

C.1 Grid settings for the general mesh sizing. 104

C.2 Grid settings for the inflation layer. 105

C.3 Grid settings for the face sizing on the blade. 105

D.1 Plot of convergence study of Case 1. It is clear from the figure that the torque of the system is constant with minor fluctuations. 108

D.2 Plot of convergence study of Case 2. It is clear from the figure that the torque of the system is constant with minor fluctuations. 108

D.3 Plot of convergence study of Case 3. It is clear from the figure that the torque of the system is constant with minor fluctuations. 109

D.4 Plot of convergence study of Case 1. transient analysis. The x-axis displays the time steps the study is based on. The actual number of time steps is displayed in table D.2 109

D.5 Plot of convergence study of Case 1. transient cavitation analysis. Note that the $Q_e = 1.09$ condition is not converged fully. 110

This page is intentionally left blank.

List of Abreviations

TD1	TurboDesign1
CFD	Computational Fluid Dynamics
SSRS	Swedish Sea Rescue Society
LOA	Length over all
BP	Planning breath
LCG	Longitudinal center of gravity
LCB	Longitudinal center of buoyancy
SOLAS	Safety of Life at Sea

This page is intentionally left blank.

Notations

Greek letters

ξ	Inlet loss factor
ρ	Density of fresh water at 20°
μ	Viscosity of fresh water at 20°
ν	Kinematic viscosity of fresh water at 20°
τ	Torque
η	Efficiency
λ	Stream tube and duct velocity ratio
β	Dead rise angle

Roman letters

P	Pressure
V	Average velocity in axial direction
H	Head rise
h	Head loss
g	The gravitational constant
T	Thrust
$\dot{m}$	Mass flow rate
$\dot{Q}$	Volume flow rate
$\dot{Q}_e$	Normalised volume flow rate
W	Work
$\dot{E}$	Energy flow rate
n	Revolutions per minute
d	Diameter
L	Length
R	Radius

This page is intentionally left blank.

Key Pump Expressions

Here the key expressions related to the pump and blade design are presented with visualisation in figure 1 and 2.

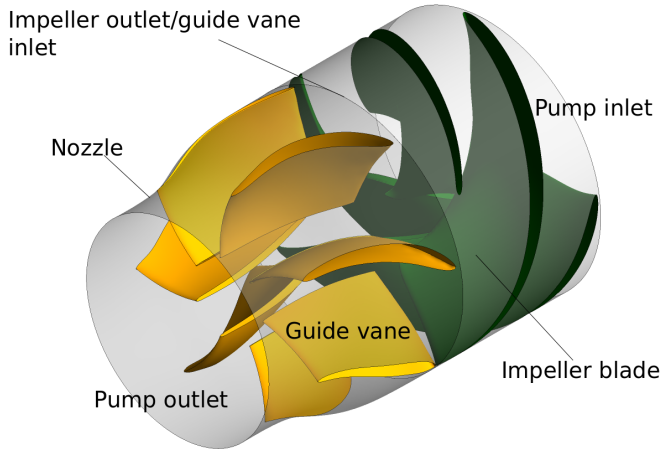

Figure 1: Illustration with key pump expressions.

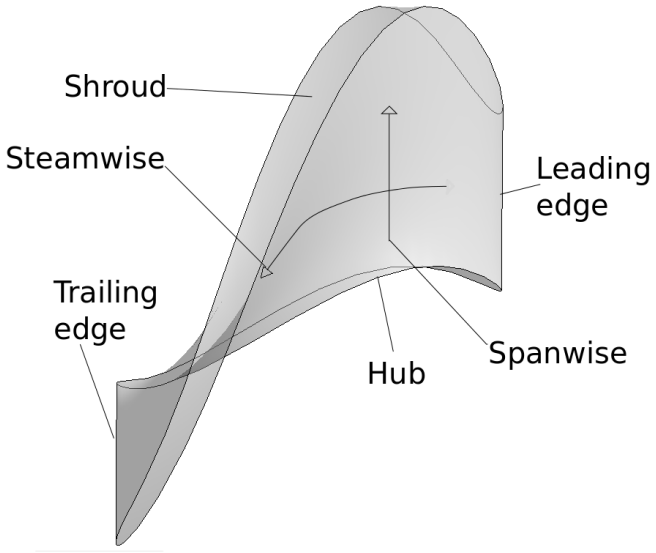

Figure 2: Illustration with key blade expressions.

This page is intentionally left blank.

1 Introduction

Rescue boats and other vessels operating near ships or marine structures in distress are vulnerable to floating debris. Such debris can get stuck in the propulsion system and cause vessel downtime. Floating lines, e.g. buoyant lines connected to life rafts, are especially problematic in conjunction with waterjets. After a few revolutions, a tangled polyester line will melt around the shaft and course a breakdown of the engine (see figure 1.1a). The engine can be damaged and the removal of melted or entangled lines can take several hours. Hours which are crucial in a rescue operation. The Swedish Sea Rescue Society has initiated the development of a new type of waterjet propulsion system in cooperation with Rolls-Royce. The goal is to minimize problems with debris and floating lines. The new propulsion system has been named a Rim-Jet. The Rim-Jet improves the operational ability of the small rescue craft as its vulnerability to floating debris is reduced. A decrease of the efficiency of the rim driven pump compared to a regular pump is expected, this is, however, an acceptable cost of reducing the downtime of the vessel. The increased ability to perform rescue operations in waters with floating debris improves the sustainability of the rescue operation.

1.1 Background

The Rim-Jet is inspired by the relatively newly commercialised rim driven thrusters (see figure 1.1b for an example.) which have shown great capabilities in handling debris in water. These thrusters are, however, neither capable of delivering the speed required of a rescue vessel, nor the safety of an enclosed propulsion system.

No commercial rim driven waterjet systems has, to the author's knowledge, been developed and research within the topic is very limited. Rolls-Royce has started the development with two separate master's theses. One thesis dealing with the mechanical design aspects of the system and one dealing with the hydromechanics of the rim driven waterjet pump as a main focus. This project is focused on the hydromechanics design and performance of the rim driven axial pump which powers the waterjet propulsion system.

(a) Entangled shaft. Picture courtesy of Fredrik Falkman (The Swedish Sea Rescue Society).

(b) Rim driven hubless thruster by Brunvoll (see [unknown, 2014]).

Figure 1.1: The figure contains a picture of the issue with rope entanglement (figure 1.1a) and a picture of a rim driven hubless thruster (1.1b).

1.2 Objective

The objective of the thesis is to develop and analyse the performance of a rim driven hubless axial pump with the capabilities of delivering the power required of the waterjet propulsion system to achieve the design speed and bollard pull. The design focus is mainly the hydrodynamic performance of the system and secondly on handling ropes in the pump.

One impeller and guide vane blade design is developed and studied using three separate pump cases.

- **Case 1.** A hubless rim driven pump with guide vanes.
- **Case 2.** A hubless rim driven pump with no guide vanes.
- **Case 3.** A rim driven pump with guide vanes and a hub.

Case 1. and 3. are used to study the effect of removing the hub and driving the pump at the rim. The purpose of Case 2. is to study the effect of removing the guide vane from Case 1. pump, Case 2. is expected to deliver the lowest pump efficiency, but the best handling of ropes in the pump.

The impeller and guide vane blades are developed using an iterative process based on results from computational fluid dynamics (CFD from here on out) analysis of the Case 1. pump configuration. The final concept design must meet the following technical specifications of the system (see table 1.2.1).

Ultimately a final concept design is to be recommended for further development.

1.2.1 Technical Specifications

The Swedish Sea Rescue Society (SSRS from here on out) has defined some main technical requirements for the Rim-Jet. These requirements are summarised in table 1.1.

Table 1.1: *The technical specifications the client.*

Requirement	Value	Unit
Vessel speed, V_s	20 - 25	knots
	10.3 -12.9	m/s
Maximum engine speed, n	4000	rpm
Maximum engine torque	132	Nm
Delivered power @ max rpm	55	kW
Maximum impeller diameter	195	mm
Bullard pull(Thrust), T	4	kN

The propulsion system is designed for a vessel of four meters. The substantial bollard pull required of the vessel originates from the operational pattern of the boat. The rescue boat must have enough thrust to pull several connected liferafts.

A more detailed system specification is necessary in order to perform the design work. Detailed specifications were created in cooperation with the mechanical designer. The relevant specifications are found in table 1.2. Some of these values are specified by the dimensional limitations of the engine and some are chosen based on ratios from previous waterjet designs in order to simplify the design process.

Table 1.2: *The detailed technical specifications. NOTE: Values given in brackets () are required by SOLAS, the boat is, however, not going to be operated in these conditions.*

Pump specifications		
Impeller diameter	195	[mm]
Impeller and guide vane axial length	100	[mm]
The "hub" diameter	60	[mm]
Outlet/inlet diameter ratio	60-80	[%]
Number of impeller blades	4	[-]
Number of stator blades	7	[-]
Elevation of nozzle outlet,	164.25	[mm]
Fluid Properties [ITTC, 2011]		
Fluid	Water	
Temperature	20	[°C]
Density (ρ)	998	[kg/m^3]
Vapour pressure	2.3	[kPa]
Design Target		
Bollard pull	4	[kN]
Impeller rotational speed	2000 - 4000	[rpm]
Torque delivered	132	[Nm]
Design speed	20(6)	[knots]
Displacement	800(1250)	[kg]

1.3 Method

Basic fluid dynamics is used to develop a energy model of the waterjet system. The model is used to calculated the requirements of the pump based in the inputs given by SSRS and estimations from previous waterjet designs.

The pump design software, TurboDesign1 (known as TD1 form here on out), is used for the 3D modelling of the impeller and the guide vane blades. This software uses potential flow theory and an inverse 3D design procedure which simplifies the designing of impeller and guide vane blades creating the desired flow.

The initial design is based on estimates of the head rise, flow rate and blade loading distribution needed to deliver the necessary thrust. The design is then improved using an iterative process with design changes based on viscus CFD evaluations of the performance of the pump. The software used for the CFD evaluation is Ansys Fluent 14.5. A steady flow analysis is conducted for the initial design and a transient flow analysis is conducted

on the final concept design to give a higher accuracy of the pump performance evaluation, a simple multiphase analysis is furthermore conducted in order to estimate the cavitation performance in bollard pull.

The evaluation of rope in pump performance is based on a simple study of the flow through the pump. The interaction between the blades and a rope is not easy to simulate with any tools readily available, and a literature study showed that no studies have been published on the topic, to the author's knowledge.

1.4 Limitations

The impeller diameter is defined by the geometry of the electromagnetic engine, this limits the design freedom significantly.

TD1 is not designed to create hubless blades, the pump is therefore designed with a cylindrical hub which is then removed in the CFD evaluation. This procedure has been used in other research projects, according to Turbo Design support, and it is therefore assumed to be a valid method for a rapid geometry definition. There are, to the author's knowledge, no programs capable of generating hubless pump blades. This fact, combined with Rolls-Royce significant experience in using TD1, is why the blade design is carried out using TD1. This is potentially limiting the achievable efficiency of the rim driven hubless pump, as the design tool is not created for this particularly use.

Due to the limited time frame of the project, only an initial CFD analysis is possible and there is no time to experimentally validate the specific CFD set-up. The consequences of this is that the models used are considered valid based on experience from Rolls-Royce and previous pump studies. An experimental pump test should be conducted in order to validate the CFD method for this specific pump type.

The study of rope in pump is, as mention in the previous section, not something that has been done before. There is, therefore, a limitation to conclusion of this study regarding rope in pump. The most effective way to test the rope in pump capabilities of the final design would be an experimental set-up, this is however not possible within the time frame of the thesis.

1.5 Changes form a Regular to a Rim Driven Waterjet Pump.

From a mechanical point of view the main difference between a regular and a rim driven pump is the absorption of the thrust (produced axial force). Usually, it is absorbed through the shaft. In this case it will have to be absorbed by a bearing solution in the rim. A comparison between a regular waterjet system and the Rim-Jet is seen in figure 1.2 for clarification. The driving engine is electric and mounted around the pump itself. An electric engine has a constant torque-rpm curve, this results in greater freedom when choosing the rpm at which the pump operates.

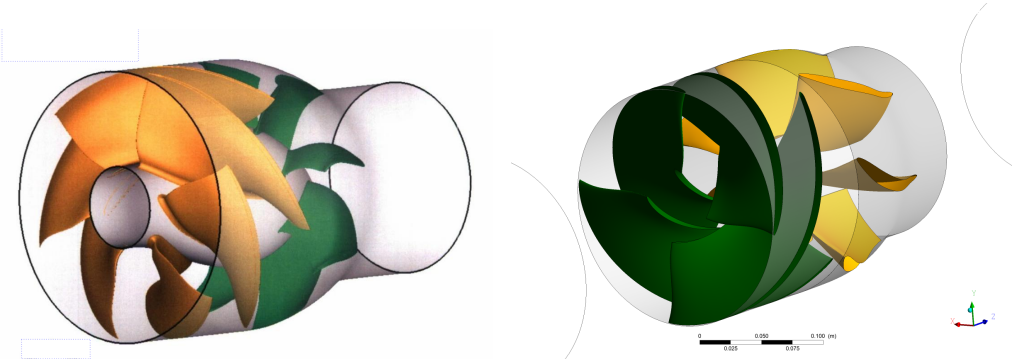

(a) Axial waterjet pump by [Thad et al., 2008].

(b) Rim driven waterjet pump.

Figure 1.2: Comparison of regular waterjet (figure 1.2a) and the Rim-Jet (figure 1.2b).

The largest impact of the hydrodynamic design is the removal of the shaft and hub. The removal of the shaft reduces the disturbances in the wake field entering the pump, leaving this mainly dependent on the inlet design. A less disturbed wake field will in general make it possible to have a more efficient pump and while maintaining good cavitation properties. The amount of fluctuating forces on the impeller blades are also lowered when the wake field is more homogeneous.

The missing hub is expected to cause problems. In a regular waterjet pump the gab between the shroud of the blade and the pump wall courses pressure leaks. This is reduced using a number of methods, one being a cavitation layer filling the gab. Driving the blade at the shroud and removing the hub leave a gab in the center of the pump allowing for pressure leaks to occur. The blades are designed with low loading towards the center to minimize these pressure leaks. Having this large gab in the center is likely to result in an overall reduced efficiency compared to a regular pump or a rim driven pump with a hub, it is however this gab that allows the pump to avoid entangling in ropes.

A significant design difference between the blade design of a regular and a hubless pump is the ability to manipulate the axial flow velocity through the pump. This is usually done by increasing the hub diameter over the length of the impeller. The rim

driven pump has a constant average axial flow velocity through the impeller, the flow is therefore only accelerated in the nozzle.

An electrical rim driven waterjet pump has a number of desirable differences compared to a regular waterjet when it comes to the design of the boat. The engine and generator can be placed anywhere without having to consider the shaft. This gives a greater flexibility in the propulsion system. The boat in question is, however, a small rescue craft, the flexibility is therefore limited. The initial boat design is presented in chapter 2.

1.6 Outline of the Thesis

The thesis consists of 11 chapters and appendices. A brief description of the content of the thesis is presented below.

Chapter 1 introduces the background of the project and defines the objective of the thesis.

Chapter 2 presents the rescue boat in question and the results of a trust prediction.

Chapter 3 describes the processes in a waterjet system and discusses pumps used for waterjet propulsion.

Chapter 4 presents the design process used for the development of the rim driven hubless waterjet pump.

Chapter 5 presents the tools and methods used in the design process, it includes references to the theory behind these methods.

Chapter 6 describes the energy model used to calculate certain design input parameters and benchmarking results for the evaluation of the performance of the concept design.

Chapter 7 introduces the steady state CFD model used for initial performance estimations and the comparison of the pump configurations.

Chapter 8 introduces the transient CFD model used for the final performance evaluation.

Chapter 9 presents the result of design process. The final pump concept is presented as wells as the major design changes throughout the design process are briefly discussed.

Chapter 10 presents the results of the CFD models introduced in Chapter 7 and 8. The performance of the final concept design is presented and discussed. A brief cavitation analysis is conducted in order to estimate the cavitation properties of the pump, and a flow analysis is conducted to evaluate the rope in pump performance of the pump.

Chapter 11 is the concluding chapter in which the main results of the thesis are summarised and the conclusions on the projects objectives are drawn. Future work suggestions are presented in a separate section.

The appendices presents the Matlab programs created for the thrust prediction and the energy model. The result of the convergence study and the settings for meshing are also presented. The result files are available upon request.

2 The Rescue Boat

The boat design is ongoing, however, SSRS has provided a sketch of the craft (see figure 2.1). The main dimensions of the boat are formulated based on these drawings, interaction with the SSRS and estimations, see table 2.1. These dimensions are used to create a thrust prediction for the boat.

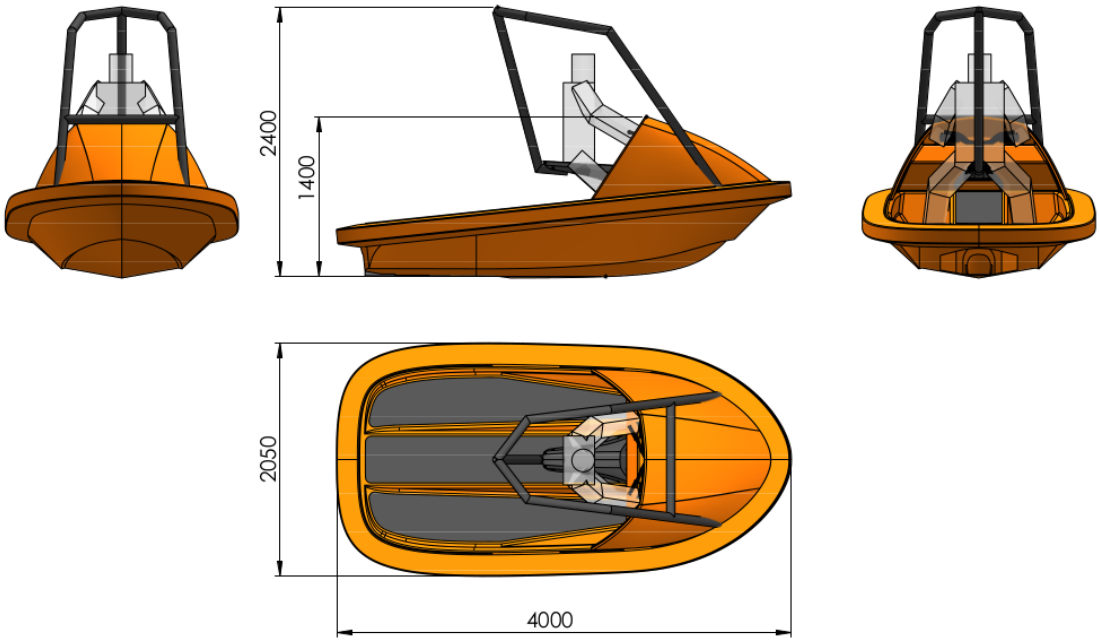

Figure 2.1: The initial boat design.

The weight and design speed in table 2.1 reflect both the transit condition with one pax on board (800kg) and with six pax on board (1250kg).The condition with six pax onboard is a requirement from the SOLAS regulations (requirement provided by SSRS), the boat is not meant to transport six pax. The condition prescribed by the SOLAS regulations are not specifically investigated in this thesis.

Table 2.1: Main particulars of boat

Main particulars	Value	Unit
Length, LOA	4	m
Planing breath, BP	0.97	m
Draught, T	0.54	m
Total weight	800(1250)	kg
Longitudinal center of gravity, LCG	1.675	m
Longitudinal center of buoyancy, LCB	1.69	m
Vertical center of gravity, VCG	0.4	m
Angle of deadrise, β	15 °	-
SOLAS pax capacity	6	-
Design speed	20(6)	knots

2.1 Thrust Prediction

Savitsky's method of thrust prediction is used to predict the thrust needed from the water jet propulsion system [Savitsky, 1964]. This Savitsky's prediction method provides a good estimate for planing vessels, such as the rescue boat in question, at an early design stage.

The interested reader is referred to Savitsky's article "Hydrodynamic design of planing hulls", see [Savitsky, 1964], and the matlab script used for the prediction in appendix A. The thrust prediction model created in connection with this thesis is in compliance with results from Orca3D provided by SSRS (Orca3D also uses the Savitsky's prediction method.).

In short Savitsky's prediction method is a 30 step thrust prediction method based on a large number of test data. The method predicts the required thrust for a certain speed, the trim angle and if the planing vessel is stable at that specific speed. The method is widely used to get an initial thrust prediction for small planing crafts with a constant dead rise angle (which is the case for the vessel in question). There are, to the author's knowledge, no better methods suited for a craft of this size, before the hull is designed and a resistance test is conducted. (Note that it is a thrust prediction method, not a resistance prediction method, as it takes the angle of the propulsion system into account. This angle results in the need for a larger thrust than the total resistance in certain cases.)

The thrust prediction curve is shown in figure 2.2. Here the so called resistance bump is seen with its peak around 14 knots. The boat starts planing when the resistance bump is passed, and as the wetted area of the vessel is reduced so is the resistance. A 20% seamargin is added to the thrust prediction to ensure the boat's ability to operate in smaller waves which causes added resistance on the hull. Larger waves causes a very

unstable speed for such a small vessel and a specific max speed is difficult to reach even with extra power.

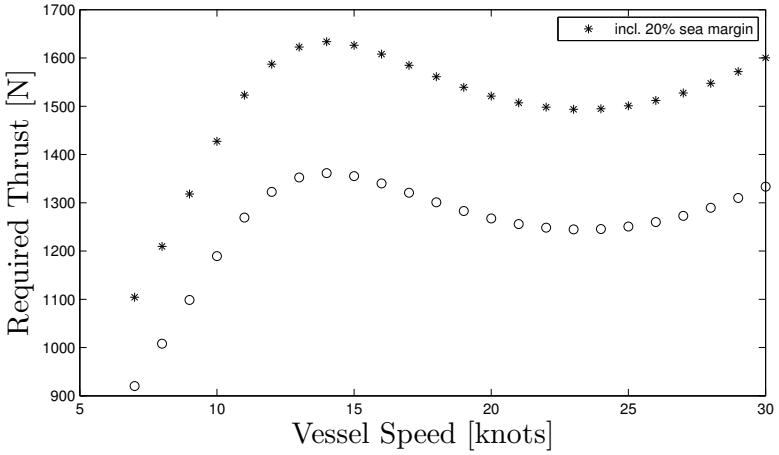

Figure 2.2: The thrust curve produced by the Savitsky prediction method and the same curve corrected with a 20% seamargin.

In figure 2.3 the trim curve is shown, it is seen that once the vessel start planing it moves towards neutral trim when the speed is increased (often ending at a certain design trim). It is also observed that the aft of the vessel is experiencing a suction at lower speeds, this creates the very steep resistance rise in the hump as it is not only the increased speed, but also the increased wetted surface which result in increased friction on the hull.

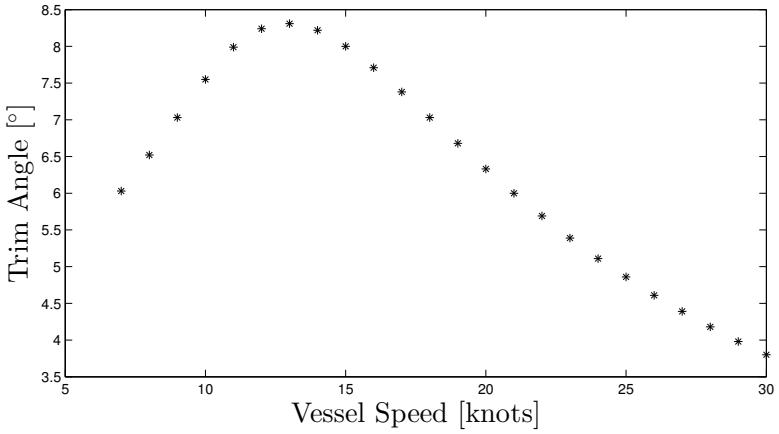

Figure 2.3: Trim curve produced by the Savitsky prediction method.

The thrust predicted with added seamargin is used as input for the mathematical model of the waterjet system. The thrust requirement is used to estimate the velocity of the jet leaving the nozzle and thereby the flow rate through the propulsion system.

This, in combination with the pressure loss, is governing the head rise needed from the pump and is therefore essential for the design of the waterjet propulsion system.

3 The Waterjet Propulsion System

In this chapter the general function of a waterjet propulsion system is described briefly. A simple sketch, following the ITTC standard (see [ITTC, 2005]) of a waterjet propulsion system is shown in Figure 3.1

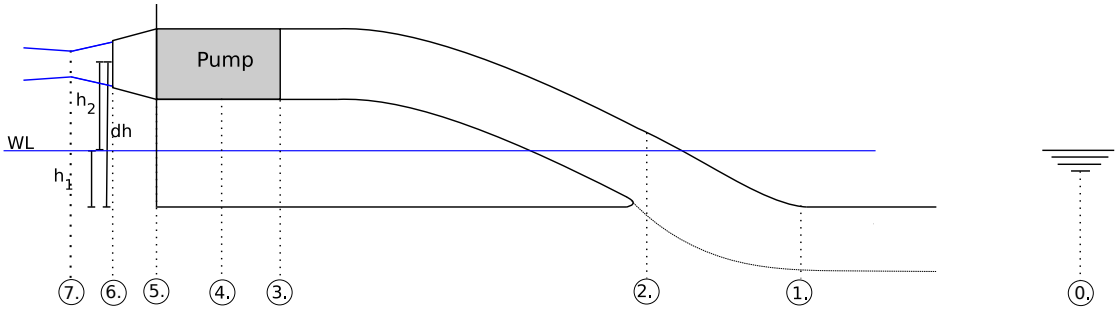

Figure 3.1: Waterjet principle model: Point 0. Free stream, Point 1. Stream tube inlet, Point 2. Duct inlet, Point 3. Pump inlet, Point 4. Pump center Point 5. Pump outlet, Point 6. Nozzle outlet and Point 7. Jet minimum diameter.

3.1 Processes of The Waterjet System

The processes throughout the system is presented in relation to the seven points shown in figure 3.1.

0. **The free stream.** The water flows free with a speed matching the speed of the boat through water.

1. **The stream tube inlet.** This is the part of the flow beneath the hull which enters the waterjet system. Here the average velocity is smaller than at point 0 due to the boundary layer built up on the keel. The cross section area is usually modelled as a rectangle with 1.35 times the width of the duct pipe diameter (Rolls-Royce standard) and a height determined by the mass flow rate through the waterjet.

2. **The duct inlet.** Here the water enters the physical propulsion system. A grid is installed in the inlet to avoid larger debris entering the system. The inlet geometry and the grid results in a significant pressure loss. This loss is dependent on the ratio between the average axial flow velocity in the duct (point 3.) and in the stream tube (point 1.).

3. **The pump inlet.** The wake field entering the pump is defined at this point. The pressure can be both higher and lower than the pressure at point 1. depending on the operation of the vessel. The pressure at this point is dependent on the mass flow rate rate of the system, the vessel speed and the pressure loss experienced in the duct inlet.

4. **The pump center.** Here, right after the rotor, the static pressure is at its maximum. The flow is highly rotational, but with the same average axial velocity as at point 3.

5. **The pump outlet.** The guide vanes are mounted in the nozzle and are running from point 4. to 6. transforming static pressure into a dynamic pressure as the water is accelerating through the nozzle. The guide vanes reduce the head rise required to produce a specific thrust by recovering some the the energy bound in the swirl.

6. **The nozzle outlet.** Here the accelerated jet leaves the physical propulsion system.

7. **Jet maximum Vena contraction.** The jet continues to contract after leaving the nozzle (at point 6.) due to the Vena contraction phenomena, see [ITTC, 2005]. This is the point at which the diameter of the waterjet is at its minimum, the point is considered the end point of the propulsion system. At this point the maximum average velocity of the jet is reached and the thrust of the system is determined. The contraction between point 6. and point 7. is, however, often insignificant.

3.2 Thrust

Thrust is an expression used to define the force a waterjet system produces on a vessel. Thrust is defined as a the forward acting force produced by propelling water backwards. The system follows Newton's third law by exceeding a force on the water in the jet which then exerts a force on the blades which is then transferred to the boat, propelling it forward. The thrust equation is defined in [Allison, 1993, Chap. 16.] and shown in equation 3.1.

$$T = \dot{m}(V_7 - V_1) \tag{3.1}$$

Where V represents the average axial velocity at points defined by the subscripted numbers, see figure 3.1, $\dot{m}$ is the mass flow and T is the produced thrust. As the steamtube velocity (V_1) is dependent on the vessel's velocity through water (V_0) it is

apparent that the thrust is reduced when increasing the vessel speed (V_0), if the jet velocity (V_7) is kept constant.

Bollard pull is the definition of the thrust produced at zero speed and represents the maximum pulling force a propulsion system can produce at a specific rotational speed and torque.

3.3 The Pump

The pump is the heart of the waterjet propulsion system. This is where the energy is transferred from the engine to the water via the impeller blades. Most waterjet pumps consist of two stages; the impeller and the nozzle stage in which the guide vanes are integrated parts of the nozzle, see figure 3.2 for reference (Note that the colours of the impeller and guide vane blades are reversed in figure 3.2).

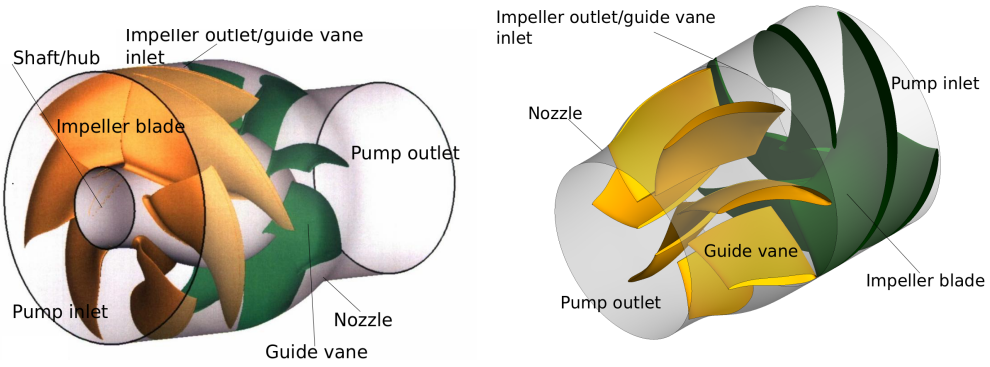

(a) Axial waterjet pump by [Thad et al., 2008] with labeling. Impeller: Orange. Guide vane: Green

(b) Rim driven waterjet pump with labeling. Impeller: Green. Guide vane: Orange

Figure 3.2: Comparison of regular waterjet (figure 1.2a) and the Rim-Jet (figure 1.2b).

The rotating impeller adds energy to the fluid, creating a pressure rise and sustaining the flow rate of the system by counter acting the pressure loss throughout the system. The static pressure is high after the impeller due to a high degree of swirl in the flow introduced by the rotating impeller. The water is accelerated through the nozzle stage transforming the high static pressure to dynamic pressure (kinetic energy). The transformation from static to dynamic pressure is achieved by narrowing the channel (the nozzle) and streamlining the flow in the axial direction via the guide vanes.

The guide vanes introduces extra friction in the pump, but the steamlining of the flow reduces the the required head rise, by converging swirl to axial flow, to such a degree that the overall axial pump efficiency is increased. Energy bound in the swirl after the nozzle is lost energy as it does not contribute to the propulsion of the vessel. The interested reader is referred to [Brennen, 1994] for an in depth presentation of the theoretical function of a pump.

The two main types of pumps, used for waterjets propulsion systems, are the mixed-flow and the axial flow pump. A mixed flow pump relies on increased average axial velocity of the flow over the impeller blades, this, however, is not possible when the hub is removed, the Rim-Jet is therefore based on an axial flow pump. An axial pump can be designed with a constant average axial flow velocity, but a velocity increase over the pump, induced by the hub shape, is used to achieve a high impeller efficiency. An example of a axial flow pump is seen in figure 3.2a. An axial flow pump is usually used for high flow rates and small head rises, making it ideal for high speed with lower thrust and less than ideal for bollard pull production.

3.3.1 The Pump Configuration Cases

The cross section of the three pump configuration cases considered are sketched in figure 3.3. This displays the projected cross section area of an impeller blade and a guide vane. Note that the Case 2. configuration is shorter than Case 1. and 3. as there is no guide vanes the nozzle is shortened.

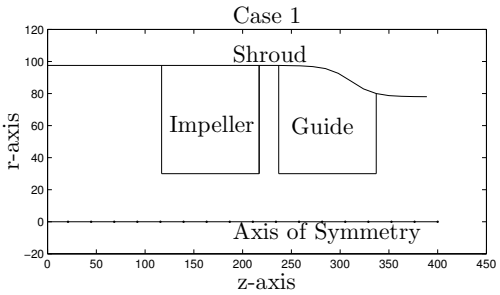

(a) Case 1 2D sketch.

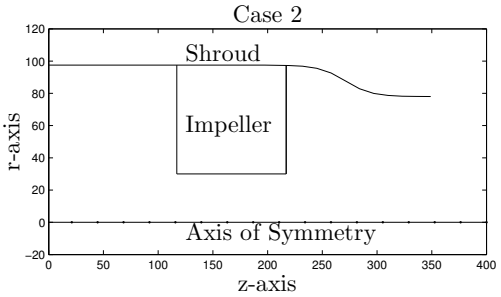

(b) Case 2 2D sketch.

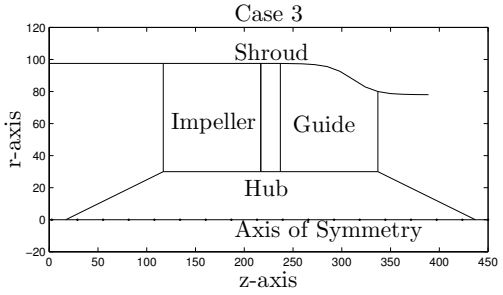

(c) Case 3 2D sketch.

Figure 3.3: Sketches of the three pump cases.

4 The Design Process

The design process is an iterative process consisting of a number of sub-processes, see figure 4.1 for a visualisation of the design process. The design process is based on the Rolls-Royce standard process with inspirations from design studies such as [Bonaiuti et al., 2010]. The pump design has a large number of variables and few limiting factors as it is a completely new design.

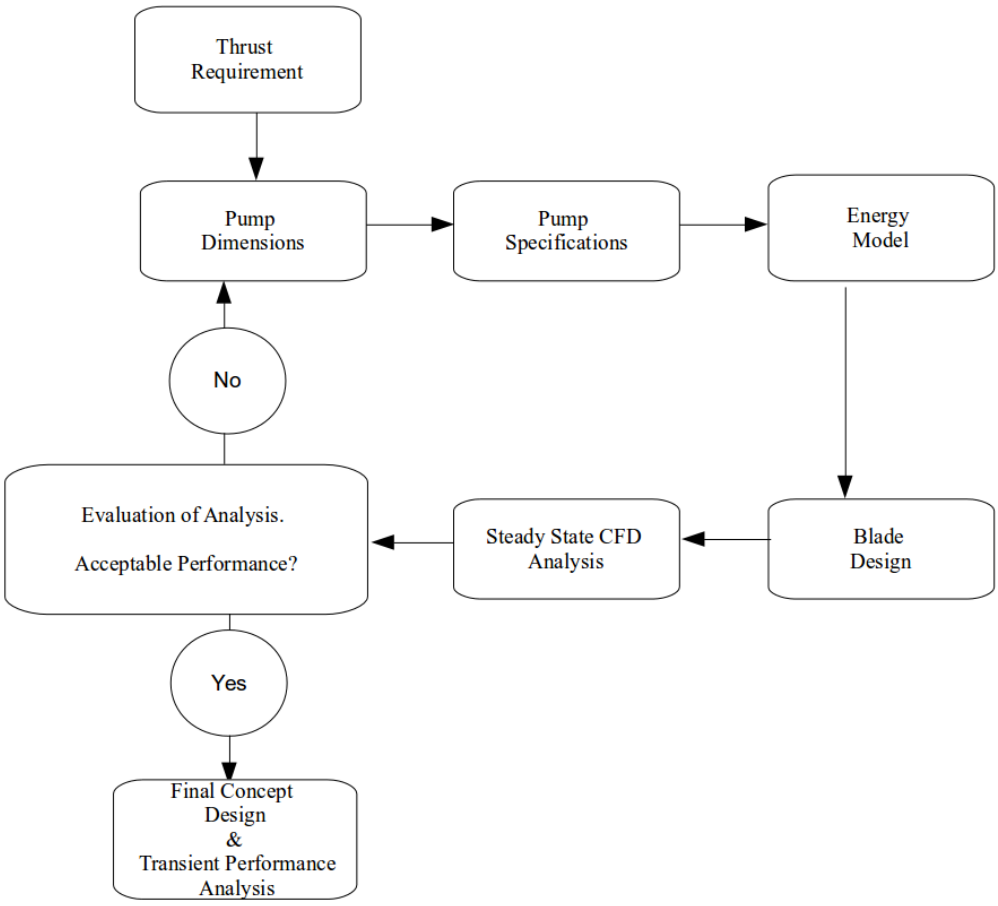

Figure 4.1: Illustration of the iterative design process.

The processes shown in figure 4.1 are briefly described in the below list.

- **Thrust Requirement**
  The pump design is based on an estimation of the required thrust of the vessel. This estimation would usually be based on a towing tank test. In this case the final hull is yet to be designed, and the thrust is therefore estimated based on the main particulars using the Savitsky's prediction method, see section 2.

- **Pump Dimensions**
  The pump diameter is limited by the rim engine. The length of the pump, the impeller blades and the guide vanes are chosen based on ratios from previous waterjet designs.

- **Pump Specifications**
  The operational revolutionary speed and the number of impeller and guide vane blades are selected. The number of blades are kept low in order to reduce the complexity of the pump and reduce the chances of debris getting stuck.

- **Mathematical Model**
  The flow rate and the required torque are estimated based on the thrust prediction and the nozzle outlet diameter. The outlet diameter of the nozzle is corrected so that the minimum torque is well within the engine specification. The average impeller blade loading is estimated using a simple empirical method from the TD1 application manual [TD1, 2012a].

- **Blade Design**
  The impeller and guide vane blades are designed using TD1, inputs from the above mentioned processes and studies of high performing designs from the literature, such as [Thad et al., 2008] and [Bonaiuti et al., 2010].

- **Steady State CFD Analysis**
  The CFD pump performance analysis consists of a number of analyses. The performance of the initial designs are estimated based on a steady flow analysis in order to reduce the computation cost.

- **Evaluation of The CFD Analysis**
  The results of the CFD analysis are evaluated. If the pump performance is acceptable a concept design has been reached. If the pump performance is unacceptable the design process starts over. In such a case it must be considered whether an acceptable performance can be reached by mainly changing the blade loading or if other design parameters, such as the rotational speed of the impeller and the nozzle outlet diameter, need to be changed as well. At a certain point it must be considered if the performance goal is reachable within the design limitations or if these must be reconsidered.

- **Final Concept Design**
  Once a final concept design is reached a transient analysis is conducted to evaluate the overall performance of the pump, including the expected pump efficiency and an estimation of the cavitation properties, using a multiphase model added to the transient analysis.

  The next stages of the pump design are working towards the final production design.

This page is intentionally left blank.

5 Design Tools and Methods

In this chapter the tools and methods, used for the pump design, are introduced. These are TurboDesign1, using potential flow theory for the design of the blades, and a viscus CFD code is used for the performance analysis of the pump design.

5.1 TurboDesign1

TurboDesign is a design tool package for designing of turbo machinery. The tool used in this case is TurboDesign1. TD1 is designed to create a 3D blade geometry based on a number of input parameters. TD1 uses an inverse 3D design method to rapidly create blade geometries, this method was developed by M. Zangeneh [Zangeneh, 1991]. This is achieved by designing the blade based on a specific in and output velocity field. The impeller and guide vane blades are designed independently, but the guide vane blade uses the output velocity field from the impeller as the base of its input velocity field. The TD1 design process starts with an initial blade shape presented by a vorticity field from which the outlet velocity field of the pump is calculated. Potential flow theory is used to calculate the flow, this enables a fast computation time as the flow is assumed inviscid, which reduces the complexity of turbulence flow simulation. The output velocity field is compared to the wanted velocity field. A new blade profile is created and the vorticity is calculated, a new output velocity field is calculated from the vorticity field, and the iterative process continues until the blade matches the specified output velocity field.

The blade design is created including a hub as the software cannot design a hubless blade. The hub is then excluded in the viscus CFD performance evaluation. The excluded hub is, however, considered when designing the blades by unloading the blades towards the center of the pump.

5.1.1 Potential Flow Theory

In potential flow theory the flow around a body is assumed inviscid, and mass and momentum are assumed constant. Potential flow theory is used based on the assumption that viscosity primarily has an important impact on a flow in the boundary layers on walls. Potential flow theory is described in detail in many textbooks, see for example White [1974]. Potential flow theory works well for rapid flow analysis, but the system is without damping and losses caused by friction. This makes it an ideal system, a viscus analysis is needed to evaluate the actual performance of the system.

5.1.2 Design Parameters

An example of a pump designed using TD1 and CFD analyses is presented in [Bonaiuti et al., 2010]. The design parameters used by TD1 are seen below.

1. **Meridional channel shape.** A drawing of the channel shape including the hub, shroud and the projected area of the impeller and guide vane blades. See figure 5.1

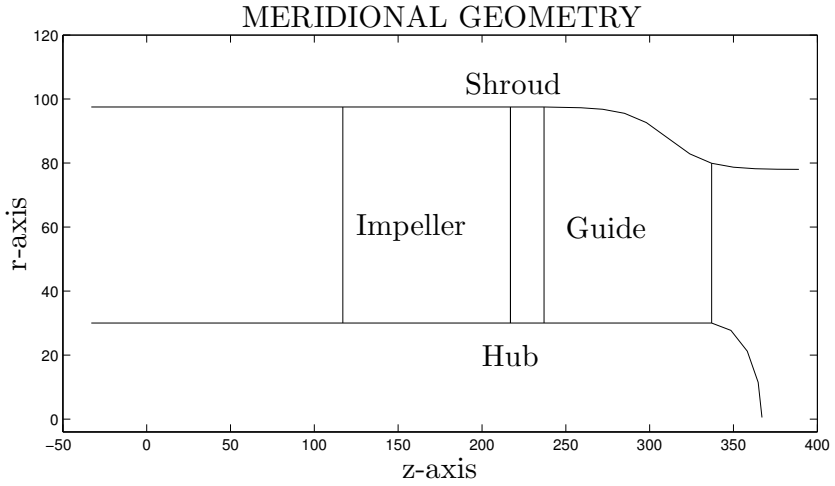

Figure 5.1: Meridional plot of the channel shape. The hub is included as it is a requirement for the input to TD1.

2. **Thickness distribution.** The thickness distribution of the blades are defined along the camber line at the hub, the mid and at the shroud. The spanwise (going from hub to shroud) thickness distribution is then linearly interpolated in between these sections. A separate thickness distribution can be defined for the impeller and guide vane blades, however, in this thesis the same thickness distribution is used for both the impeller and the guide vane blades.

3. **Fluid properties and design specifications.** The working fluid, the rotational speed and the inlet velocity and pressure field is specified.

4. **Number of blades.** The number of impeller and guide vane blades are chosen. There is in general more guide vane blades than impeller blades.

5. **Vorticity distribution.** The blade loading is spanwise specified by a given vorticity at the hub and shroud at the leading and trailing edge.

6. **Blade loading.** The streamwise (following the camber line from leading to trailing edge) blade loading is imposed at two or more span locations. The program makes a linear interpolation of the loading between the defined spanwise positions.

7. **Stacking condition.** The stacking condition defines a spanwise line (at a specific streamwise position) as the starting point of the blade design. It defines if the blade is leaning towards or against the rotational direction at that specific streamwise position. The blade can freely adjust according to the defined blade loading and vorticity distribution everywhere else along the chord length.

These are the seven main design parameters. Some of these parameters are limited by other design limitations, such as the design specifications, others are based on ratios from excising waterjet designs and kept constant or only slightly modified throughout the entire design process to reduce the amount of variables.

5.2 Computational Fluid Dynamics Analysis

Computational fluid dynamics covers a wide range of numerical ways to solve the Navier Stokes' equations. In this section the methods used for the CFD analysis are presented. There is a large number of CFD methods each with their own advantages, the two main considerations for all CFD calculations are the quality of the results contra the cost of computation. These two parameters are often connected; if results of excellent quality is required, the computation is costly.

A steady flow analysis is the foundation of the performance evaluation as it has a low cost of computation, and a great number of analyses are done to evaluate the effect of design changes. The quality of the steady flow computation is decent, but a transient analysis is conducted for the final concept design to obtain a more precise indication of the pump performance.

5.2.1 Steady State Analysis

The steady state analysis is a cost efficient analysis. It is used to evaluate the pump performance and to visualise where changes are needed. The analysis excludes any time dependent effects and estimates the flow through the pump as steady. The rotation of the impeller blade is modelled by introducing a simulated rotation of the grid surrounding the impeller blade. Thereby modelling the rotation of the blade in a constant flow rate and causing the correct lift and loading on the impeller blade. The guide vane is, however, kept at a constant relative position compared to the impeller blade, this is a consequence of the steady state model. A transient analysis includes the time dependent effects.

5.2.2 Transient Analysis

A transient analysis is a study of a time dependent unsteady flow, with a high computational cost. It is used to study how unsteady flow evolves over time. The impeller blades are rotating, and thereby shifting their relative position compared to the guide vanes over time, this results in a time dependent unsteady flow. The transient analysis is therefore a more accurate model of the flow in the pump than the steady state analysis.

The final solution of the flow is a repeated cycle of fluctuating results. The analysis is conducted for constant flow rates but with fluctuating and dynamic effects between the impeller and guide vane blades.

5.2.3 SST $k-\omega$ Turbulent Flow Model

The turbulent flow in both the steady and transient analysis is modelled using the SST (Shear-Stress Transport) $k-\omega$ turbulent flow model proposed by Menter in 1992 [Menter, 1993]. This model combines the standard $k-\epsilon$ model with the Wilcox $k-\omega$ model, using the best properties of both models.

The $k-\epsilon$ model is functioning well when applied on a free stream flow, however, a wall dampening function is needed when evaluating the flow near a wall. The Wilcox $k-\omega$ model works well at predicting flows near a wall, thus removing the need for a wall function, it is however more unstable in free stream. The combination of the two models results in a stable turbulent model capable of modelling the flow both in the free stream and near the wall. See [Versteeg and Malalasekera, 2007, Chap. 3] and [Menter, 1993] for reference and a more detail description.

This specific model is regarded as an efficient and flexible model, and Rolls-Royce has had positive experiences using this model.

5.2.4 Mixture Flow Model

A multiphase analysis is conducted using the mixture flow model ([Ansys, 2013]). The analysis is used to evaluate the cavitation properties of the pump. It is applied in combination with the turbulence flow model in the transient analysis. The two phases of the water is defined as water-liquid and water-vapour, and a mass transfer function is defined. This function defines when cavitation occurs using a defined vapour pressure given as input.

It is difficult to obtain a stable calculation using the mixture model, especially if there is a large amount of cavitation in the pump. A first order scheme is therefore used to calculate the volume fraction and the momentum equation, this increases the stability of the calculation, but decreases the model accuracy. The model is, however, regarded as a good method to establish an indication of the cavitation properties of the pump.

A cavitation analysis is usually adjusted to match experimental results, this however is not an option in this thesis. The results of the cavitation analysis are therefore only regarded as an indication numerical cavitation properties of the pump.

5.2.5 Schemes

The second order upwind scheme is used in the steady and transient flow analyses. As the flow is mostly in the axial direction the second order upwind scheme is a good choice resulting in second order accuracy of the results and a high stability. An implicit scheme is used when evaluating over time steps in the transient analysis. The first order upwind scheme is used for the momentum and volume fraction calculations in the

cavitation analysis. The first order scheme is less accurate than the second order, but the stability is better. For more details regarding the theory behind the different schemes the interested reader is referred to [Versteeg and Malalasekera, 2007].

5.2.6 Solver Algorithm

The algorithm used to solve the pressure and velocity in the steady flow model is the SIMPLE algorithm. The SIMPLE algorithm is a simple iterative solver with great calculation stability properties. The algorithm introduces under-relaxation, for increased computation stability, using the guess and correct solver approach, see [Versteeg and Malalasekera, 2007, p.186-190] for reference and a detail description. The solver runs through the cells one at a time making it possible to run on computers with a small amount of memory.

A modified version of the SIMPLE solver is used to solve the equation system in the transient analysis. Here a time dependence is added to the solver making it possible to solve unsteady flow problems, see [Versteeg and Malalasekera, 2007, sec. 8.7].

5.2.7 The Computational Mesh

The computational grid or mesh is generated using a CAD/mesh tool in the Ansys Workbench. The mesh is structured at the walls to ensure a sufficient resolution of the boundary layers. The blades are also considered as walls, but are modelled with smaller cells in order to construct the complex geometries and obtain sufficiently low y-plus values. The remaining computational domain is constructed using an unstructured mesh. A short grid dependence study is conducted to ensure sufficient grid independence.

5.2.8 y-plus

The size of the first cell at a wall determines the y-plus size. The incorporated wall treatment of the turbulent flow model is design for a specific y-plus value range. The resolution of the boundary layer have to be fine enough to ensure that the y-plus of the mesh has a sufficient size for the turbulent flow model. It is however costly to obtain a small enough y-plus value for research purposes (y-plus around 1) an industry standard range of 30-60 is used as it has a low cost/benefit ratio (Rolls-Royce standard). A more detailed description of y-plus can be found in [Versteeg and Malalasekera, 2007, Chap. 9.].

5.2.9 Convergence

To determine if a computation has converged one needs to define convergence. There are different definitions of convergence when looking at the steady and unsteady flow analysis. In this project steady flow convergence has been defined as a minimum reduction of a factor ten for the residuals and a maximum fluctuation of 1% of the torque on the impeller blade over the last 200 iterations.

The unsteady flow convergence is defined as a cyclic fluctuating solution with a time average difference of less than 1% from cycle to cycle.

5.2.10 The CFD Code - Ansys Fluent

The tool used for the viscous computational fluid dynamics analysis of the pump is Ansys Fluent. This is an efficient and widely used CFD code for enclosed flows.

5.2.11 Postprocessing

The post-processing is conducted using Ansys Post. Using the post-processing tool the flow is visualised and studied. Data used for calculations of the pump performance is extracted from the CFD calculations.

6 Energy Model

In this chapter a simple mathematical model is developed to create an overview of the energy flow through the system. The development of the model is necessary in order to calculate the data required for the inputs, assumptions and benchmarking of the pump design. The model is a compilation of different methods of estimating the energy flow, the head losses and the thrust required of the waterjet system. The energy model covers the waterjet propulsion system from the steam tube inlet to the jet outlet.

In figure 6.1 the sketch displayed in section 3 is shown in order to create a better overview of the system, the points displayed in the figure are referred to and used as subscriptions throughout the energy model.

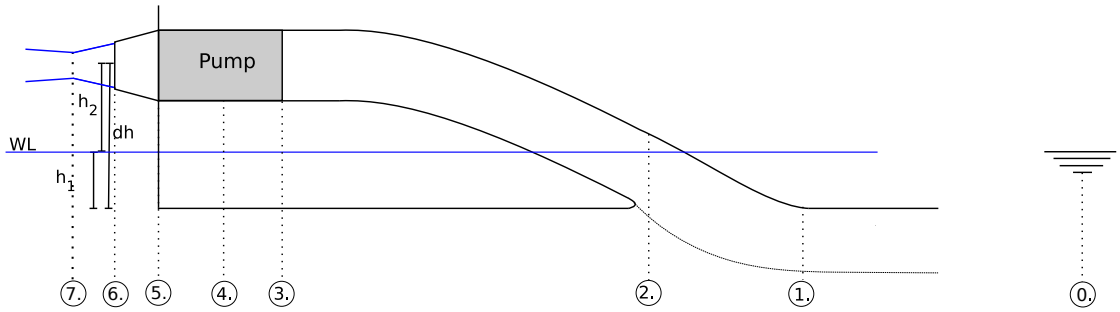

Figure 6.1: Waterjet principle model: Point 0. Free stream, Point 1. Stream tube inlet, Point 2. Duct inlet, Point 3. Pump inlet, Point 4. Pump center Point 5. Pump outlet, Point 6. Nozzle outlet and Point 7. Jet minimum diameter.

6.1 Assumptions

The assumptions used in the energy model are presented in the following list:

- The flow rate is assumed constant. The mass flow rate is changed to simulate a number of operational points, but is constant at each operational point in order to simplify the model.
- Temperature variations are assumed insignificant and are therefore neglected. The temperature variations are minimal for pressure changes in a fluid.

- It is assumed that the Vena Contraction is insignificant or that the actual nozzle size results in a Vena Contraction matching the jet output area considered here. This effectively sets the velocity and pressure at point 7. equal to that of point 6 (in figure 6.1).
- The duct of the boat is assumed to be a standard Rolls-Royce duct. Experimental data for this duct enable a calculation of the expected pressure loss through the duct. The method is described in an internal Rolls-Royce report [Rolls-Royce, 2010].
- The steam tube is assumed to have a rectangular cross section with a width of 1.35 times the impeller diameter (point 1.). This is a Rolls-Royce standard assumption for the calculation of the flow velocity in the steam tube.
- A grid loss factor of $\xi_{grid} = 0.05$ is assumed and added to the inlet loss factor. This assumption is a rough estimate based on Rolls-Royce experience.

6.2 The Model

The energy model models the energy flow through the propulsion system, and is used to evaluate the head rise needed to maintain the required thrust for a given operational speed (See figure 2.2). The system is modelled using the energy equation (A Bernoulli equation modified to include losses) presented in [Carlton, 2007]. The variables are rearranged slightly in order to create a simple connection between this mathematical model and the following CFD model. The energy is, according to tradition, referred to as meter water column, making the unit of the energy equation meters.

$$\frac{P_1}{\rho g} + \frac{V_1^2}{2g} + H = \frac{P_7}{\rho g} + \frac{V_7^2}{2g} + \Delta h + h_{duct} + h_{pump} \tag{6.1}$$

H is the total head rise delivered by the pump, Δh is the head loss related the the elevation of the outlet above the keel (see figure 2.2), h_{duct} the head losses in the duct and h_{pump} is the head loss in the pump. V_1 is the average velocity at the stream tube inlet and V_7 is average the velocity of the jet at the maximum Vena contraction. By expanding P_7 to $P_7 = P_1 - h_1 \rho g$ equation 6.1 is reduce to:

$$H = \frac{V_7^2 - V_1^2}{2g} + h_2 + h_{duct} + h_{pump} \tag{6.2}$$

$$\tag{6.3}$$

The power delivered to the pump is proportional to the head rise produced by the pump.

$$P_{pump} = \dot{m} g H \tag{6.4}$$

$$\tag{6.5}$$

The thrust delivered by the jet is equal to the mass flow times the difference in speed between the average axial stream tube velocity (point 1.) and jet average axial velocity (point 7.). As the thrust is known from the Savitsky prediction in figure 2.2 the average velocity at point 7 is determined using the thrust equation.

$$T = \dot{m}(V_7 - V_1) \tag{6.6}$$

The size of the stream tube is, however, dependent on the mass flow, this makes the average velocity in the stream tube (V_1) dependent on the mass flow. The cross sectional area of the stream tube is divided into two areas, the boundary layer and the free flow area (going perpendicular to the flow direction) each with different average velocities. The average axial velocity and the cross sectional area of the boundary layer are estimated using theory describing the turbulent boundary layer on a flat plate, see [White, 1974, p.433-434]. The free flow area of the stream tube is calculated so that the mass flow requirement is reached (The free flow area is defined by the difference between the mass flow in the boundary layer and the needed flow rate of the stream tube). The mass flow is, as mentioned earlier, dependent on the average stream tube velocity thus making it necessary to solve the problem ($\dot{m}$,V_1 & V_7) using a simple iterative solver. See appendix B for the full Matlab program containing the mathematical model.

The work done in propelling the vessel is based on the trust, and is expressed by the following equation [Allison, 1993].

$$W_{jet} = TV_0 = \dot{m}(V_7 - V_1)V_0 \tag{6.7}$$

The propulsion efficiency is defined as the ratio between the work done in propelling the vessel (equation 6.7) and power delivered by the pump (equation 6.5) [Allison, 1993; Carlton, 2007].

$$\eta_{propulsion} = \frac{TV_0}{\dot{m}gH} = \frac{(V_7 - V_1)V_0}{\frac{1}{2}(V_7^2 - V_1^2) + g(h_2 + h_{duct} + h_{pump})} \tag{6.8}$$

It is desirable to achieve the highest possible propulsion efficiency as this results in the minimum fuel consumption and thereby minimise the operational cost. The propulsion efficiency is often increasing with increased velocity for a waterjet propulsion system, this growth is, however, dependent on how rapid the head loss (h_{duct}) in the duct is growing.

The velocity term in the numerator of equation 6.8 is growing linearly while the denominator is experiencing quadratic growth, until a point is reached where the head loss in the duct increases rapidly.

A more interesting way of evaluating the efficiency of the system is the efficiency of the pump (η_{pump}). The pump efficiency is of greater interest as it is also evaluated at the bollard pull condition($V_0 = 0$). This efficiency is based on the total energy input (equation 6.5) and the effective head rise ($H_{effective}$) produced by the pump. The effective head rise is equal to the total head rise (H) subtracted the internal head loss in the pump (h_{pump}) and the energy in leftover swirl in the jet after the nozzle (h_{swirl}) (point 7), see equation 6.9.

$$H_{effect} = H - h_{pump} - h_{swirl} \tag{6.9}$$

The efficiency of the pump is of great importance as the pump is the heart of the thrust production. The pump efficiency is defined as the ratio between the effective head rise ($H_{effective}$) and the total head rise (the total energy input) (H).

$$\eta_{pump} = \frac{H_{effect}}{H} \tag{6.10}$$

From the CFD analysis the total energy input to the system (H) is determined using the torque on the blades and the angular velocity of these.

$$P_{total} = \tau\omega \tag{6.11}$$

$$H = \frac{P_{total}}{\dot{m}g} \tag{6.12}$$

With τ being the torque delivered by the engine and ω being the angular velocity of the impeller rotation. The efficiency expression used for the pump in this thesis is expressed using equation 6.10 and 6.12

$$\eta_{pump} = \frac{\dot{m}gH_{effect}}{\tau\omega} \tag{6.13}$$

The head loss related to the duct (h_{duct}) must be estimated in order to effectively predict the needed effective head rise of the pump. The duct head loss consists of a number of losses, see [Carlton, 2007]. The losses related to the duct are shown in equation 6.14.

$$h_{duct} = h_{inlet} + h_{sf} + h_{bend} \tag{6.14}$$

These losses are related to the inlet loss (h_{inlet}), the skin friction (h_{sf}) throughout the duct and the pressure loss caused by a bending pipe h_{bend}. All of these losses are estimated based on an internal Rolls-Royce report, see section 6.2.1. The internal pump loss (h_{pump}) includes the loss related to the outlet nozzle and the guide vanes. This loss is not estimated as it is evaluated in the CFD models and defines the pump efficiency. The model for prediction of the head losses are presented in the following section.

6.2.1 The Head Losses

The total head loss of the duct (h_{total}), including the elevation of the nozzle, is estimated based on experimental data available from Rolls-Royce [Rolls-Royce, 2010] and the dimensions of the boat.

The Inlet and Duct Head Loss

The head loss (h_{duct}) from the duct inlet (point 1. to 2.) to the pump inlet (point 3.) is related to the inlet geometry (including the inlet grid), the mass flow rate of the system and the speed of the vessel. The head loss is estimated using an empirical method (based on model scale tests) recommended in an internal Rolls-Royce report [Rolls-Royce, 2010].

The duct velocity factor, λ, is defined as the ratio between the average flow velocity in the stream tube (V_1 figure 6.1) and the average velocity in the duct (V_3).

$$\lambda = \frac{V_1}{V_3} \tag{6.15}$$

An inlet loss factor ξ is determined using a polynomial with λ as a variable fitting the experimental data (see figure figure 6.2). This polynomial is connected to the specific method used to predict the total energy at point 3. in figure 6.1. The inlet loss factor (ξ) defines the amount of energy lost from the duct inlet to the pump inlet (point 3.), see equation 6.18.

The y-axis and the specific polynomium used is excluded from the report and the mathematical model in the appendix due to intellectual property rules from Rolls-Royce.

A grid loss factor(ξ_{grid}) of 0.05 is added (see assumptions, section 6.1) to the inlet loss factor to include the pressure loss caused by the inlet grid. Thus the total inlet loss factor is

$$\xi_{total} = \xi + \xi_{grid} \tag{6.16}$$

In figure 6.2 the inlet loss factor with and without inlet grid correction is plotted. It is clear from the figure that the inlet loss factor is sensitive to large λ values and the smallest inlet loss occurs just before $\lambda = 1$.

The energy input at point 1. is evaluated with still water at the depth of the keel as reference.

$$\dot{E}_1 = (\frac{1}{2}\rho V_1^2)\dot{Q} \tag{6.17}$$

where $\dot{Q}$ is the volume flow rate into the system and $\dot{E}$ is the energy flow rate in watts ($kg/m^3 \cdot (m/s)^2 \cdot m^3/s = kg \cdot m^2/s^3 = Nm/s = W$).

The total energy at point 3 is determined using a simple energy equilibrium.

The inlet loss factor (ξ) is used to evaluate the energy at the duct outlet (or the pump inlet (point 3.)) ($\dot{E}_3$). The definition of $\dot{E}_3$ from the Rolls-Royce report is used and rewritten, using equation 6.15, in order to make it possible to evaluate the head loss in the bollard pull operation ($V_1 = 0$).

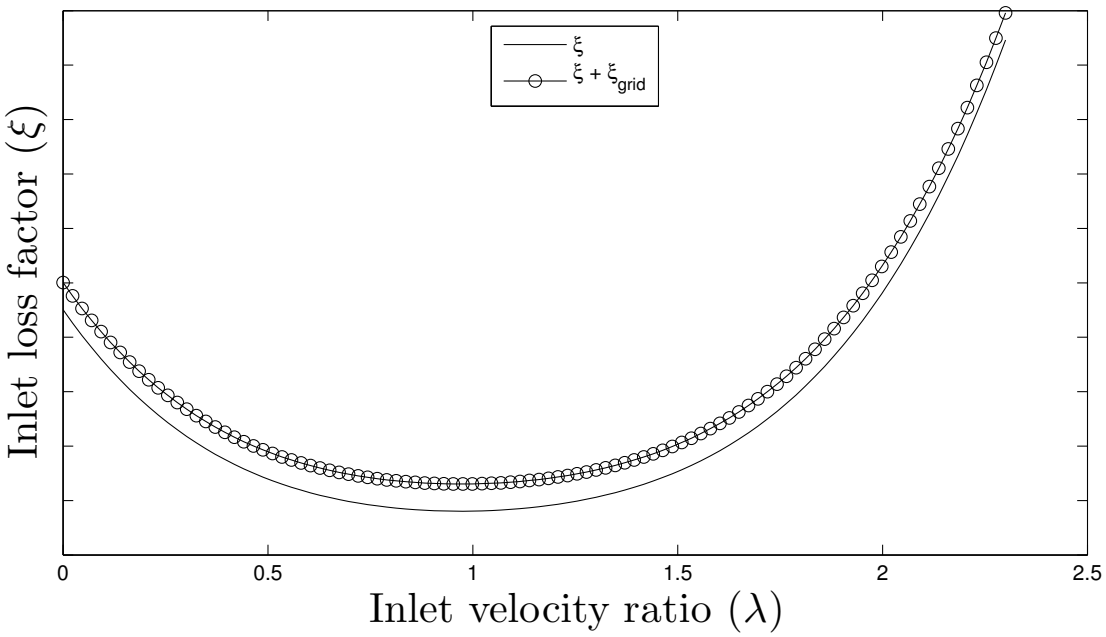

Figure 6.2: Plot of the inlet loss factor polynomial.

$$\dot{E}_3 = \dot{E}_1 - \frac{\xi E_1}{\lambda^2} \tag{6.18}$$

$$\dot{E}_3 = \dot{E}_1 - \frac{\xi \frac{1}{2}\rho V_1^2 \dot{Q}}{\left(\frac{V_1}{V_3}\right)^2} \tag{6.19}$$

$$\dot{E}_3 = \dot{E}_1 - \xi \frac{1}{2}\rho \dot{Q} V_3^2 \tag{6.20}$$

The duct head loss is the energy loss from point 1. to 3. given in meters.

$$h_{duct} = \frac{\dot{E}_1 - \dot{E}_3}{\dot{Q}\rho g} \tag{6.21}$$

Pump Elevation and The Pressure Before The Pump

The head loss caused by the nozzle (the pump outlet, point 6.) elevation above sea level is h_2 in figure 3.1. When the boat is planing h_2 is approximated as dh and when the boat is in bollard pull operation the nozzle is submerged making the elevation loss zero (as it is counteracted by a positive pressure at the inlet).

The pressure at point 3. (figure 3.1) is determined using the energy equation [Carlton, 2007] and the known pressure losses in the duct.

$$P_1 + \frac{1}{2}\rho V_1^2 = P_3 + \frac{1}{2}\rho V_3^2 + (h_{duct} + h_2)\rho g \quad (6.22)$$

$$P_3 = P_1 + \frac{1}{2}\rho V_1^2 - (h_{total})\rho g - \frac{1}{2}\rho V_3^2 \quad (6.23)$$

The resulting losses and pressures are presented in section 6.3 for a number of operational points.

6.3 Key Results

In this section the key results relevant for the blade design and pump benchmarking are presented.

The two main operational points of relevance are the transit design speed of 20 knots and the bollard pull condition. The flow rate of these conditions are presented in table 6.1. The flow rate achieved at the bollard pull condition ($V_0 = 0$ knots) is representing the minimum achievable flow rate (and highest head rise) at a given blade loading and rotation speed.

Table 6.1: *Design conditions.*

Vessel speed (V_0)	[knots]	0	20
$\dot{Q}$	[m^3/s]	0.28	0.29
$\dot{Q}_e$	[-]	1.07	1.13

The flow rate ($\dot{Q}$) is normalised ($\dot{Q}_e$) by equation 6.24, in which n is the speed of revolution in rounds per minute and d_{imp} is the impeller diameter. Q_e is presented as unitless to avoid confusion (the unit is $[rpm/s]$).

$$\dot{Q}_e = \frac{\dot{Q}}{\frac{n}{100} d_{imp}^3} \quad (6.24)$$

This normalisation represents a pump with a 1 m diameter running at 100 rpm. This is a Rolls-Royce standard for normalisation of the flow rate.

A number of operational points are chosen to establish a benchmark for the performance of the pump design. The CFD analyses of the pump are then performed at the same operational points.

The key results used for the pump benchmarking and design corrections are the effective head rise, i.e. the thrust and the flow rate. These key results are presented in table 6.2, the effective head rise is plotted in figure 6.3. The figure visualizes the portion of the required total head rise caused by head losses outside of the pump. The required head rise at the bollard pull condition is so much larger than that of the 20 knots condition that the vessel top speed is expected to exceed the design speed of 20 knots. The benchmarking therefore includes operational points equivalent to a top speed of 26 knots.

Table 6.2: Key results from the mathematidal model

V_0	[knots]	0	19	20	21	22	23	24	25	26
T	[kNm]	4.00	1.54	1.52	1.51	1.50	1.49	1.49	1.50	1.51
H_{effect}	$[m]$	12.15	7.28	7.30	7.33	7.38	7.45	7.54	7.65	7.78
$h_{total\ loss}$	$[m]$	1.97	0.23	0.25	0.27	0.30	0.33	0.36	0.39	0.43
V_3	[m/s]	9.3	9.6	9.8	10.1	10.3	10.5	10.8	11.0	11.3
$\dot{Q}$	[kg/s]	0.28	0.29	0.29	0.30	0.31	0.31	0.32	0.33	0.34
$\dot{Q}_e$	[−]	1.07	1.11	1.13	1.16	1.18	1.21	1.24	1.27	1.30

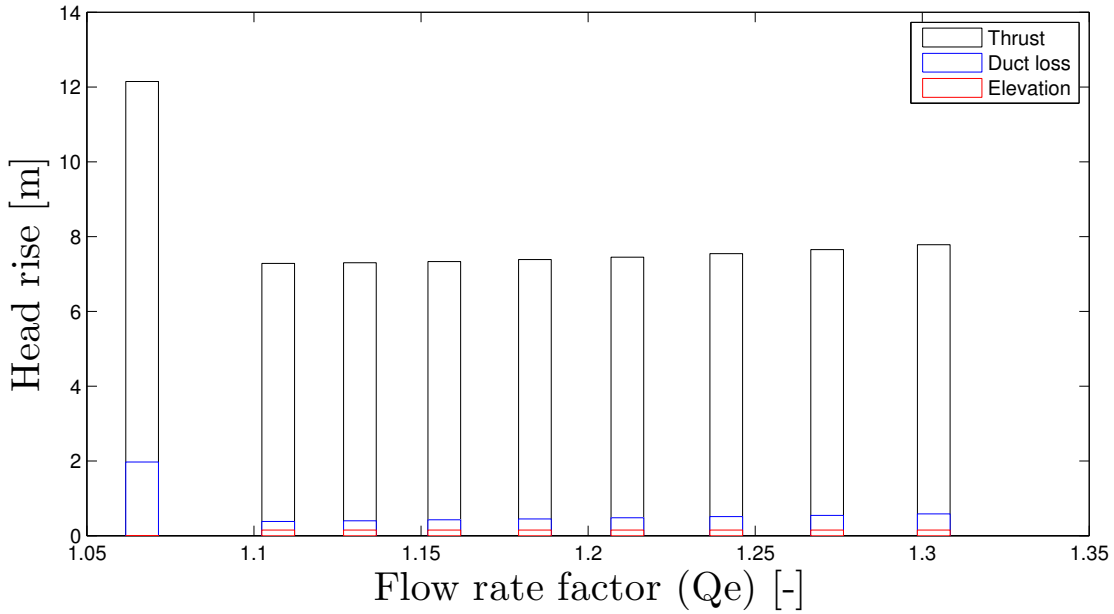

Figure 6.3: Plot specifying the head rise required to produce the necessary thrust.

It is clear from figure 6.3 that around 20% of the head rise needed to produce the bollard pull thrust is related to the duct losses.

6.3.1 Maximum Efficiency Prediction

The expected efficiency of a standard pump is estimated based on the specific speed and the pump type. The specific speed is defined in [Brennen, 1994, p28, equation 2.22], here shown in equation 6.25. Ω is the shaft rotational speed in rad/s, $\dot{Q}$ is the volume flow in m^3/s and H is the effective head rise (H_{effect}).

$$N = \frac{\Omega \dot{Q}^{\frac{1}{2}}}{(gH)^{\frac{3}{4}}} \tag{6.25}$$

For the pump considered here, the design specific speed at 20 knots is $N_D = 2.78$ based on the results from 6.2. This should according to [Brennen, 1994, p32, figure 2.8] (copied to figure 6.4 for easy reference) equal an estimated maximum efficiency of 70% for an axial flow pump. In [Brennen, 1994] axial pumps generally have a lower efficiency than mixed flow pumps operating at similar specific speeds, other sources (e.g. [Bulten, 2008]) are, on the contrary, indicating that similar efficiencies are achievable. However these similar efficiency are achieved with a axial flow pump running at a lower specific speeds than an axial pump usually does.

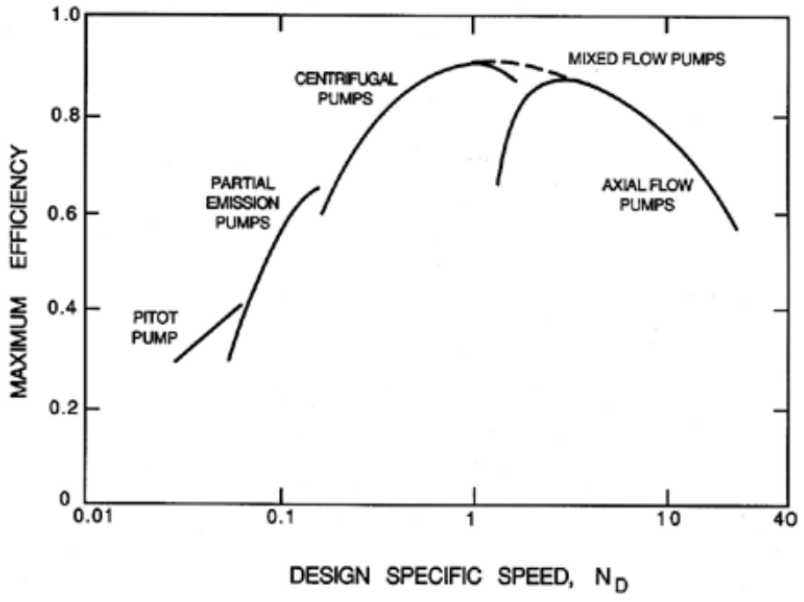

Figure 6.4: Plot of performance prediction for pumps of varying type. Source: [Brennen, 1994, p32, figure 2.8].

6.3.2 Engine Load

From the key results the required torque is estimated for a number of operational points. In table 6.3 the ideal torque (τ_{min}) and the required torque at 70% pump efficiency is

shown for the pump running at 3500 rpm and a nozzle and impeller diameter ratio of 80%.

Table 6.3: The ideal engine torque and the torque required at 70 per cent pump efficiency.

V_0	[knots]	0	19	20	21	22	23	24	25	26
τ_{min}	[kNm]	90	56	57	59	61	63	65	68	70
$\tau_{min\ \eta_p=0.7}$	[kNm]	128	80	82	84	87	89.00	93	96	101

From this table it is clear that the rim engine is able to produce the head rise needed if a sufficiently high pump efficiency is reached, but only just. It is also apparent that the bollard pull condition is the most power consuming operation of the vessel.

6.4 Discussion of Model

It is obvious from table 6.2 that the main challenge is to produce the 12.3 meters head rise demanded by the bollard pull condition. The high head rise is related to a high thrust requirement and a large head loss at the inlet.

The model is in general useful for testing the impact of smaller design alterations on the pump requirements. The diameter ratio of the nozzle outlet is variable along with the rpm of the pump, making it possible to adjust the required torque to match the engine limitations. It is evident from table 6.3 that the engine can deliver power to achieve specified bollard pull thrust if a pump efficiency around 70% is reached.

The model is based on rough estimates, both for the head losses and for the thrust prediction. It is a good basis for the conceptual design, but experimental or CFD data predictions of both the inlet losses and the hull resistance are necessary for the final production design of the pump.

The efficiency predicted is low compared to other axial pumps, axial pumps are however usually designed for larger specific speeds. The expected efficiency would be around 85%-89% if the specific design speed of the pump would have been around five (see equation 6.25). The specific speed of the pump could be increased by increasing the rotational speed to 4000 rpm, but it would only increase the specific speed to around 3. The efficiency prediction method is based on old shaft driven designs (the original source data used for figure 6.4 is from 1981) and the resulting efficiency will deviate from this prediction as the pump is rim driven and hubless. The efficiency prediction is however useful for benchmarking the pump performance.

7 Steady Flow CFD Pump Model

The set-up of the computational fluid dynamics model for the steady state analysis is presented in the following sections. The model is build upon the methods specified in section 5.2.

The steady flow model is used to test the effect of the design changes throughout the design phase.

The steady flow simulation set-up is displayed in figure 7.1, this set-up is generally used to get an indication of the pump performance at a low computational cost, see [Aartojärvi and Heder, 2008; Bulten, 2008].

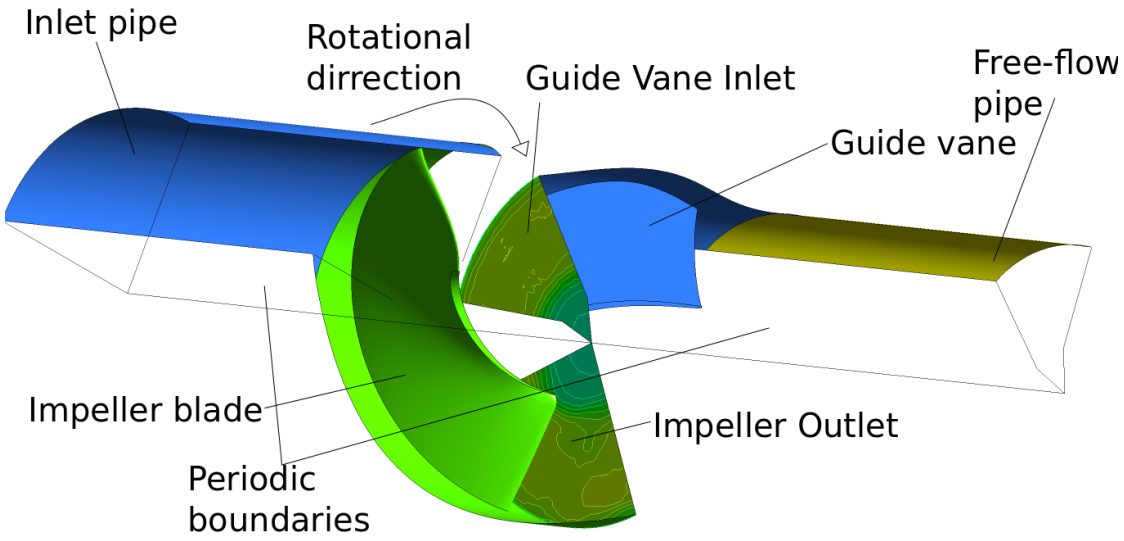

Figure 7.1: Steady flow simulation set-up. Blue: Stationary walls. Green: Rotating impeller blade and shroud. Yellow: Free flow pipe.

The set-up consists of two computational domains; one for the impeller (e.g. in figure 7.2b) and on the for guide vane (e.g. in figure 7.2a).

The computational cost is minimised by only having to simulate one blade in each domain which is possible because of the of the pump symmetry. The volume flows in the domains are not of same value as there are four impeller blades and seven guide vanes. A mixing plane is introduced to cope with this difference. The mixing plane exchanges

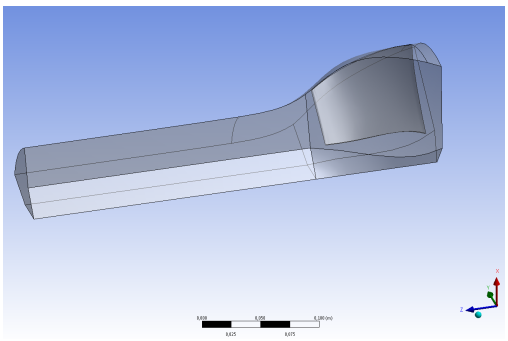

(a) Computational domain for the guide vane, Case 1.

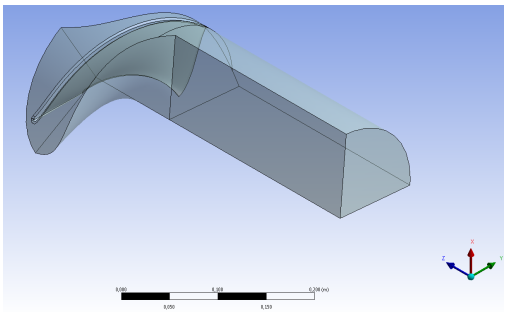

(b) Computational domain for the impeller blade, Case 1.

Figure 7.2: example of computational domains.

information about the averaged pressure and velocity at a given radius between the upstream area (the impeller outlet) and the downstream area (the guide vane inlet). This insures energy and mass conservation throughout the total volume of the pump. The dynamic interaction between the impeller and guide vane blades are, however, lost as their relative positions are constant and the computation is therefore independent of time.

7.1 The Computational Grid

The computational domains (figure 7.2) are divided into a number of small cells creating the computational grid. Both grids are constructed with similar grid specifications to ensure a stable computation. The amount of cells in and the quality of the mesh are controlled by a maximum and minimum cell size as well as a minimum cell skewness(the angle between the walls of the cell). An example of the resulting mesh is shown in figure 7.3. The detailed mesh specifications are found in appendix C.

The rotational symmetry of the grid is ensured by controlling the cells which defines the two periodic boundaries (the walls meeting in the centreline, see figure 7.1).

A sufficient y-plus value is ensured by controlling the size of the cells in the boundary layer.

7.1.1 Simplified Grid Dependency Study

A minor mesh dependency study is conducted to establish the solution dependency of the computational grid, the results are shown in table 7.1. The study is conducted on the Case 1. with three different flow rates. Mesh no. 2 in table 7.1 has roughly half the volume of each cell compared to mesh 1.

The grid dependency study shows a maximum result difference around 1% between the two meshes. With mesh no. 2 resulting in higher pump performance. In a full mesh dependency study a number of meshes, each with half the average cell volume, should be

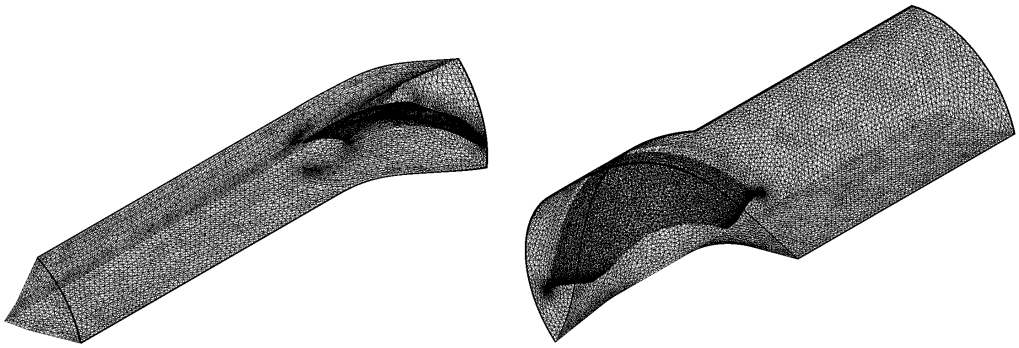

(a) The mesh used for the guide vane domain, Case 1.

(b) The mesh used for the impeller domain, Case 1.

Figure 7.3: Example of computational mesh.

Table 7.1: Simplified grid dependency study for case 1.

Mesh no.		1	2
Impeller mesh:			
Number of elements	[-]	812,775	1,549,961
Minimum element size	[mm]	0.236	0.130
Maximum element size	[mm]	45.19	25.07
Maximum face size	[mm]	5	2.89
Guide vane mesh:			
Number of elements	[-]	296,604	526,052
Minimum element size	[mm]	0.059	0.0339
Maximum element size	[mm]	11.7390	6.7718
Maximum face size	[mm]	5	2.89
Mesh differences	mesh 1 / mesh 2		
	Bollard pull	20 knots	25 knots
Torque ratio		1.0100	1.0119	1.0127
Head rise ratio		1.0003	1.0030	1.0032
Pump efficiency ratio		0.9900	0.9908	0.9900

investigated until the difference is regarded insignificant. A 1% difference is a significant difference. The performance impact of the mesh dependency is however avoided by using meshes with similar settings, thus ruling out differences caused by differences in mesh sizing. A small grid dependency is acceptable when using this strategy to avoid its

impact on the design changes.

A more refined, and thereby more correct solution or, a model scale test should be conducted for the final design. The development of the pump is in no way hindered by a small grid dependency as long as the grid properties are relative comparable, a full grid dependency study is therefore beyond the scope of this project.

7.2 Boundary Conditions

The boundary conditions are stated in table 7.2.

Table 7.2: Boundary conditions.

1. Walls and blades	*No slip condition.*
2. Free-flow pipe	*Slip condition.*
3. Impeller blade inlet	*Velocity inlet*
4. Guide vane outlet	*Pressure outlet*
5. Axial domain boundaries	*Periodic boundaries.*

The slip condition in the free-flow pipe (boundary 2.) is emulating a free jet. At the velocity inlet (boundary 3.) the flow rate through the system is defined as a constant average velocity. Changing this point changes the operation point of the pump, making it possible to produce a $Q - H$ plot for the pump.

The periodic boundaries (5. in table 7.2) are simulating the neighbouring blades by projecting the output from the one boundary and to the opposite boundary. This is possible as the mesh on both periodic boundaries are similar [Versteeg and Malalasekera, 2007, p. 281].

7.3 Calculation Settings

The main calculation settings used for the analysis in Ansys Fluent is summarised in table 7.3.

Table 7.3: The calculation setting used for the steady analysis in Ansys Fluent.

Turbulence model	SST $k-\omega$
Solution methods	
Pressure- Velocity Coupling	
Scheme	SIMPLE
Spatial Discretization	
Gradient	Least Square Cell Based
Pressure	Second Order
Momentum	Second Order Upwind
Turbulent Kinetic Energy	Second Order Upwind
Specific Dissipation Rate	Second Order Upwind
Mixing plane	
Averaging method	Area
Under-Relaxation	0.05
Interpolation Points	200

7.4 Discussion of the Model

The model is in general an efficient way to get a performance prediction, and useful for design iterations. The model does not include the dynamic effects of the impeller moving in relation to the guide vane. This results in a constant blade torque and a constant effect of the guide vane at a given flow rate.

It is possible to reduce the mesh dependency of the solution by increasing the mesh resolution, this would, however, increase the computation time and the gained accuracy would have little impact on the design process. The system is normally tested in an experimental set-up for the final performance evaluation it is therefore more interesting to run a transient analysis, to capture the dynamic effects, than to improve the mesh resolution.

The flow through the pump is dynamic, and the relative position of the guide vane compared to the impeller blade causes fluctuations in the pump performance. It is therefore possible that the steady state simplification is presenting a local efficiency extreme. A transient analysis is therefore conducted in order to achieve a more accurate time averaged pump performance.

This page is intentionally left blank.

8 Transient Flow CFD Pump Model

The unsteady flow CFD model is used to make a more detailed analysis of the flow through the pump. The time averaged performance calculated using an unsteady flow analysis (a transient analysis) is more accurate than that of the steady state analysis.

The transient analysis set-up is presented in figure 8.1. A similar set-up has been used to simulate an axial waterjet pump in [Bulten, 2004] and [Bulten, 2007]. The turbulent flow models used in these analyses are respectively a standard $k-\omega$ and a standard $k-\epsilon$ model. The SST $k-\omega$ turbulent flow model used in this thesis should have a higher accuracy than both methods (see section 5.2).

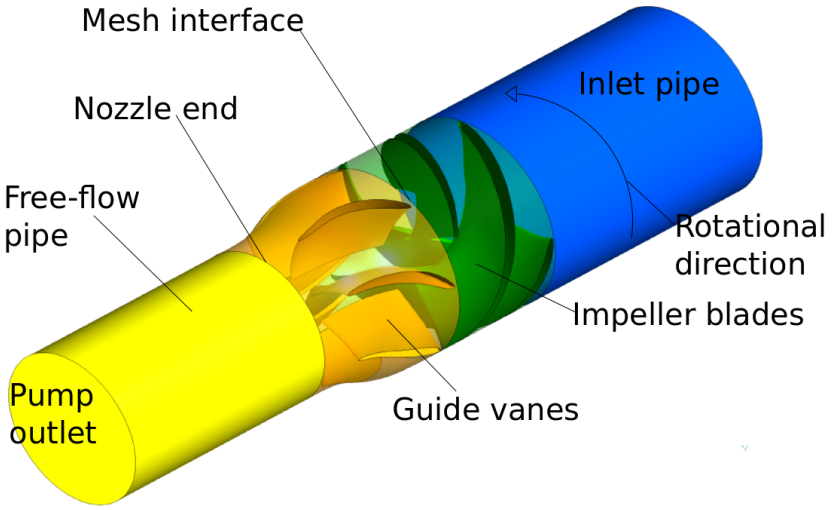

Figure 8.1: Unsteady flow analysis set-up.

The set-up is constructed using the computational domains presented in figure 7.2. The impeller domain is copied four times and the guide vane domain seven times in order to create the full pump domain.

8.1 The Computational Grid

The grid used for the steady analysis is the base of the transient computational grid. The grid is constructed by copying and rotating the impeller and guide vane grid to construct a mesh covering the full pump volume. The grid is constructed in this manner in order to avoid meshing problems. Rolls-Royce has previously experienced problems when meshing blades in more than one radial direction, this method of copying the mesh is therefore used to ensure a good mesh with properties similar to that of the steady mesh.

As the grid used is the same as used in the steady analysis the simplified grid dependency study is still, to some extend, valid. The grids are combined and fused using Ansys Fluent, the final computational grid is shown in figure 8.2.

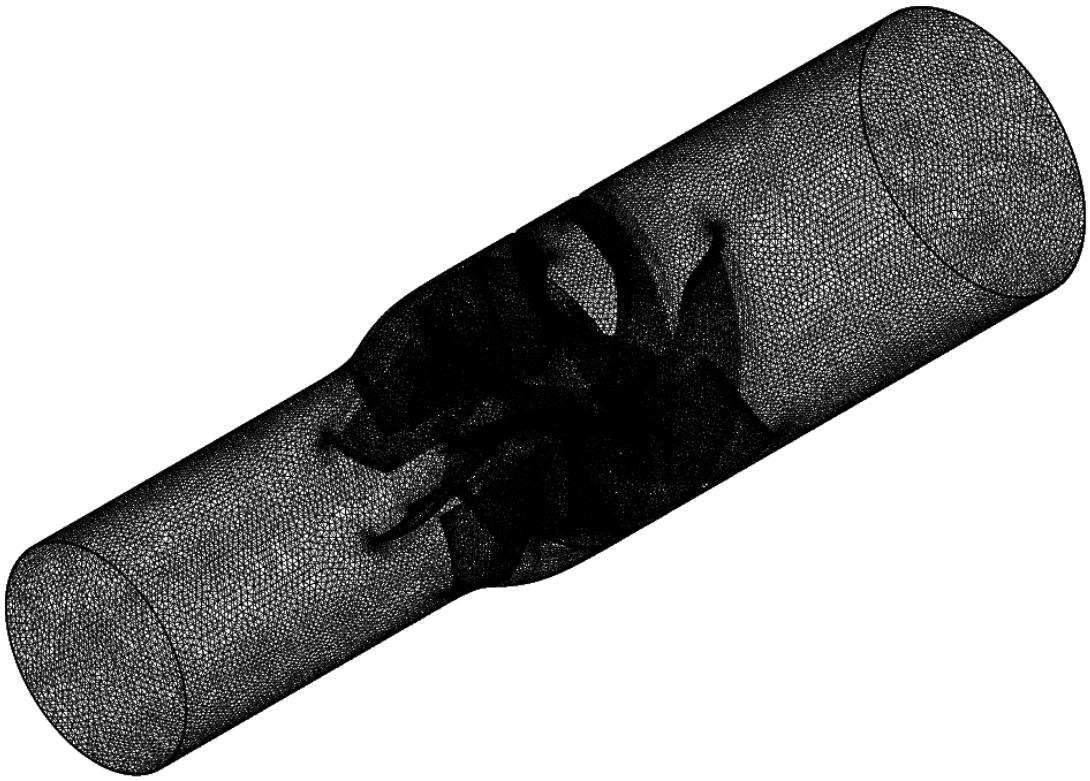

Figure 8.2: The figure visualises the mesh used for the transient analysis of the unsteady flow through the pump.

8.2 Boundary Conditions

The boundary conditions are stated in table 8.1. They are very similar to the ones used in the steady analysis. The 5. boundary condition from 7.2 is no longer needed as the full

computational grid is modelled and the mesh containing the impeller is actual rotating around the flow axis. The rotation of the impeller grid creates the time dependency of the computation as the relative position of the impeller blades compared to the guide vanes is time dependent.

Table 8.1: Boundary conditions.

1. Walls and blades	*No slip condition.*
2. Free-flow pipe	*Slip condition.*
3. Impeller blade inlet	*Velocity inlet*
4. Guide vane outlet	*Pressure outlet*

8.3 Calculation Settings

The main calculation settings used for the transient analysis in Ansys Fluent is summarised in table 8.2. Here the main difference from the steady flow analysis is the use of a second order implicit scheme to model the time stepping in the SIMPLE solver. The rotation of the impeller mesh is handled by a mesh interface (A fluent function handling the information transfer between independent grids) between the guide vane outlet and the impeller inlet.

Table 8.2: The calculation setting used for the transient analysis in Ansys Fluent.

Turbulence model	SST $k-\omega$
Solution methods	
Pressure- Velocity Coupling Scheme	SIMPLE
Spatial Discretization	
Gradient	Least Square Cell Based
Pressure	Second Order
Momentum	Second Order Upwind
Turbulent Kinetic Energy	Second Order Upwind
Specific Dissipation Rate	Second Order Upwind
Transient Formulation	Second Order Implicit
Mesh Interfaces	impeller outlet - guide vane inlet

8.4 Multiphase Flow Model

The mixture flow model, presented in section 5.2, is used to model cavitation in the pump. The cavitation model is based on a transient analysis and follows the same settings as the transient analysis with some added configurations presented in table 8.3. The model is sensitive and the computation diverges easily, the analysis is therefore started with very small time steps and gradually increased until a similar time step as that of the transient model is used.

8.4.1 Settings

Table 8.3: The calculation setting used for the transient multiphase analysis in Ansys Fluent. Changes from table 8.2 is marked with *talic*.

Turbulence model	SST $k-\omega$
Multiphase model	*Mixture*
Phases	
Phase 1 - Primary Phase	*Water-liquid*
Phase 2 - Secondary Phase	*Water-vapour*
Vaporization pressure	2.3 kPa
Bubble Number Density	10^6
Cavitation model	*Schnerr*
Solution methods	
Pressure- Velocity Coupling Scheme	SIMPLE
Spatial Discretization	
Gradient	Least Square Cell Based
Pressure	Second Order
Momentum	*First Order Upwind*
Volume Fraction	*First Order Upwind*
Turbulent Kinetic Energy	Second Order Upwind
Specific Dissipation Rate	Second Order Upwind
Transient Formulation	Second Order Implicit
Mesh Interfaces	impeller outlet - guide vane inlet

8.5 Discussion of the Model

The unsteady model produces a more accurate prediction of the performance and the cavitation properties of the pump than the steady flow analysis. The model makes it possible to analyse the variation of the pressure on the blades, thereby giving a more realistic evaluation of the cavitation properties. The cost of the computation is significantly higher compared to the steady analysis, and the analysis is therefore only conducted for the final concept design.

The mesh from the steady state analysis is used and the grid dependency study is assumed to cover the use in the transient analysis. The grid does however react differently when used in the transient analysis, a separate grid dependency study should therefore be conducted at a later stage. The grid is however estimated to be sufficiently independent for the performance analysis in this thesis, based on the steady state grid dependency study and comparisons with gird used in other studies [Bulten, 2008].

The multiphase flow model is used to achieve an indication of the cavitation properties of the pump at certain operational points. The computation helps visualise the effects and consequences of cavitation. The accuracy of the computation is low and the results are only used as early indications of possible cavitation issues.

This page is intentionally left blank.

9 Blade and Pump Design

The majority of the project time has been used working on and improving the blade design. The final blade design is presented in this section with some comments on major changes throughout the design phase. The design of the impeller and guide vane blades are initially based on results from the mathematical model presented in section 6.3 and from the specifications in table 1.2.

When an initial design is created in TD1 the performance of the pump is evaluated using the steady flow CFD model, presented in section 7. The design parameters, presented in section 5.1.2, are then corrected based on the results from the CFD analysis in order to create a blade that performs better. This iterative process is ongoing until a satisfying design is achieved. Some of the design parameters are kept constant for the final iterative design process. These parameters are no. 1 through 4 presented in section 5.1.2.

The design parameters used are presented in the following sub sections.

9.1 Constant Design Parameters

The following parameters are changed from the early design phases, but kept constant through the final part of the design process. The main changes from the early design stage are a decrease in the impeller diameter (New information from the engine manufacturer), an increase of the diameter of the nozzle (from 60% to 80% of the impeller diameter) and an increase of the rotational speed of the impeller blade. These major changes are based on improvements of the mathematical model, early stage steady flow CFD results, which predicted a lower than expected efficiency, and new information from SSRS.

9.1.1 The Meridional Channel Shape

The meridional channel shape is presented in figure 9.1. This channel shape is created using the TD1 user and application manual, see [TD1, 2012b] and [TD1, 2012a]. The channel shape is simple and the nozzle design is created using a simple s-function in Matlab. The channel shape is kept simple in order to reduce the complexity of the blade design and thereby the difficulties related to creating a functioning hubless pump. Tests with TD1 have shown a great sensitivity to changes of blade's axial lengths at the hub. The blade design code in TD1 simply diverges if the axial length of the hub is changed compared to the axial length of the shroud. This sensitivity appears to be related to the

cylindrical hub as the problem is non-existing in regular axial pump designs (according to tests and Rolls-Royce experience).

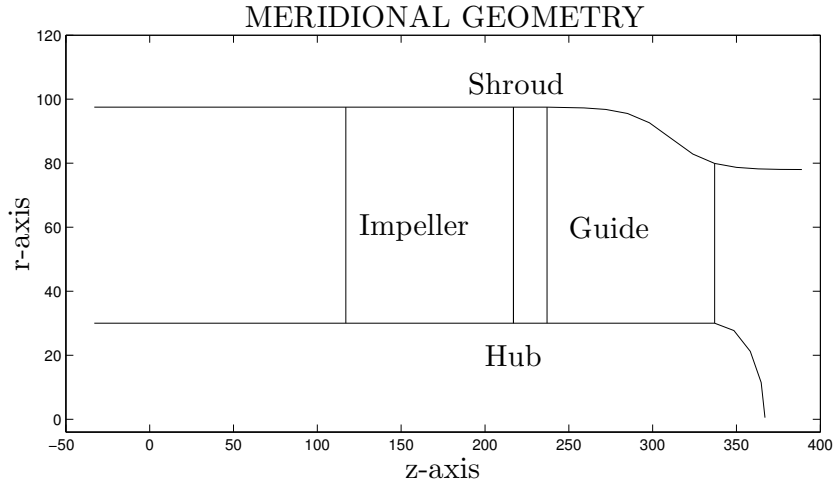

Figure 9.1: Meridional plot of the channel shape. The hub is included as it is a requirement for the input to TD1.

A standard axial waterjet pump have a more bulky hub used to accelerate the average axial flow velocity and to create room for a bearing (see figure 3.2a). The lack of flow acceleration, in combination with the off loading near the hub, has shown to create some difficulties when loading the hubless impeller blade.

9.1.2 The Thickness Distribution

The thickness distribution used for both the impeller and guide vane blades is developed and used by Rolls-Royce. It is, however, reversed for this specific design to create sufficient strengthening at the shroud. The thickness distribution at the hub, the mid and the shroud section is plotted with a straight camber line in figure 9.2.

The cavitation performance of a blade is controlled among other by the thickness distribution as this is used to control the flow velocity over the blade. The thickness distribution has good cavitation properties according to Rolls-Royce. A modification of the distribution is time consuming compared to the performance gains and it is therefore kept constant throughout the design process.

The leading and trailing edge, which appear blunt on figure 9.2, are modified at a later stage in the design process (section 9.3).

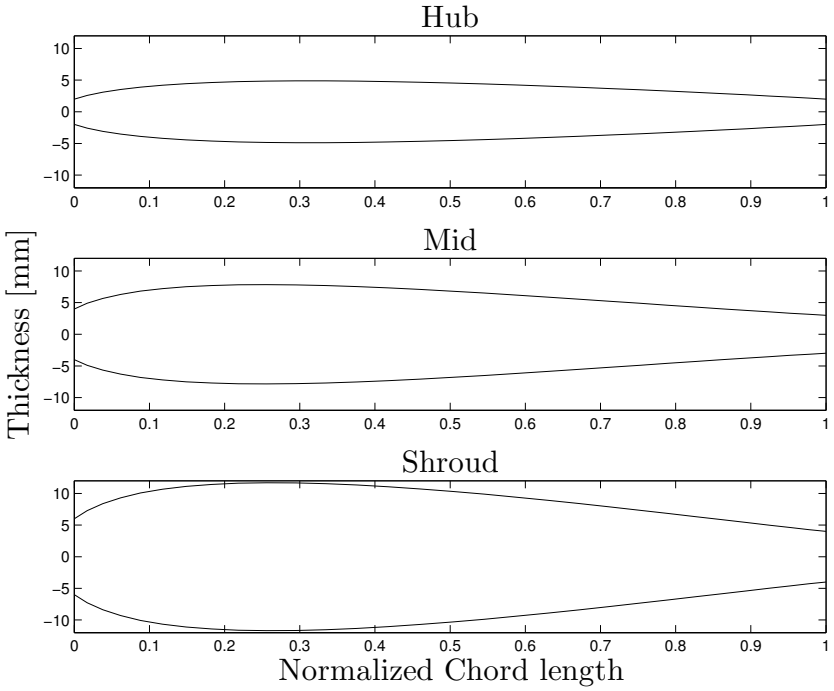

Figure 9.2: Plot of the thickness distribution in three spanwise positions. The leading and trailing edge is modified at a later stage.

9.1.3 Fluid Properties and Design Specifications

The specifications used for the impeller and guide vane blade design (shown in table 9.1.) are chosen based on results from the mathematical model, see table 6.3, 6.2 and the specification in table 1.2.

Table 9.1: *Design specifications input for TD1.*

Impeller		
Rotational speed	3500	rpm
Reference speed at shroud	35.74	m/s
Average axial inlet flow velocity (V_3)	9.83	m/s
Guide vane		
Rotational speed	0	rpm
Reference speed at shroud	35.74	m/s
Average axial inlet flow velocity (V_4)	10.70	m/s

The boat is mainly operating in sea water, however, the fluid properties are based on fresh water at 20 ° C, see table 1.2. The differences of the fluid properties are however

negligible and the experimental tests are performed with fresh water as well.

It is possible to specify a pump inlet velocity distribution, however as the pump has no shaft the variation in the velocity field at the impeller inlet is much smaller than that of a regular pump. Rolls-Royce usually uses an average velocity distribution as the effects of cavitation are difficult to predict, and furthermore, the advantages of using a distributed intake velocity are quickly lost in added cavitation. An average pump inlet velocity is therefore also defined for this design, see table 6.1. The guide vane inlet velocity (or the outlet velocity from the impeller (point 4. figure 6.1)) is higher than the average velocity through the pump as the flow in the center is much slower resulting in a higher flow velocity in the area covered by the impeller and guide vane blades (see figure 9.3 and table 6.1).

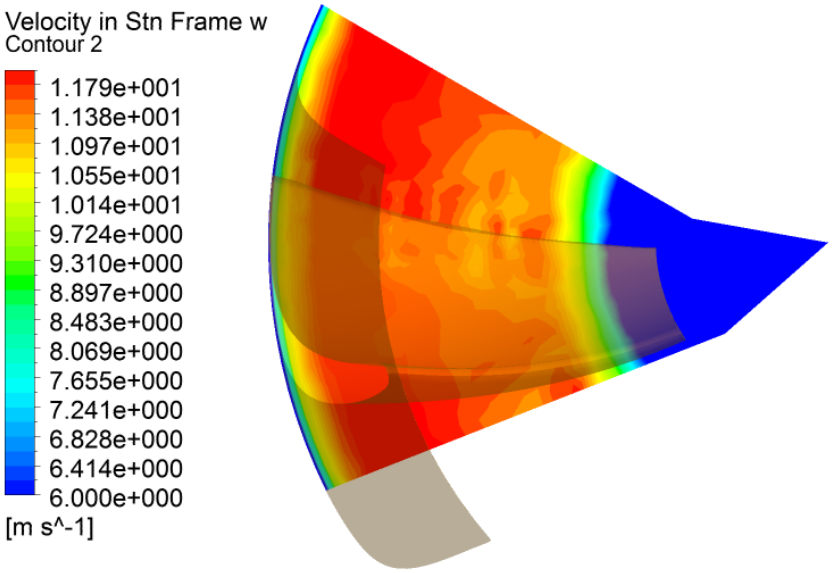

Figure 9.3: The contour figure showing the axial velocity field entering the guide inlet. The orange blade is a guide vane and the grey is the nozzle wall. The direction of the look into the pump is upstream.

The specified design flow rate is set to the flow rate corresponding to thrust production able to sustain a velocity of 20 knots. The impeller blade is however mainly loaded for the production of the bollard pull thrust as this requires a much higher head rise than the 20 knot speed. However the design point of 20 knots is chosen as a test shows this yields a high overall efficiency of the pump. The test shows that having the design flow rate equal to the flow rate at the bollard pull condition results in a significant decrease of the efficiency at the higher flow rates, and the increase in efficiency at the bollard pull condition is insignificant.

9.1.4 Number of Blades

The number of blades are specified in table 1.2: four impeller blades and seven guide vanes. The main reason for the low number of blades is to maintain a simple pump geometry to reduce the risk of rope entanglement. This is an area of the design process in which efficiency gains are possible. Studies have shown that changing the amount of blades (both impeller and guide vane blades) can have a positive impact on the pump performance [Yang et al., 2008]. The number of blades is kept constant in order to simplify the design process, changing the amount of blades would mean a redesign of the blade loading.

9.2 Non-Constant Design Parameters

The remaining three design parameters of TD1 are related to the loading of the impeller and guide vane blades. The final iterative design process is focused on these tree design parameters. These parameters are used to control the pump performance, efficiency and cavitation properties. A high efficiency often means bad cavitation properties, consequently, a compromise must be established.

9.2.1 Vorticity Distribution

The vorticity distribution is determining the spanwise loading of the blade. It is kept as a simple linear distribution with a heavy loading on the shroud and the lowest possible loading at the hub in order to reduce the pressure leaks. A rough estimate of the average blade vorticity, see [TD1, 2012a, p.22], is used to create the first blade design. The vorticity distribution of this initial blade design is corrected using results from the steady flow CFD in order to adjust the blade loading and achieve the necessary head rise.

A plot of the resulting vorticity distribution is found in figure 9.4a for the impeller and in figure 9.4b for the guide vane. Note that the loading on the leading edge of the impeller and the trailing edge of the guide vane is zero. The zero represents a flow with no vorticity. The pump inlet flow is assumed without any swirl or vorticity and the guide vane is designed to deliver a jet with no swirl at the nozzle outlet, thus transforming all energy bound in the swirl into axial flow energy. The energy is mainly added to the water by introducing a swirl and thereby increasing the static pressure (which is lowered by the pressure losses prior to the pump inlet).

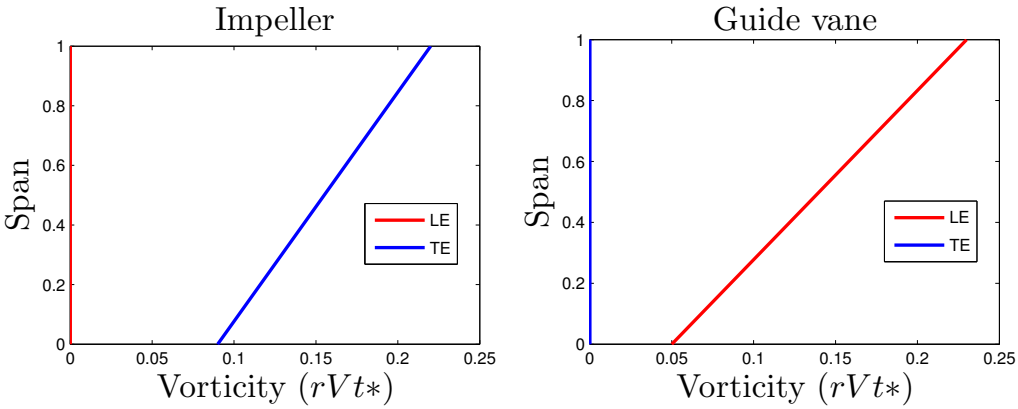

(a) Plot of the vorticity distribution for the final impeller design. Note that the vorticity is zero at the leading edge.

(b) Plot of the vorticity distribution for the final guide vane blade design. Note that the vorticity is zero at the trailing edge.

Figure 9.4: Vorticity distribution for the impeller and guide vane blade.

9.2.2 Blade Loading

The streamwise loading of the blade distributes the defined spanwise loading along the chamber line of the blade. The loading distribution dictates the pressure distribution on the suction and the pressure side of the blade. The pressure distribution determines the cavitation properties and the efficiency of the blade. The pressure distribution defines the boundaries of how the required change of the vorticity distribution should be achieved. A heavy loading impeller towards the leading edge results is an efficient blade with poor cavitation properties. A blade loaded towards trailing edge results in a blade with better cavitation properties, but lower efficiency ([Bonaiuti et al., 2010; Thad et al., 2008]). The blade loading controls the velocity of the flow over the pressure and suction side of the blade. The flow is accelerated rapidly when the blade is loaded at the leading edge, thus creating a low pressure region at which cavitation can occur and cover a large area of the following blade. The flow acceleration at the leading edge is reduced by loading towards the trailing edge.

The cavitation performance of the impeller and guide vane blades in off-design operation must be considered when assessing the total cavitation properties of the pump. The best cavitation properties are not necessarily obtained when the cavitation performance is best at the design point (20 knots - $Q_e = 1.13$). It is important that the pump has good cavitation performance in the crucial operational conditions such as the bollard pull condition, the blade design alterations are therefore based on a steady flow analysis of the full operational curve.

The final impeller blade design is loaded heavily towards the trailing edge at the shroud and more equally at the mid and hub (see figure 9.5). The impeller is loaded so that the required bollard pull thrust is reached, this leads to a low pressure area on the suction side of the impeller near the shroud. The aft loading helps distribute the loading

to reduce the low pressure area at the leading edge. There is however still a significant low pressure area where cavitation is expected.

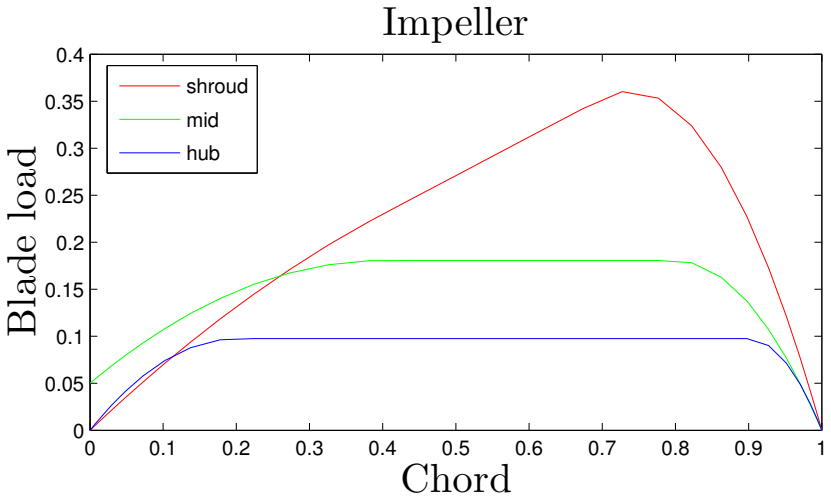

Figure 9.5: Plot of the resulting blade loading for the impeller blade.

The guide vane loading (figure 9.6) is based on efficient guide vane designs presented in [Bonaiuti et al., 2010], the loading is then modified to fit the impeller design resulting in a guide vane with a high efficiency and good cavitation properties. The guide vane is unloaded (actually negatively loaded) at the leading edge at the shroud to avoid cavitation at the leading edge and otherwise evenly loaded towards the trailing edge.

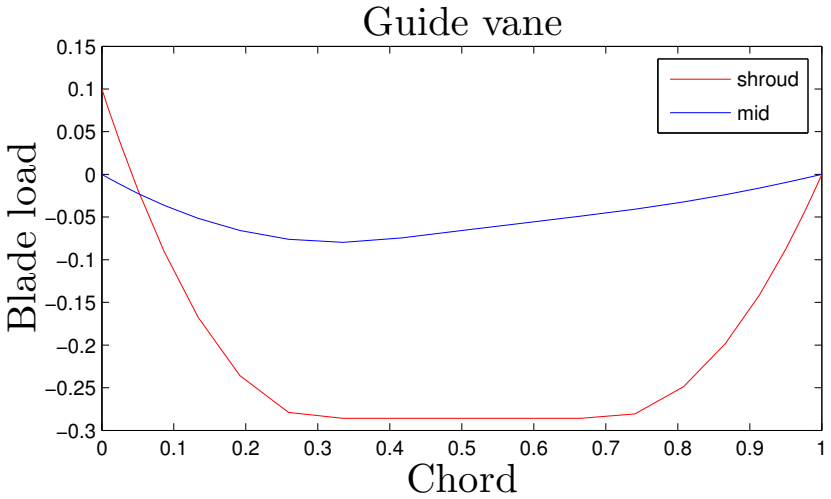

Figure 9.6: Plot of the resulting blade loading for the guide vane.

9.2.3 Stacking Condition

Stacking is usually used to control the cavitation performance of the guide vanes, see [Bonaiuti et al., 2010]. The effect of stacking for a hubless pump is however difficult to confirm, though some improvements of the trailing edge cavitation on the guide vane blade was observed. Stacking is used for both the impeller and guide vane blade. The stacking is leaning the hub of the blade against the rotation in order to increase the rope in pump performance of the pump. The effect of stacking is however limited as it is only used to define the leaning near the trailing edge.

9.3 Leading and Trailing Edge Modification

The trailing and leading edge is created using an elliptic shape. The shape is defined using a ratio that defines the length of the modification of the edge compared to the thickness of the blade (see equation 9.1 and figure 9.7 from [TD1, 2012b]).

$$Ratio = \frac{2L}{th} \tag{9.1}$$

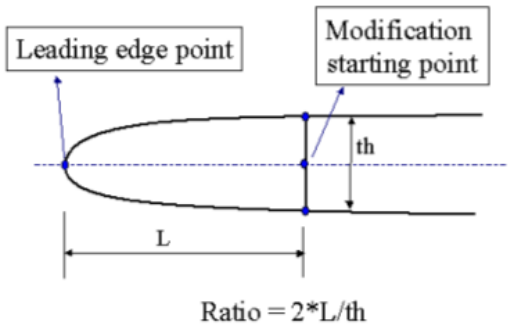

Figure 9.7: Figure explaining the use of the edge defining ratio. source: [TD1, 2012b]

The modification of the edges are defined at both the hub and shroud and the modification in between is found by linear iteration.

The ratio used is 6 at the leading edge at both the hub and shroud and 3 at the trailing edge. Similar ratios are used for both the impeller and guide vane design. This elliptic leading edge modification improves the cavitation properties of the impeller guide without altering the blade geometry significantly. The ratio defines the roundness of the edge. A high ratio results in a sharp blade with good cavitation properties at the design flow rate and a small ratio gives a rounder edge with good performance at varying angles of attack caused by varying flow rates. The ratios used for the blade design is medium resulting in a somewhat sharp leading edge. The ratios are chosen to improve the cavitation properties throughout the operational profile. This is a good option as the flow rate variation between the bollard pull and the transit condition are small and, a sharper blade will result in a improved cavitation performance for both conditions.

9.4 The Final Pump Concept

The final pump concept, impeller and guide vane blades are shown in figure 9.8. The initial CFD evaluation of the pump is showing that the pump deliver the needed thrust in both the bollard pull and transit operation. There are indications that the cavitation properties are unsatisfactory, it is, however, difficult to achieve better cavitation properties without reducing the loading on the blade. The detailed performance analysis is conducted for the final design, even though cavitation problems are expected. The requirements from the SSRS is the minimum requirements and other measures to improve the cavitation properties of the pump must be done as it is not an option to lower the bollard pull thrust.

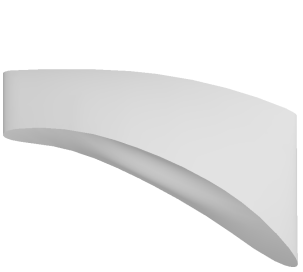

(a) Guide vane.

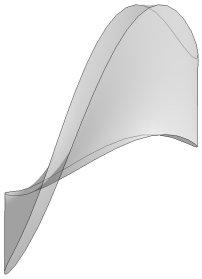

(b) Impeller blade.

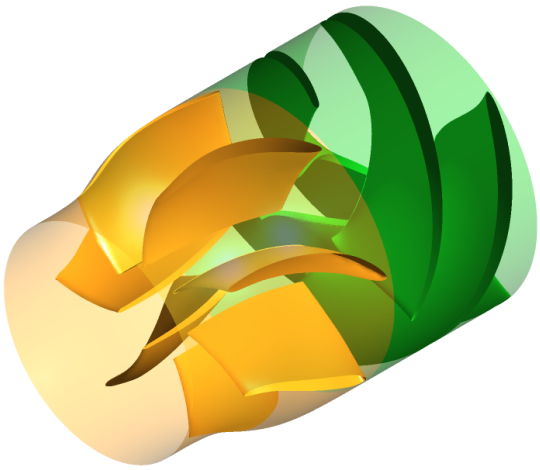

(c) Figure on the final concept pump with the nozzle and piping visualised.

Figure 9.8: The impeller blade and guide vane blade with modified leading and trailing edges are shown free and in connection with the final pump Case 1. configuration. The rotation of the impeller follows the right hand rule around the z-axis (blue arrow in the right hand corner of figure 9.8c).

This page is intentionally left blank.

10 Performance of the Final Pump Concept

The performance of the final concept design is evaluated using a number of analyses based on the CFD models presented in section 7 and 8. The performance of Case 1. and 2. pump configuration are compared, and the effect of the missing hub is analysed using Case 3. pump configuration. All three cases are analysed using a steady flow analysis. Case 1. is studied further using a transient analysis to evaluate the flow as time dependent. A multiphase flow model is added to the transient flow analysis to evaluate the cavitation properties.

The convergence of the results are confirmed using a convergence study.

10.1 Convergence Study

The convergence study is performed for all analyses in order to ensure that they all have converged. Convergence, as mentioned in section 5.2.9, is based on observations of the residuals and the torque on the system for the steady analysis. The convergence of the transient analysis is based on the residuals and the observation of a repetitive torque curve. The residuals are not exported from Ansys Fluent, only observed, as the convergence of the torque is a better indicator of the final calculation convergence.

An example of the study is given for the steady flow analysis of Case 1. in figure 10.1 and table 10.1. From this study it is evident that the analyses presented are fully converged. See appendix D for the full study.

Table 10.1: The standard deviation as permille of the mean torque value, see figure D.1

Case 1.										
Volume flow (Q_e)		1.09	1.11	1.13	1.16	1.18	1.21	1.24	1.27	1.30
Standard deviation	‰	0.21	0.15	0.01	0.01	0.04	0.03	0.36	0.91	0.61

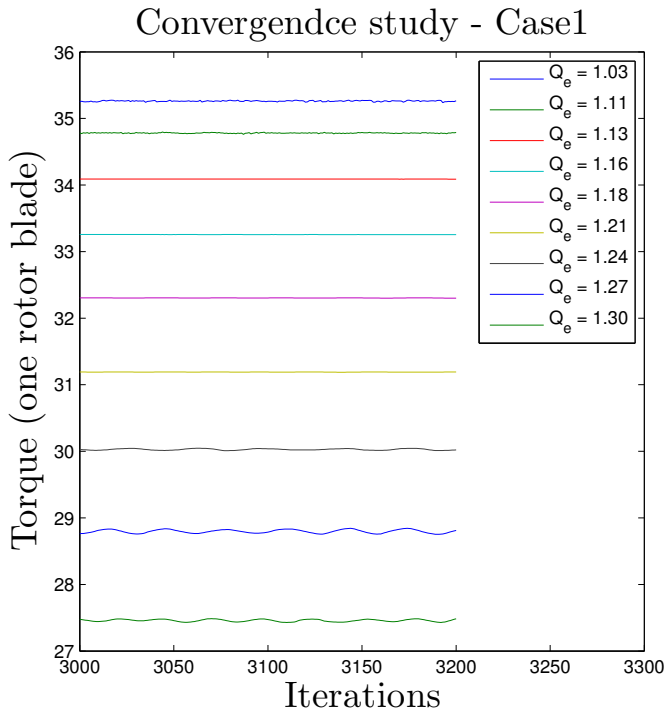

Figure 10.1: Plot of convergence study of Case 1. It is evident from the figure that the torque of the system is constant though with small fluctuations. Please note that this figure is based solely on the last 200 iterations displayed.

Convergence is, in general, reached for the transient analysis as well. However, the bollard pull condition never reached full convergence even though a great effort in adjusting the parameters of the model was done. It is believed that a grid refinement is needed in order to reach full convergence. The computation history of the unconverged bollard pull condition is displayed in figure 10.2. It is clear that large fluctuations are visual (figure 10.2a. The data used for to estimate the performance of the pump in the bollard pull condition is visualised in figure 10.2b, this is the last part of the computational history and it is well below the average value of the total computational history, this ensures that the performance results in a low head rise and the performance is estimated as conservative for the given condition.

The results from the bollard pull condition are still displayed in section 10.2.3, as they follow the trend on the computations at the other flow rates. The reader should, however, be aware of the uncertainties related to this particular operational point.

The bollard pull condition is critical for the performance analysis of the pump. However, the results of the (converged) transient cavitation analysis in combination with the steady flow analysis are enough to draw the necessary conclusions for the pump performance in the bollard pull condition.

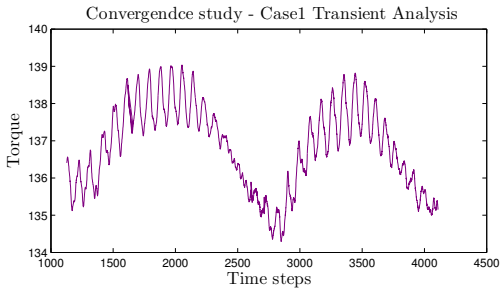

(a) Computation history of the transient analysis $Q_e = 1.09$. each time step is $5 \cdot 10^{-5}$

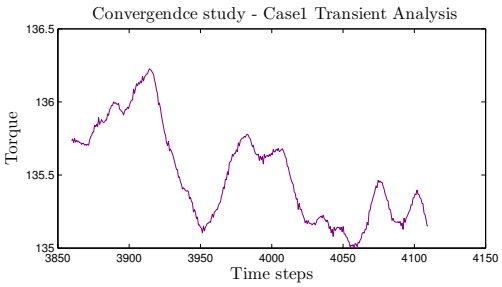

(b) Data used for time averaging of the bollard pull perfromance.

Figure 10.2: Computational history for the bollard pull condition.

10.2 Performance Results

In this section the results of the performance analysis of the final concept are presented and discussed. It is observed that the bollard pull produced by the pump is larger than specified (in table 1.2). The final and more detailed analysis of the concept design uncovered a minor error in the settings of the steady flow CFD model resulting in an artificially low blade loading. This error was corrected in the more detailed analysis presented here, resulting in a higher than expected blade loading. The result of the error leads to a bollard pull about 4% higher than needed, the pump design is, however, still regarded as a valid concept design. The energy model is used to find the new bollard pull thrust equilibrium for Case 1. and 2. The benchmark results displayed in table 6.2 are therefore constant for all other operational points than the bollard pull.

Clear definitions of the pump and impeller efficiency are needed in order to to evaluate the performance. The efficiency expression used in the post processing of the results is presented in section 10.2.1.

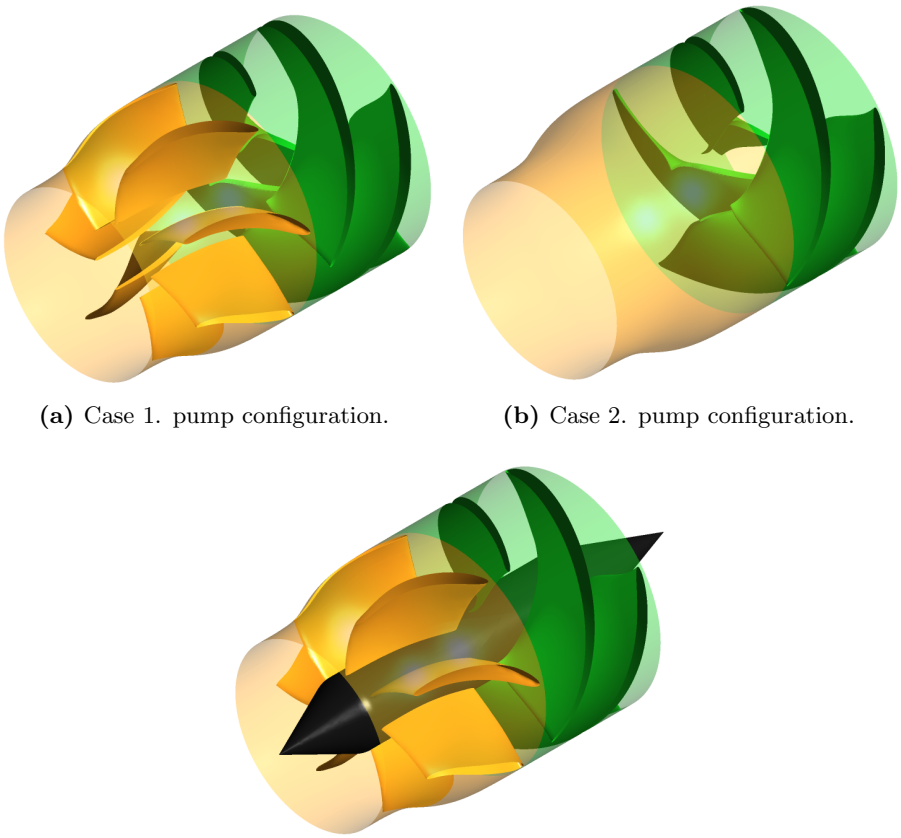

(a) Case 1. pump configuration.

(b) Case 2. pump configuration.

(c) Case 3. pump configuration.

Figure 10.3: The three pump configurations are displayed in 3D. The rotation is following the right hand rule for the flow direction (towards the nozzle). Note that the impeller is upstream of the guide vanes.

10.2.1 The Efficiency Definition

The pump efficiency definition from the energy model, defined in equation 6.13, is used to evaluate the pump efficiency from the CFD analyses. The impeller efficiency is however also studied in order to perform a full performance analysis of the pump. The impeller efficiency is defined in two ways, the axial efficiency ($\eta_{imp,axial}$) which is defined like the pump efficiency and the total efficiency ($\eta_{imp,total}$) which is defined like the pump efficiency but, with both the dynamic energy in the swirl and in the axial flow included.

$$\eta_{imp,axial} = \frac{\dot{m}g(H_{static} + H_w)}{\tau\omega} \tag{10.1}$$

$$\eta_{imp,total} = \frac{\dot{m}g(H_{static} + H_{dynamic})}{\tau\omega} \tag{10.2}$$

where H_{static} is the static pressure at point 4. (figure 6.1) relative to atmospheric pressure (the pressure at which the jet leaves the system). H_w is the dynamic pressure in the axial velocity at point 4. and $H_{dynamic}$ is the total dynamic pressure at point 4 including the flow in x and y direction (z being the flow direction) creating a swirl.

The total efficiency is interesting as it states how much of the energy added to the impeller results in an increased dynamic or static pressure, and how much is lost in dissipation. The total efficiency sets a maximum efficiency possible to obtain if the nozzle and guide vane converted all swirl and was without friction loss.

The difference between the axial impeller efficiency and the pump efficiency (η_{pump}) shows how much energy is transformed form swirl to axial energy in the nozzle. This value is named η_{nozzle} as it shows the added efficiency from the nozzle.

$$\eta_{nozzle} = \eta_{pump} - \eta_{imp,axial} \tag{10.3}$$

In section 10.2.2 the results of the steady flow analysis are presented (see section 7 for model details). The steady state analysis is used for evaluating the performance of the pump, compare the three pump cases to study the effects of different pump configurations and the effect of having a hubless pump. The three pump configurations are presented in figure 10.3.

10.2.2 Steady Analysis

The two pump configurations of main interest are Case 1. and 2. Case 3 is used to study the efficiency loss of the impeller related to the missing hub.

In figure 10.4 the performance results of Case 1. and 2. are displayed. By comparing Case 1. and 2. it is obvious that the inclusion of the guide vane results gives a significant efficiency increase, especially when operating at lower volume rates. The low efficiency of Case 2. results in an unsatisfying bollard pull as seen in table 10.2, it is, however, noted that the required bollard pull is reached if the inlet head loss is reduced with about 1.8 meters (see figure 6.3 and table 10.2).

Table 10.2: *The result of the bollard pull condition for the Case 1. and 2. are presented.*

Case		1.	2.	2.(required)
Bollard pull	[kN]	4.17	3.74	4.00
Torque	[Nm]	141	150	146
Head rise ($H_{effective}$)	[Nm]	12.7	11.4	10.9

Note that the shapes of the efficiency curves of pump Case 1. and 2. are different from each other. It appears as if Case 1. operates on the right hand side of a efficiency peak (example of an axial pump efficiency curve is found in [Bulten, 2008]). The efficiency curve of Case 2. appears to be operating on the left hand side, and it even shares similarities with a ducted propeller [Brennen, 1994, Chap. 22].

The impeller and the guide vane blades are influencing each other dynamically and it is therefore likely that a higher efficiency for Case 2. is achievable by blade design alterations (designing it for operation without the guide vane.). It is however unlikely that the average axial efficiency approaches that of Case 1., especially at lower flow rates, as the guide vanes ensure a good efficiency by recovering a lot of the energy in the swirl (compare $\dot{E}_{swirl}$ in table 10.3). The efficiency is split into an impeller contribution and a nozzle contribution (including the guide vane blades for Case 1.) in order to investigate the effect of the guide vane blades. The result is displayed in table 10.3.

It is evident from table 10.3 that the guide vanes have a significant impact on the efficiency and the conversion from static to dynamic pressure in the nozzle. A nozzle without guide vanes results in an overall axial head loss and much of the static pressure is transformed in to dynamic pressure not orientated in the axial direction and the energy stored is lost without any guide vanes to redirect the energy in the axial direction, this is clear when comparing the remaining energy in the swirl (E_{swirl} given in percent of the total energy input) after the nozzle.

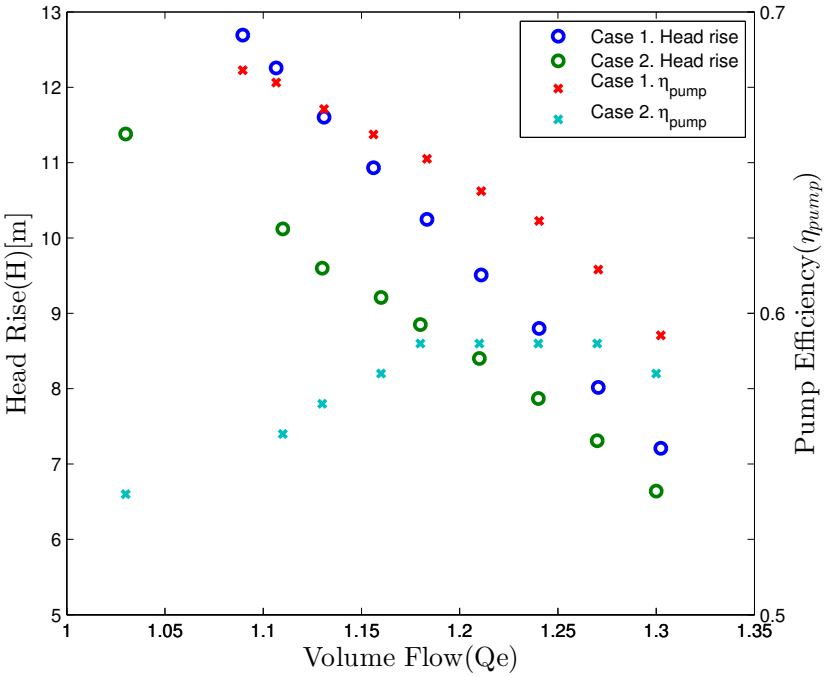

Figure 10.4: Plot of the produced head rise and axial efficiency at given flow rates for the case 1 pump configuration.

It is observed that the guide vanes are decreasing the efficiency of the impeller when they are contributing with the highest amount of energy recovery (η_{nozzle}). This tendency was also observed during the final design phase as adjusting the impeller or the guide vane blades to increase the overall efficiency often resulted in an almost unchanged efficiency. The efficiency of the impeller would drop along with the increase in guide vane efficiency and visa versa. The guide vanes affect the static pressure after the impeller and thereby changes the flow on the pressure side of the blade which causes the change in the impeller efficiency.

The results from Case 1. and 2. are compared to the thrust requirement prediction (see section 2.1) to determine the maximum speed of the boat. In figure 10.5a the produced head rise form Case 1. and 2 are plotted together with the benchmarking head rise from the mathematical model, (see table 6.2). From this figure it is obvious that both Case 1. and 2. would be able to reach speeds around 25 knots.

It is clear that the head rise produced for the speeds between bollard pull and 25 knots is much higher than the required head rise from the benchmarking. These conditions are in reality not in equilibrium and the thrust produced is much higher than that needed to maintain the specific speed, this keeps the vessel accelerating until an equilibrium is reached between the produced thrust and the hull resistance at around 25 knots. The equilibrium occurs just over 25 knots for Case 1 and just under for Case 2 with a head rise close to 8 meters and a produced thrust around 1.5 kN (see figure 2.2).

Table 10.3: The axial pump efficiency divided into the contributions from the impeller and the guide vane. E_{swirl} defines remaining energy in the swirl as a fraction of the total energy added to the system. H is the total head input (energy input) and $H_{effective}$ is the resulting head rise, see equation 6.9

Case 1.										
Flow rate ($\dot{Q}_e$)		1.09	1.11	1.13	1.16	1.18	1.21	1.24	1.27	1.30
H	$[m]$	18.6	18.1	17.4	16.6	15.7	14.8	14.0	13.0	12.2
$H_{effective}$	$[m]$	12.7	12.3	11.6	10.9	10.2	9.5	8.8	8.0	7.2
$\eta_{imp,axial}$	[%]	56	57	59	60	61	62	63	63	63
η_{nozzle}	[%]	12	11	8	6	4	2	0	-2	-4
η_{total}	[%]	**68**	**68**	**67**	**66**	**65**	**64**	**63**	**61**	**59**
E_{swirl}	[%]	2	2	2	2	2	2	2	2	2
Case 2.										
Flow rate ($\dot{Q}_e$)		1.03	1.11	1.13	1.16	1.18	1.21	1.24	1.27	1.30
H	$[m]$	20.9	18.0	16.9	15.9	15.0	14.2	13.3	12.4	11.5
$H_{effective}$	$[m]$	11.4	10.1	9.6	9.2	8.9	8.4	7.9	7.3	6.6
$\eta_{imp,axial}$	[%]	64	64	62	59	59	60	60	61	61
η_{nozzle}	[%]	-10	-8	-5	-1	0	0	-1	-2	-3
η_{total}	[%]	**54**	**56**	**57**	**58**	**59**	**59**	**59**	**59**	**58**
E_{swirl}	[%]	29	26	24	23	21	18	17	15	14

When observing the torque needed to sustain the flow rates displayed in figure 10.5b and table 10.2 it is evident that the final design exceeds the torque limit of the engine in the bollard pull condition for both the Case 1. and 2. configuration. The torque limit is also exceeded at the two following points, but these are irrelevant as the pump can easily operate at a lower torque and still produce thrust enough to cause acceleration of the boat. The high torque in the bollard pull condition is a direct result of the high thrust produced by the pump. However, the torque needed to produce the required 4 kN of thrust is also just above the torque limit (90 Nm/0.68 = 132.4 Nm, see table 6.3 and 10.2) assuming that a similar axial efficiency is reached for the impeller with a slightly lower average loading.

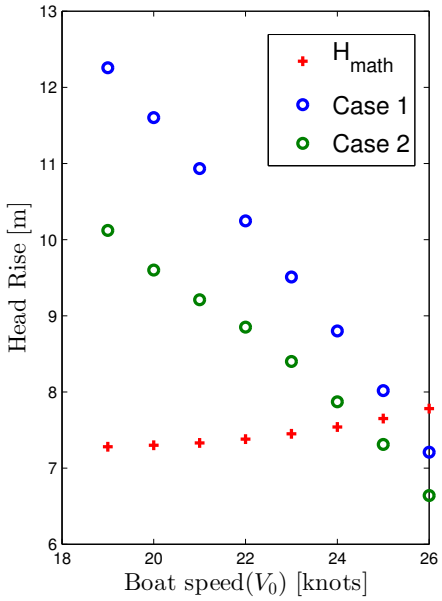

(a) The head rise produced by case 1. and 2. is presented and compared to the minimum requirement from the thrust prediction.

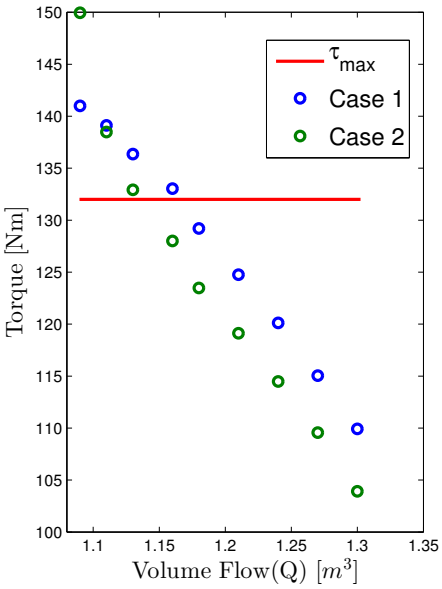

(b) The torque on the impeller in order to create the head rise. The maximum engine torque production is displayed with a line at 132 Nm

Figure 10.5: Figure 10.5a displays head rise produced and required. Figure 10.5b display the torque requirements and the maximum limit

The Performance Impact of The Missing Hub

The consequences of removing the hub are studied by analysing Case 3. and comparing with the Case 1. results. The Case 3. pump configuration uses the same impeller and guide vane blades as Case 1. though with a hub connecting them, see figure 10.6.

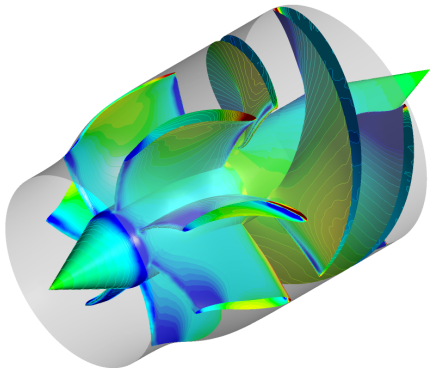

Figure 10.6: Picture of Case 3. pump configuration with the pressure distribution as contours.

The hub is considered frictionless. This is done to remove the open center of the pump without adding skin friction from the hub. The effect of the open center line is thereby studied with the least amount of changing parameters. The hub is forcing the water to flow faster through the pump and thereby altering the design condition for the impeller blades. It is apparent that this pump design is not ideal, a more conventional hub would unmistakably result in a higher efficiency. This configuration does, however, allow for a direct comparison of the impeller performance with and without pressure leaks at the hub. It is evident from figure 10.7a and 10.7b that the efficiency of the impeller, both the total and the axial, is much higher than that of Case 1.

The interesting effect to study is the energy loss related to the pressure leaks from the impeller as this sets an upper limit of the efficiency of the pump, the guide vanes are, therefore, not considered in this study. In addition, the guide vanes are not functioning well as the increased flow velocity emulates a higher flow rate through the pump where the guide vanes result in a decrease in the pump efficiency.

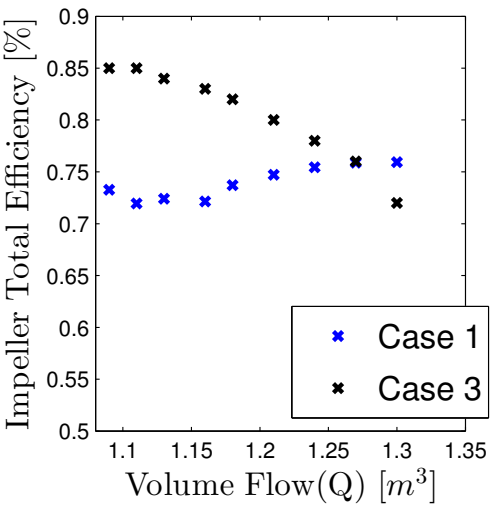

(a) The total impeller efficiency plotted for Case 1. and 3.

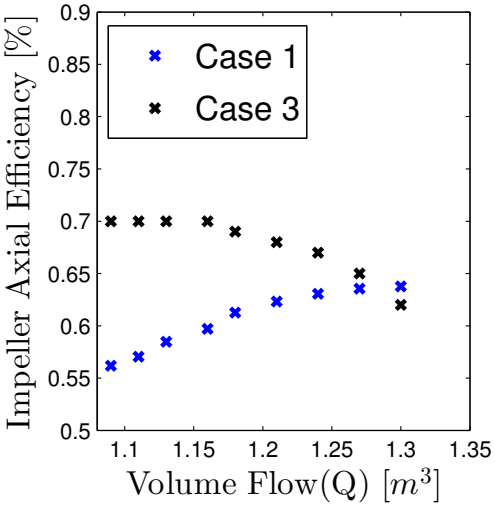

(b) The axial impeller efficiency plotted for Case 1. and 3.

Figure 10.7: Figure 10.7a displays total impeller efficiency of the impeller for Case 1. and 3. Figure 10.7b displays axial impeller efficiency of the impeller for Case 1. and 3.

The significant difference in the impeller efficiency, especial the axial efficiency, is a clear indicator that a larger amount of the energy added to the impeller in Case 1. is transformed into vortices and other swirling flows, thus increasing the static pressure, but also causing a larger dissipation of energy due to internal friction which results in a lower total efficiency and a considerably lower axial efficiency. A traditional axial pump has a maximal total impeller efficiency around 95% (Rolls-Royce experience), which is around 10% higher than that of Case 3. The efficiency difference (from the maximum) is understandable as the impeller is designed for Case 1. and a traditional pump uses a

thickening hub in order to manipulated the flow velocity in order to achieve the highest possible impeller efficiency. The remaining 10% to the efficiency of a regular impeller blade (figure 10.7a) are therefore assumed lost due to design considerations (a cylindrical hub).

It is observed that the trends of the impeller efficiency for Case 1. and Case 3. are in opposition. Case 1. is rising with increased flow rates and Case 3. is dropping. This is caused by the increased flow velocity over the impeller, this emulates a higher flow rate through the system. The emulated flow rate at the bollard pull condition ($Q_e = 1.09$) is equal to that of $Q_e = 1.21$. This pushes the operational points of the impeller to the right hand side of the efficiency peak (decreasing efficiency with increased flow rate) while the impeller in Case 1. is operating on the left hand side (increasing efficiency with increased flow rate).

A minor backflow (fluid flowing opposite of the jet direction) is present at the center of the pump when operating at $Q_e = 1.09$ and $Q_e = 1.11$. The backflow covers 3% to 4% of the pump cross-sectional area, but the flow rate of the backflow is less than one percent of the system's flowrate ($\dot{Q}$). This backflow explains the deviation from the trend in figure 10.7a at the two lowest flow rates. The deviation is explainable as a physical consequence of the backflow, but numerical accuracy is also influenced by the backflow as the second order upwind scheme, used for the computation loses accuracy when evaluating a flow flowing downwind (opposite of the defined flow direction). This decrease in the accuracy is assumed to be small due to the low amount of energy involved in the backflow. The results are still regarded as valid, it is, however, important to be aware of the increased uncertainties of these operational points.

Indication of Cavitation Properties

The steady flow analysis shows that the Case 1. pump configuration is indeed able to produce the needed bollard pull at an efficiency around 68%, the torque is however above the maximum torque produced by the engine. Case 2. is unable to produce the needed head rise for the thrust production in bollard pull. In conclusion the efficiency of the Case 2. is unacceptably low (54%) compared to the 70% expected from a regular axial flow pump with a similar specific speed (see section 6.3.1). The focus of the design phase has been to reach the required thrust production while achieving the best possible cavitation properties. However, this is difficult to establish when the cavitation properties are not good enough and a thrust breakdown (when the efficiency drops 1% because of cavitation) occurs. The cavitation properties are evaluated based on the blade area with pressure below the vapour pressure (2.3 kPa, see table 1.2). It has been clear from an early stage that it is impossible to avoid a significant low pressure area when producing the required bollard pull thrust.

The blade area below vapour pressure, as well as the pressure distribution on a cross sections of the blade, are studied for Case 1. From these studies an indication of the cavitation performance is achieved. Figure 10.9 displays the pump (Case 1. configuration) with pressure contours on the blades (blue being low and red high pressure). The low pressure areas (below vapour pressure) are indicated by a light blue indication, espe-

cially visible in figure 10.9a. It is clear from this visualization that the main cavitation problem occurs when the flow rate is low and the head rise is high. This was expected as the pressure at the pump inlet (Point 3. figure 6.1) is at its lowest in the bollard pull condition which makes the pump vulnerable to cavitation, see figure 10.8.

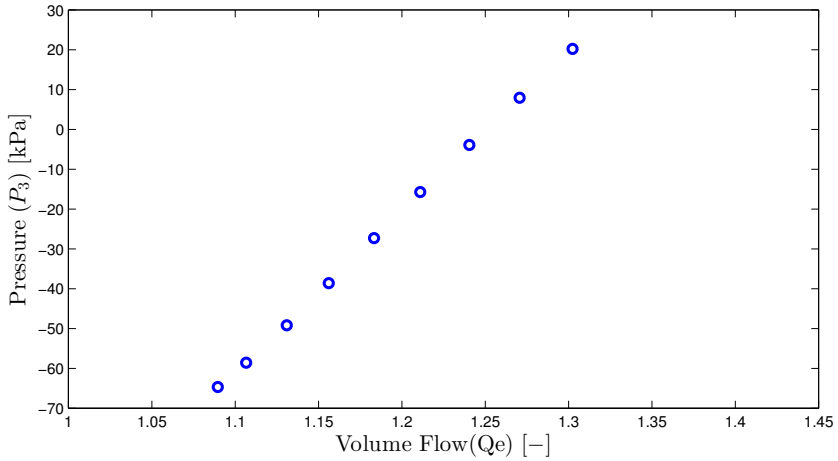

Figure 10.8: Case 1. pressure at the pump inlet (point 3 figure 3.1). The pressure is given relative to atmospheric pressure, here the vapour pressure is −99 kPa.

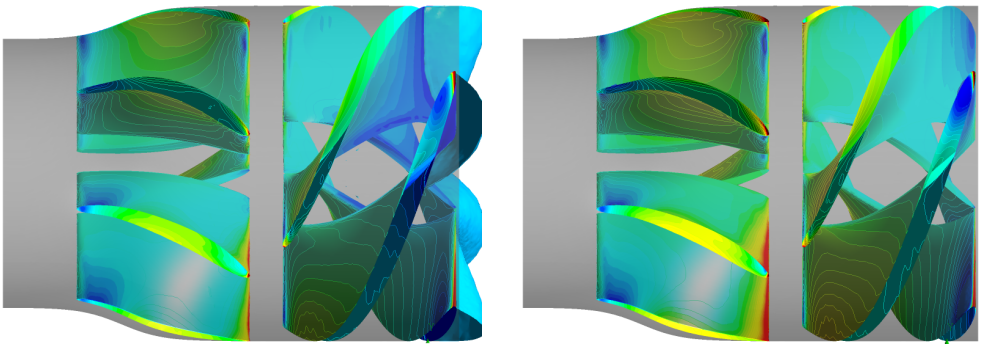

(a) Flow rate at bollard pull ($Q_e = 1.09$).

(b) Flow rate $Q_e = 1.27$, the flow rate equal to a speed of 25 knots.

Figure 10.9: Figure 10.9a and 10.9b displays the results of the CFD evaluation of the pump (Case 1.) operating at the two points of equilibrium.

The streamwise pressure distributions on the impeller blade near the hub at the mid and at the shroud are displayed in figure 10.10. At this point the vapour pressure is indicated with a line. The areas below this line represent the load that the blade in reality cannot deliver as such a low pressure is impossible to reach and the water is spontaneously evaporating causing cavitation. This is especially an issue at the leading edge, even though the impeller blade is mainly loaded on the mid and aft part of the

blade (see figure 9.5), the sudden acceleration of the water at the leading edge results in a very low static pressure near the leading edge.

The pressure difference between the suction and the pressure side defines the blade loading. A load equal to the area below the vapour pressure (figure 10.10) is, in reality, spread out on the rest of the suction side resulting in a larger area of cavitation. The actual area covered by cavitation is difficult to estimate without the use of a multiphase flow model. The area covered by cavitation is dependent on how low the pressure is for a given low pressure area (below 2.3 kN), but also how the pressure distribution of the remaining blade area is, see the bollard pull condition (figure 10.10) at the hub compared to the shroud. It is apparent that the area following the leading edge, at the shroud, can take a higher loading, before cavitation occurs, than the similar area at the hub as the pressure is higher on the suction side near the shroud. Another interesting observation is that the location of the low pressure area switches impeller suction side in the bollard pull condition to the pressure side, near the leading edge at the shroud, in the 25 knot ($Q_e = 1.27$) equilibrium. This is a consequence of the design volume flow of $Q_e = 1.13$, the angle of attack changes with the flow rate. The acceleration on the pressure side is increasing as the flow rate increases and thereby decreasing the static pressure.

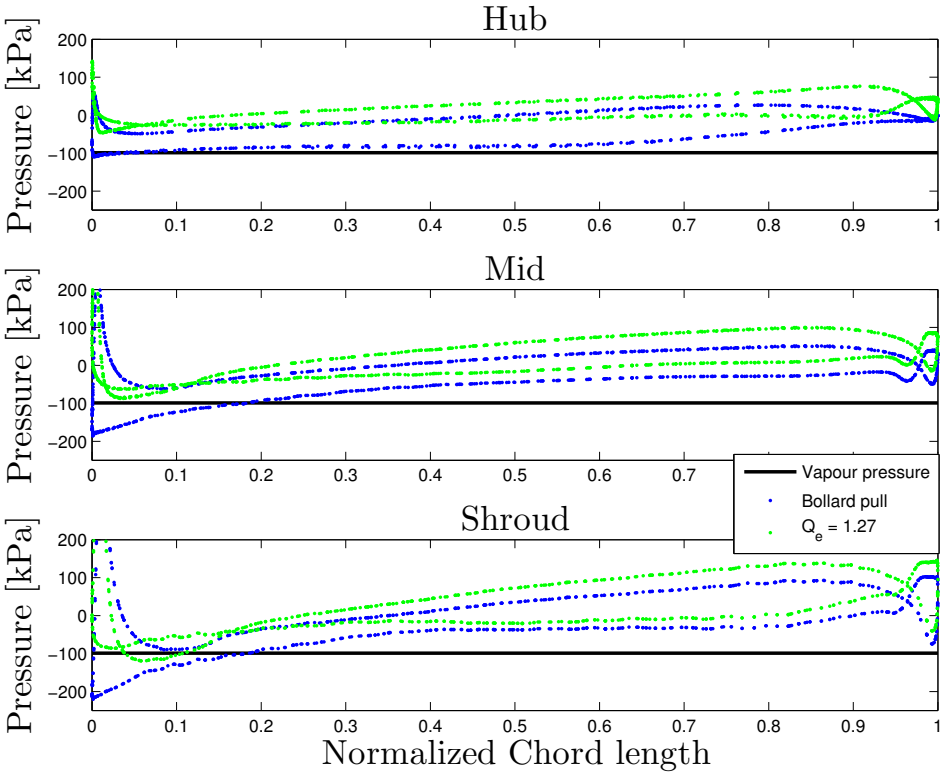

Figure 10.10: The pressure distribution of the Case 1. pump configuration at the two points of head rise equilibrium.

The consequences of cavitation are related to erosion of the pump. However, in this projected a more serious consideration is thrust breakdown. (The minimum operational life of the pump is only 500 hours according to SSRS). Thrust breakdown is often defined to start at the point at which the pump efficiency drops 1% due to cavitation (Rolls-Royce definition, no reference). A complete thrust breakdown (extreme drop in pump efficiency) occurs shortly after due to excessive cavitation in the pump. This definition of 1% efficiency loss is difficult to apply to this study without significant changes in the CFD model, increased number of computations and a more comprehensive analysis are required. The thrust breakdown is estimated using the low pressure area on the impeller as a industry standard, a margin is defined as how much the static pressure at the pump inlet can be lowered before a certain low pressure area is reached. This margin varies from pump to pump and is based on experimental results and CFD computations. Rolls-Royce has pump models in which cavitation breakdown occurs at an approximately low pressure area between 5-10%, it dependence on the pressure distribution of the impeller blades. A estimated cavitation limit of 5% low pressure area is used in this thesis. From this limit a cavitation margin is defined for the two points of equilibrium, see table 10.4. The margin is defined as the pressure difference at the pump inlet that is needed to bring the low pressure area above 5%.

Table 10.4: The table lists the area covered by pressure below vapour pressure. A pressure cavitation margin resulting in 5% cavitating area is displayed as well.

Flow rate (Q_e)		1.09	1.27
Cavitation area	[%]	10.8	1.3
Pressure margin to 5% area	[kPa]	-34.1	34.9

It is obvious from figure 10.9, 10.10 and table 10.4 that a relatively large area of the impeller blade is covered by cavitation in the bollard pull condition. A quite significant negative pressure margin is required to reduce the cavitation area to 5% of the blade. The high cavitation margin of the 25 knots ($Q_e = 1.27$) condition shows a good cavitation performance.

The cavitation performance at the bollard pull condition is crucial as the large head rise required results in a low pressure before the pump inlet (see figure 10.8). The low pressure results in a high cavitation sensitivity of the impeller blade in this operation. The delivered head rise (H), see table 10.3, should be lowered with around 3.5 m ($\frac{34.1\,\text{kPa}}{\rho g} = 3.5\,\text{m}$) in order to reduce the low pressure area to around 5% of the blade area, this is a significant reduction of around 17% of the delivered head rise (table 10.3). This could for example be achieved by reducing the head loss in the duct (increasing the pressure at the pump inlet), improving the efficiency of the pump or increasing the diameter of the impeller, thus reducing the average load in the impeller blade.

The steady flow analysis gives a cost effective insight into the performance of the pump, an unsteady flow analysis is performed for Case 1. to validate the results from the steady flow analysis and to get an improved prediction of the performance of the pump.

The transient performance analysis reveals if the steady flow analysis is a reasonable estimate of the pump performance, it includes the dynamic effect of the pressure in the pump center and then it is possible to establish whether the steady analysis is predicting a local extreme or if it estimates a reasonable average performance.

10.2.3 Transient Analysis

A transient analysis is performed to model the unsteady flow through the Case 1. pump configuration. The pump performance results stem from a time averaging at different flow rates in order to create a $Q - H$ plot (figure 10.11) similar to that of the steady analysis (figure 10.4).

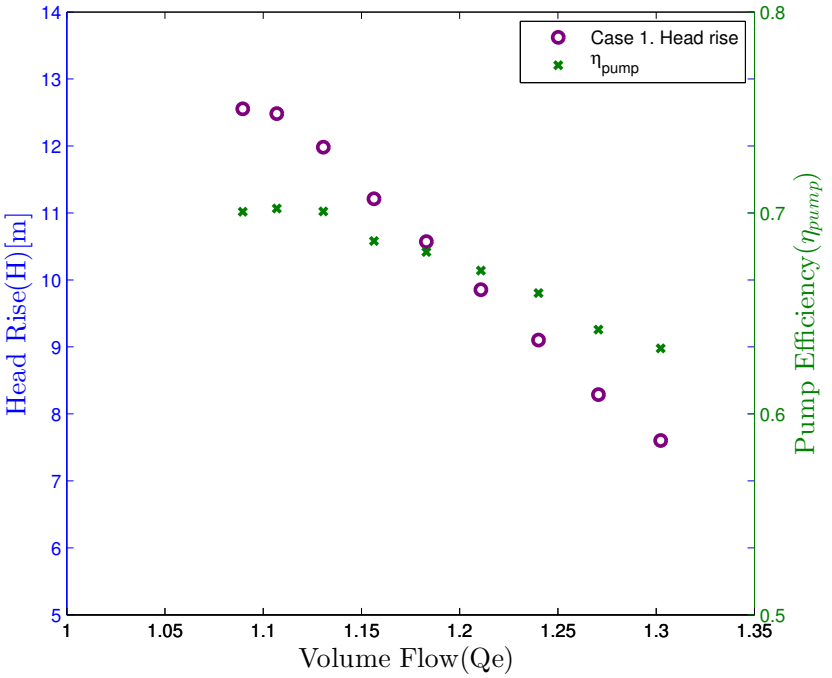

Figure 10.11: Plot of the produced head rise and axial efficiency at given flow rates for the transient analysis of Case 1.

The dynamic behaviour of the pressure in the pump is visualized in figure 10.12 in which four pictures of the pressure distributions on the impeller and guide vane blades, with different relative positions, are displayed. As evident from the figure the fluctuations on the suction side of the impeller blade are small. The flow entering the pump is undisturbed (in the CFD model) and with a constant average velocity, this results in insignificant variations of the pressure distribution on the suction side as this is mostly unaffected by the dynamic behaviour of the pressure behind the impeller. The main fluctuation occurs at the center of the pump and affects the pressure side of the impeller and the guide vane blades.

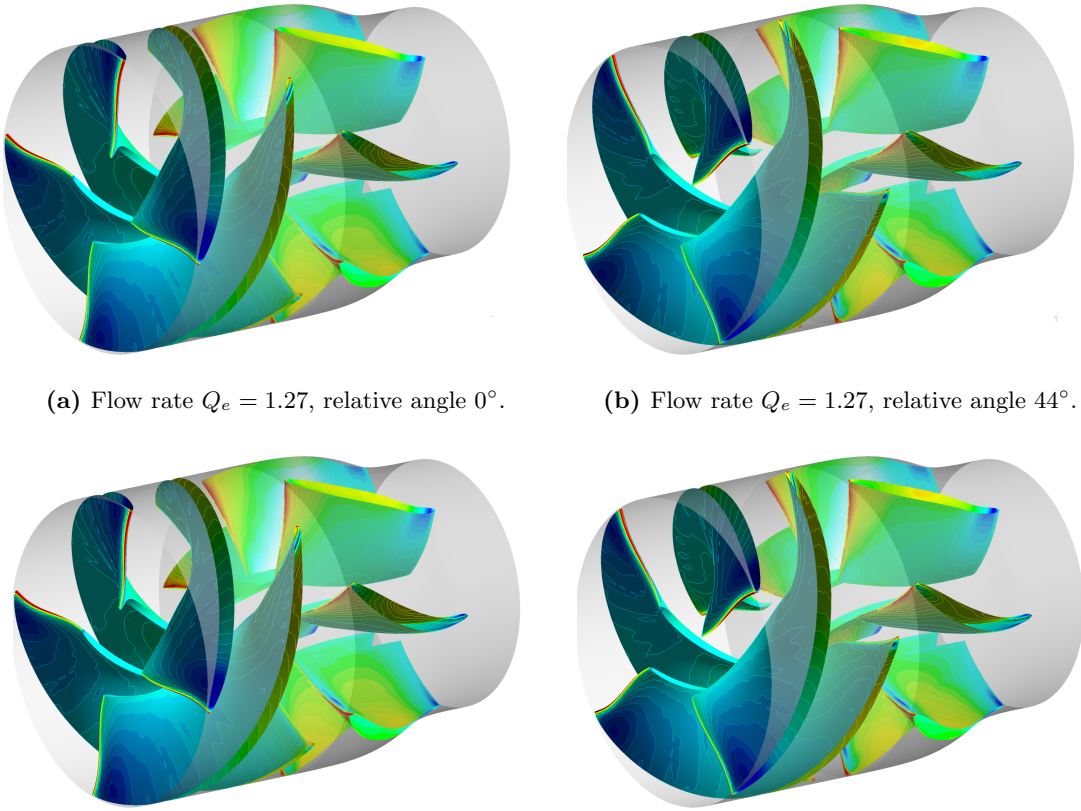

(a) Flow rate $Q_e = 1.27$, relative angle 0°.

(b) Flow rate $Q_e = 1.27$, relative angle 44°.

(c) Flow rate $Q_e = 1.27$, relative angle 88°.

(d) Flow rate $Q_e = 1.27$, relative angle 132°.

Figure 10.12: The fluctuating pressure in the pump is apparent, especially at the guide vane.

The transient analysis yields a higher overall efficiency of the pump, see figure 10.11 and table 10.5. The efficiency is in general around 3 percentage points higher than the results from the steady analysis. The effect of this higher efficiency is visualized in figure 10.13 in which the produced head rise and the torque requirements are plotted against the results of the steady analysis. At this point it is obvious that the transient analysis yields a lower torque and a higher head rise which suggests a higher impeller efficiency. The maximum transit speed determined by the head rise equilibrium displayed in figure 10.13a shows that the top speed remains around 25 knots it is, however, slightly closer to 26 knots compared to the results of the steady flow analysis.

The efficiency distribution between the impeller efficiency and the efficiency gain from the guide vane blades have shifted and the analysis shows a significantly higher added efficiency from the guide vanes (η_{nozzle}) (even at the higher flow rates) and a lower impeller efficiency (see table 10.3 and 10.5). The amount of energy left in the swirl (E_{swirl}) is however unchanged.

Table 10.5: The axial pump efficiency for the transient analysis of Case 1. parted into the contributions form the impeller and the guide vane.

Case 1 - Transient.										
Flow rate ($\dot{Q}_e$)		1.09	1.11	1.13	1.16	1.18	1.21	1.24	1.27	1.3
H	$[m]$	17.9	17.8	17.1	16.3	15.5	14.7	13.8	12.9	12
$H_{effective}$	$[m]$	12.6	12.5	12.0	11.2	10.6	9.9	9.1	8.3	7.6
$\eta_{imp,axial}$	[%]	53	54	55	58	60	61	62	62	63
η_{nozzle}	[%]	18	16	15	11	8	6	4	2	0
η_{Total}	[%]	**70**	**70**	**70**	**69**	**68**	**67**	**66**	**64**	**63**
E_{swirl}	[%]	2	2	2	2	2	2	2	2	2
Difference from steady analysis	[%]	2.1	2.2	3.1	2.6	3.1	3.1	3.0	3.2	4.3

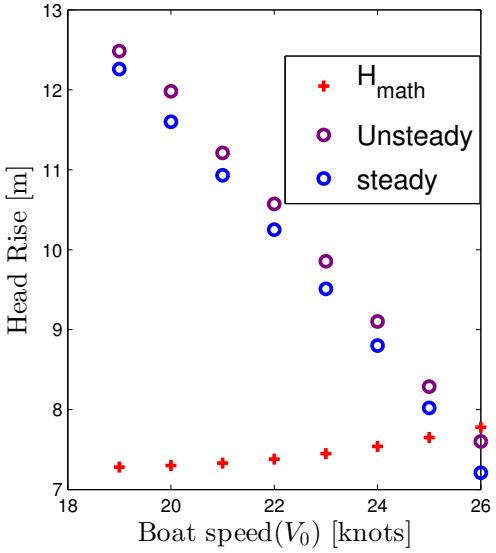

(a) The head rise produced by the Case 1. configuration according to the unsteady and the steady flow analyses compared to the needed head rise from the mathematical model. Please note that the bollard pull condition ($V_0 = 0$) is not included in this figure.

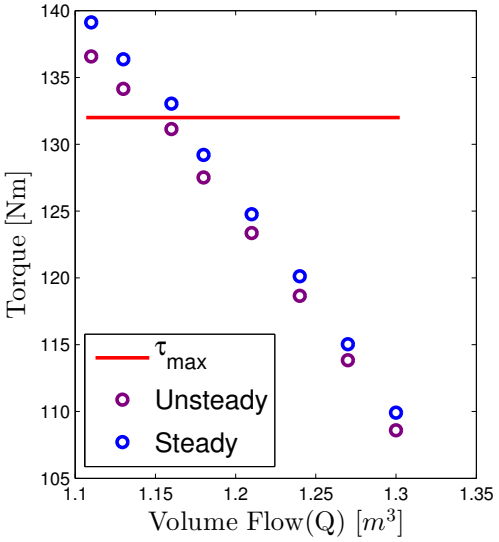

(b) The resulting torque on the impeller blade according to the unsteady and steady analyses. The maximum engine torque production is displayed with a line at 132 Nm.

Figure 10.13: Figure 10.13a displays the head rise production. Figure 10.13b displays torque requirements.

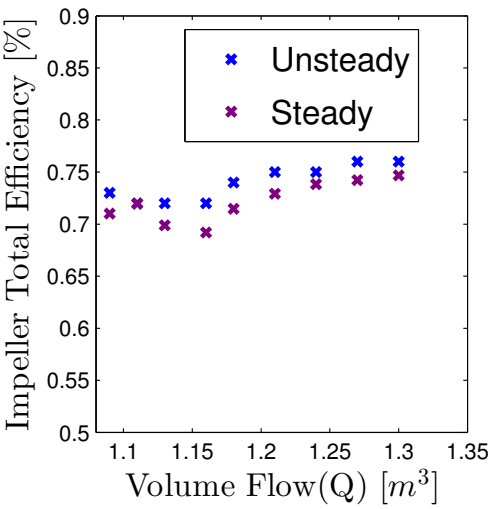

(a) The total impeller efficiency is plotted for Case 1. Note: point 2 ($Q_e = 1.11$) is overlapping for the steady and the unsteady analyses.

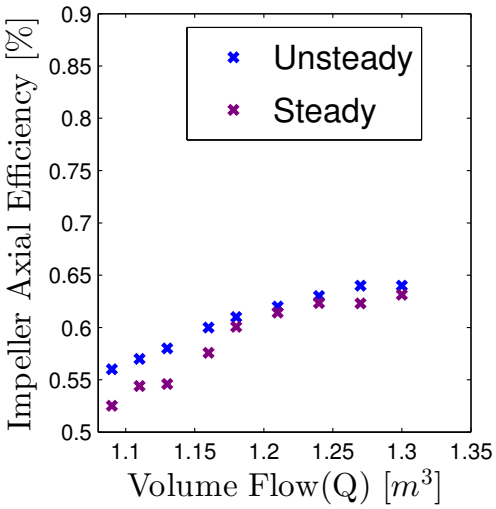

(b) The axial impeller efficiency is plotted Case 1.

Figure 10.14: Figure 10.14a displays the total impeller efficiency. Figure 10.14b displays axial efficiency.

The backflow, observed in the steady flow analysis (section 10.2.2), is also present in the results of the transient analysis. A visualisation of the volume affected by the backflow is displayed in figure 10.15. The backflow occurs at the three lowest flow rates ($Q_e = 1.09$, $Q_e = 1.11$ and $Q_e = 1.13$), which is different than that observed in the steady flow analysis. The effect of the backflow is again related to the physical effects of the backflow and the numerical consequences.

The backflow is believed to affect the energy flow in the center of the pump and enhance the shift of added efficiency from the impeller to the guide vane blades. The effect of this change in the efficiency gain is most severe for the operational points affected by backflow.

It is difficult to determined the exact effect of the backflow on the overall results and efficiency of the pump, the accuracy of the three operational points with the lowest flow rates are, however, regarded as lower than that of the rest. The distinguishing of the impeller and guide vane efficiency of these points are questionable. This argument is supported by the minimal difference between the impeller total efficiency (figure 10.7a) and the pump efficiency (table 10.5) seen at the affected operational points. There are, to the author's knowledge, no published research related directly to this issue and no solution have been implemented. The results of the operational points $Q_e = 1.11$ and $Q_e = 1.13$ are regarded as valid, but this issue emphasizes the importance of an experimental validation and correction of the CFD model. The average backflow velocity is largest in the bollard pull condition (see figure 10.15) and the backflow is believed to be

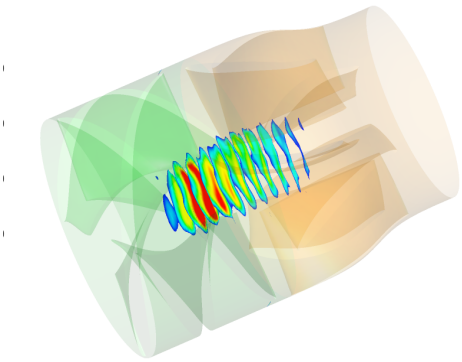

(a) Visualization of the backflow at $Q_e = 1.09$.

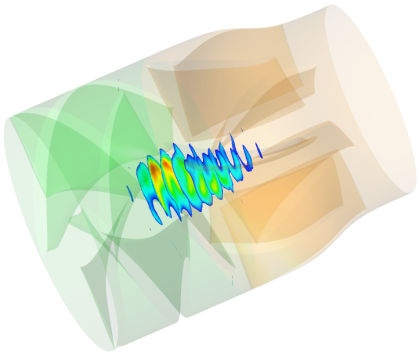

(b) Visualization of the backflow at $Q_e = 1.11$.

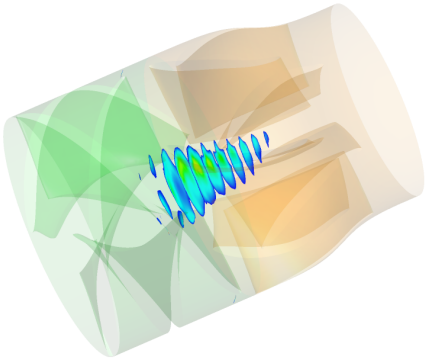

(c) Visualization of the backflow at $Q_e = 1.13$.

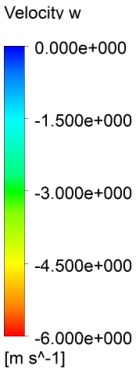

(d) Velocity scale for the backflow plots.

Figure 10.15: The backflow observed in the operational points of low flow rate is visualized.

the main reason why a full convergence is not reached for this condition. This condition is considered invalid and should not be used for the conclusion of the performance (the cavitation analysis is used instead.)

The results from the transient analysis are in general in compliance with the trends from the steady flow analysis, however with a slightly higher pump efficiency. The issue of backflow is more apparent from the transient analysis and the results related to the affected operational points are regarded as valid, but with a higher degree of uncertainty. The efficiency ranges from 63% to 70% in the operational range (equilibrium at $Q_e = 1.3$) this is in accordance with the expected efficiency from section 6.3.1, and it should be possible to produce the design bollard pull of 4 kN within the torque limit (assuming an efficiency around 70% for the bollard pull condition) if the blade loading is lowered while maintaining the same efficiency. The efficiency prediction method (section 6.3.1)

was expected to under predict the maximum efficiency, this is clearly the case as the final concept design is different a high efficiency axial waterjet pump, jet still obtains an efficiency close to the prediction for a regular axial pump. The cavitation properties are still an issue in the bollard pull condition and the risk of thrust breakdown is great as seen in the steady analysis. A transient cavitation analysis is carried out at the two key operational points, the bollard pull and the maximum speed.

10.2.4 Cavitation Analysis

In this section a brief cavitation analysis is presented. The cavitation analysis is based on the transient analysis with an added multiphase flow model. The cavitation analysis is conducted for the two conditions in equilibrium with the energy model, the bollard pull ($Q_e = 1.09$) and the 25 knots condition ($Q_e = 1.27$). The cavitation analysis for the bollard pull condition ($Q_e = 1.09$) converges even though it is based on the non-converged transient analysis, see figure D.5 in appendix D.

The remaining operational points on the pump curve (figure 10.11) are not in equilibrium with the benchmark data (figure 10.13a) which results in an unrealistic low pressure in front of the pump making these condition irrelevant for the cavitation analysis.

The cavitation is displayed at a volume fraction of 0.5. The outer definition of the cavitation (the grey sheet on the figure) is where the volume mixture between water and vapour is 50/50. This is a standard value used by Rolls-Royce. The numerical cavitation produced in the CFD calculation mixes with the water before collapsing in a different way compared to cavitation in experimental set-ups (according to Rolls-Royce experience), the volume fraction of 0.5 is a good approximation of the natural cavitation according to Rolls-Royce experience. The volume fraction and vapour pressure is usually corrected using experimental data to achieve the best predictions, this is however not an option in this thesis.

The results of the cavitation analysis are displayed in figure 10.16 and 10.17. It is quite clear that the cavitation sheet on the suction side of the blade is stable and continuous in the bollard pull condition (figure 10.16). The area covering the blade is large and the efficiency is significantly reduced, see table 10.6. The pump is not able to produce the head rise required for the bollard pull condition, even if a complete thrust breakdown does not occur. Cavitation is however not an issue for the $Q_e = 1.27$ condition as seen in figure 10.17, some minor cavitation occurs and the efficiency is only slightly reduced from 64% to 63% (table 10.6) and the top speed of 25 knots is still reachable.

Table 10.6: *Performance result of the bollard pull condition from the cavitation analysis.*

Flow rate Q_e	1.09	1.27	
Head rise	11.5	8.3	$[m]$
Efficiency	64	63	[%]
Torque	136	116	$[Nm]$

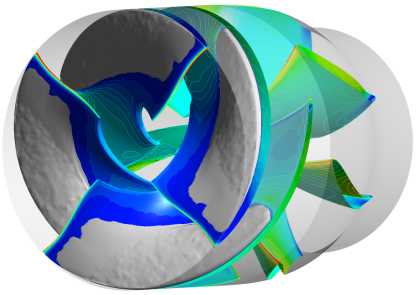

(a) Flow rate $Q_e = 1.27$, relative angle 0°.

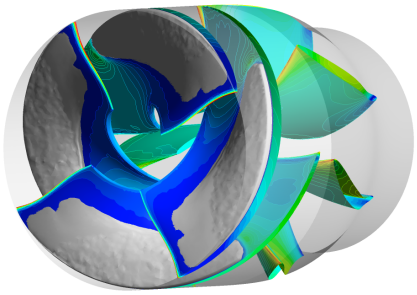

(b) Flow rate $Q_e = 1.27$, relative angle 22°.

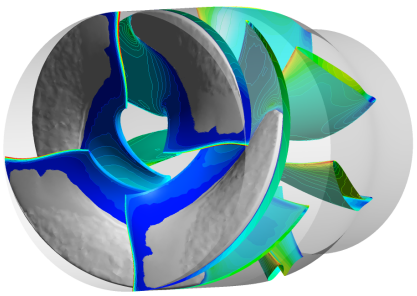

(c) Flow rate $Q_e = 1.27$, relative angle 44°.

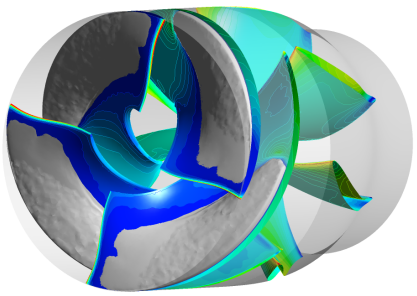

(d) Flow rate $Q_e = 1.27$, relative angle 66°.

Figure 10.16: The fluctuating pressure in the pump is visual, especially at the guide vane.

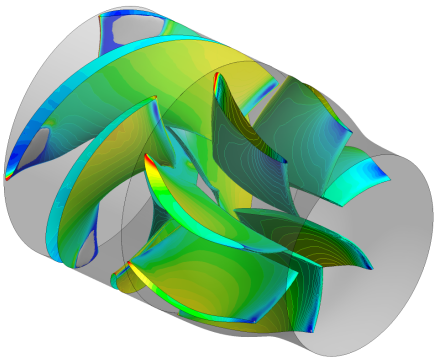

(a) Flow rate $Q_e = 1.27$, relative angle 0°.

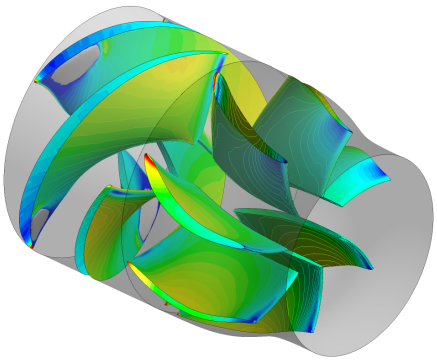

(b) Flow rate $Q_e = 1.27$, relative angle 44°.

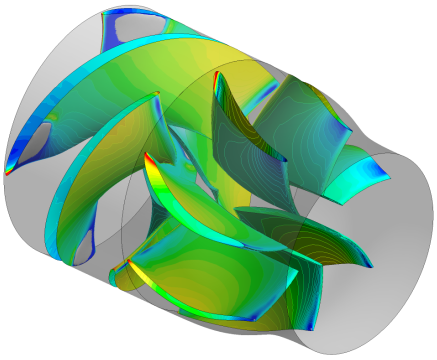

(c) Flow rate $Q_e = 1.27$, relative angle 88°.

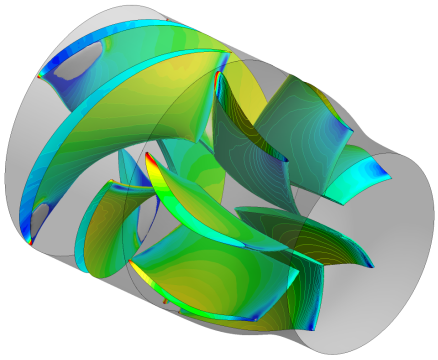

(d) Flow rate $Q_e = 1.27$, relative angle 133°.

Figure 10.17: The fluctuating pressure in the pump is visual, especially at the guide vane.

10.3 Discussion

The results show that it is possible to construct a functioning rim driven hubless waterjet pump, however, it is significant less efficient than a regular waterjet system.

The comparison between the Case 1. and Case 2. pump configurations show that both pumps are able to produce speeds above the minimum design speed of 20 knots, a speed around 25 knots is reachable for the Case 1. pump configuration. The Case 2. pump configuration is, however, unable to produce the required bollard pull thrust, even without considering the cavitation performance. The configuration is simply too inefficient at low flow rates. The ability to handle rope in pump would be good for the Case 2. configuration, but the low efficiency yields the pump unable to meet the requirements of the waterjet system.

The comparison of Case 1. and Case 3. pump configurations revealed as expected a significant energy loss due to the missing hub (around 10%). A spin-off effect of this is the loss of the ability to manipulate the flow velocity over the pump, and thereby be able to design a high efficiency impeller. These two effects result in an impeller with roughly 20% lower efficiency compared to regular axial waterjet impellers. Another way to increase the velocity of the flow over the impeller could be to start the nozzle already at the impeller stage, this has not been investigated, but it is believed to have little effect if the current pump specifications are to be used, as the nozzle inlet/outlet ratio is high (80%).

The transient analysis shows that the pump is delivering the needed head rise for the propulsion. The accuracy of the transient analysis is reduced for the lower flow rates as a backflow is experienced. The backflow results in a highly dynamic flow, and it is difficult to reach convergence of the calculation and the bollard pull condition never fully converged. However, the results are in compliance with the results of the steady analysis and the trends of the results at the higher flow rate calculations.

The cavitation analysis showed, as expected, a significant amount of cavitation in the bollard pull condition. The efficiency of the pump is reduced greatly by this, and it is likely that cavitation breakdown would occur. The top speed condition only experiences a minor amount of cavitation which does not influences the reachable top speed.

It is evident from the entire analysis that the impeller blades are loaded heavily in order to produce the required head rise. The pump is too small to produce the required head rise (ignoring cavitation) for the bollard pull condition as the impeller blades must be loaded to such an extend that, the efficiency is reduced significantly when cavitation is considered.

10.4 Rope in Pump Discussion

The rope in pump condition is briefly discussed using a simple flow analysis. The ability to avoid downtime due to rope in pump is of great importance to the pump design. It is, however, very difficult to analyse without an experimental set-up.

There is a large number of different types of ropes that could be found in the water near a ship in distress. The main type of rope considered in this analysis is a floating polyester line used on life rafts. A floating line should be much easier to handle in the pump compared to for example a steel wire, but the probability of encountering a floating line is equally larger (because it does not sink). However, if the floating line is attached to something it cannot pass through the pump thus making the encounter that much more critical.

The discussion is purely hypothetical as there are no tools available to produce a deeper analysis. The discussion is based on the hypothesis that the pump functions as a centrifuge, and thereby forces the floating line (with a density lower than water) into the center of the pump as the heavier water is forced to the sides of the pump. Floating lines in the pump are easily handled if the hypothesis is valid. The rope is pushed into the center by the centrifugal force. See figure 10.18 for a figure of the pump including streamlines. On this figure the swirl in the center line is clear.

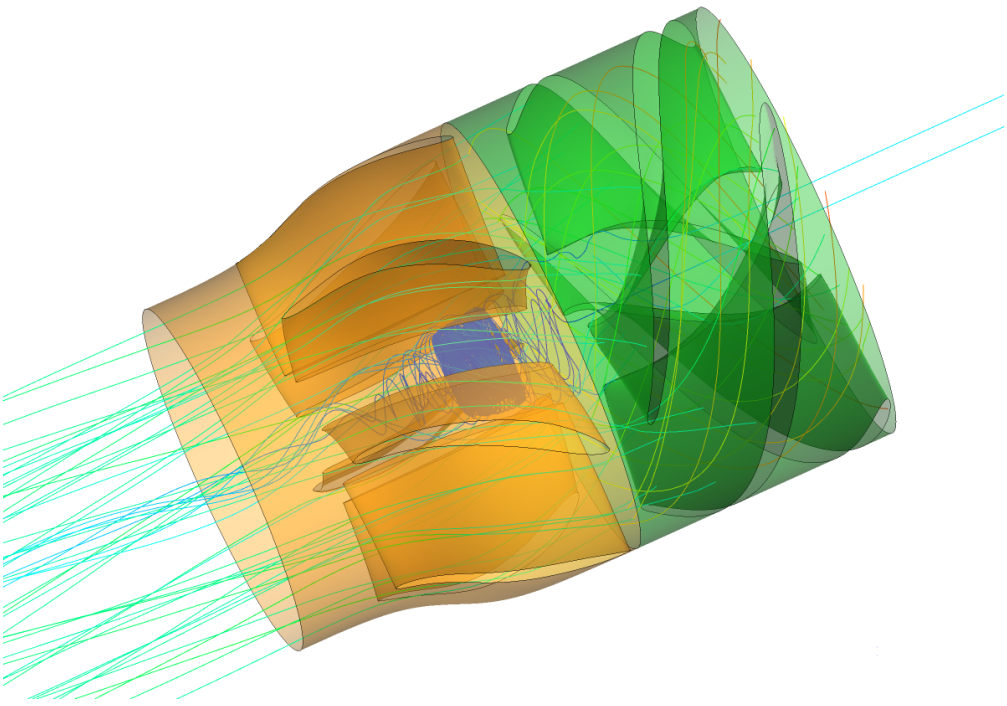

Figure 10.18: Figure of the flow through the pump at the bollard pull condition with steamlines visualizing the flow through the pump. Note the swirl in the centerline. The figure is based on the transient cavitation analysis.

The most likely situation in which to encounter ropes attached to something would be in bollard pull when towing for example a number of life rafts. At this condition the flow in the pump have the highest fluctuation and the probability of the rope getting out of the center and into the impeller and guide vane blades are at the highest. It is therefore interesting to investigate how the rope will react when caught in the blades.

To analyse the reaction of the rope in such a situation one has to imagine the rope placed along one impeller blade and in between two guide vanes. The rope would slide into the center of the pump, when the rope is forced pass the a guide vane, if the guide vane blades are leaned slightly away from the rotational direction at the hub. This is already the case with the stacking used it is, however, a minimal angle, as it is impossible to enforce a leaning angle for the entire blade in TD1. This is, however, very difficult to visualize using the tools available.

Even if the rope is entangled into the impeller and guide vane blades the removal would probably be much simpler than compared to a regular shaft driven pump as there is nothing the rope can get stuck on or spin up on.

This page is intentionally left blank.

11 Conclusion

In this thesis a rim driven hubless waterjet pump concept has been developed and a performance analysis has been conducted. Three pump configurations has been analysed, using a simple steady state CFD model, and compared in order to investigate the option to operate without guide vanes and the efficiency loss related to the removal of the hub. It has been concluded that a pump without guide vanes is unable to produce the required head rise of the specific application, and that a pump without guide vanes, in general, is unable to produce an acceptable pump efficiency. A study of the effects of removing the hub showed that the efficiency of the impeller is reduced with about 10%, compared to an impeller with a cylindrical hub, due to energy losses in the center line. The impeller efficiency is further reduced, compared to a regular axial waterjet impeller, due to the inability to manipulate the flow velocity over the impeller blade. The reduced impeller efficiency results in a reduced pump efficiency as the impeller efficiency defines the maximum pump efficiency.

The final concept design, with guide vanes, has been analysed using a transient CFD analysis in order to improve the performance prediction by including the dynamic effects of the rotating impeller. The performance analysis has shown that a top speed around 25 knots is reachable, and that the required bollard pull of 4 kN is achievable if cavitation is ignored. However, the required bollard pull thrust is not achievable, if cavitation is considered, as evident from the cavitation analysis. The pump experiences a large amount of cavitation resulting in a low efficiency and possibly a cavitation induced thrust breakdown. The cavitation properties of the pump must be improved, either by pump or duct design alterations. A number of solutions to this problem are suggested in the future work section (section 11.1).

The transient analysis has shown that the efficiency of the pump ranges from 70% at low flow rates to 63% at the top speed. This is consistent with the predicted maximum for an axial flow pump in section 6.3.1.

The accuracy of the transient performance prediction is reduced by a backflow in the pump center at the lowest flow rates. A deviation from the trend of the efficiency curve (figure 10.11) is observed at these points, it is concluded that both the physical and numerical consequences of the backflow has an effect on the efficiency. The effects are however undistinguishable with the methods used. It is therefore evident that an experimental validation of the pump performance is required.

It is concluded that the handling of rope in pump is significantly improved compared with a regular waterjet pump. A simple flow analysis has shown that it is possible to

avoid entanglement as the centrifugal force, due to the rotation of the water, forces the floating line into the centerline of the pump. However, an experimental conformation is required as the analysis is based purely on flow observations.

The objective of the thesis is met as a functioning concept design of a rim driven waterjet pump has been developed. The bollard pull requirement is, however, not met with the current design. It is concluded that the required bollard pull is achievable with a rim driven pump of similar design, if the cavitation properties of the entire waterjet system are improved. The final concept design of the thesis is recommended as a starting point for the final development of the full waterjet system including the duct.

11.1 Future Work

The concept design needs refinement to reach acceptable cavitation properties. There are several methods to improve the cavitation properties, that should be investigated further.

- Re-evaluate the bollard pull requirement. If a lower thrust is acceptable improved cavitation properties are reachable by lowering the average blade loading.

- Detailed modelling of the inlet duct to evaluate the actual head loss. It is possible to improve the cavitation properties by designing a duct with a significantly lower inlet loss factor (ξ) at zero speed, this would result in a decreased blade loading at the same produced bollard pull thrust.

- Increase the impeller diameter. The cavitation properties are improved if the diameter of the impeller is increased as there is a greater area to distribute the loading on. However, this will require a redesign of the engine entirely.

- Increase the rotational speed of the impeller. The maximum speed of the engine is 4000 rpm, and the present design is running at 3500 rpm. The change would improve the cavitation properties as the average blade loading is lowered, it is however not believed that this alone will be sufficient to reach acceptable cavitation properties as it is only a 14% increase in the rpm. The increased rotational speed will increase the complexity of the impeller blade's geometry, thereby reduce the rope in pump capabilities of the pump.

- Increase the nozzle outlet diameter. This has already been done to a certain extend as the nozzle inlet/outlet ratio has been increased from 60% to 80 %. The method reduces the efficiency of the pump as the flow rate is increased and thereby the frictional losses in the pump. The required head rise is decreased with the increased flow rate, this results in a higher pressure in front of the pump which improves the cavitation properties. However, it is necessary to ensure that the inlet duct does not experience cavitation due to the increased flow rate.

It is evident from the results that the performance of the pump is pushed over the limit and the best solution is believed to be an increased pump diameter. It is however of great importance to investigate if the inlet head loss factor is correct for the final duct design. The crucial operation of the pump is the bollard pull condition as the speed requirement of 20 knots is easily obtained if a 4 kN thrust is achieved in the bollard pull condition.

This page is intentionally left blank.

Bibliography

R. Aartojärvi and M. Heder. Waterjet pump development for high performance and higher power density. *Waterjet Propulsion*, 5, 2008.

John Allison. Marine waterjet propulsion. *Transactions - Society of Naval Architects and Marine Engineers*, 101:275–335, 1993. ISSN 00811661.

Ansys. Fluent documentation. Ansys, 2013.

D. Bonaiuti, M. Zangeneh, R. Aartojärvi, and J. Eriksson. Parametric design of a waterjet pump by means of inverse design, cfd calculations and experimental analyses. *Transactions - American Society of Mechanical Engineers Journal of Fluid Engineering*, 132(3), 2010. ISSN 0098-2202.

Christopher E. Brennen. *Hydrodynamics of Pumps*. Oxford University Press, 1994. ISBN 0-933283-07-5.

N.W.H. Bulten. Cfd simulations of the flow through a waterjet installation. *Waterjet Propulsion*, 4, 2004.

N.W.H. Bulten. Fully transient cfd analyses of waterjet pumps. *Marine Technology*, 44, 2007.

N.W.H. Bulten. A breakthrough in waterjet propulsion systems. *DIMDEX*, 2008.

J. S. Carlton. Marine propellers and propulsion. *Marine Propellers and Propulsion*, pages 357–365, 2007.

ITTC. The specialist committee on validation of waterjet test procedures. *24th ITTC*, 2005.

ITTC. Ittc recommended procedures: Fresh water and seawater properties. *26th ITTC*, 2011.

Florian R. Menter. Zonal two equation kappa-omega turbulence models for aerodynamic flows. *CASI*, 1993.

Rolls-Royce. Internal duct pressure loss investigation. Internal document, 2010.

D. Savitsky. Hydrodynamic design of planing hulls. *Marine Technology*, 1(1):71–95, 1964. ISSN 00253316.

TD1. Turbodesign1: Application manual. Advanced Design Technology, 2012a.

TD1. Turbodesign1: User manual. Advanced Design Technology, 2012b.

Michael J. Thad, Schroeder D. Seth, and Becnel J. Alan. Design of the onr axwj-2 axial flow water jet pump. *Hydromechanics Department Report*, 2008.

author unknown. http://www.nauticexpo.com/prod/brunvoll/azimuth-thrusters-ship-rim-drive-22122-435833.html, 2014.

H. K. Versteeg and W. Malalasekera. *An introduction to computational fluid dynamics : The fintie volume method*. Pearson Education Limited, 2007. ISBN 9780131274983.

F.M. White. *Viscous Fluid Flow*. McGraw-Hill Book Company, 1974. ISBN 0070697108, 9780070697102.

Qiongfang Yang, Yongsheng Wang, Zhihong Zhang, and Mingmin Zhang. Research on the optimum blades number of mixed flow pump based on cfd. *Waterjet Propulsion*, 2008.

M. Zangeneh. A compressible 3-dimensional design method for radial and mixed flow turbomachinery blades. *INTERNATIONAL JOURNAL FOR NUMERICAL METHODS IN FLUIDS*, 13(5):599–624, 1991. ISSN 02712091, 10970363.

A Savitsky's Thrust Prediction Method

```
%%%%%%%%%%%%%%%%%%%%%%%%%%%%%%%%%%%%%%%%%%%%%%%%%%%%%%%%%%%%%%%%%%%%%%%%%%%
% Savitsky's prediction method
% By Thor Peter Andersen - 2014
% version 1.
%%%%%%%%%%%%%%%%%%%%%%%%%%%%%%%%%%%%%%%%%%%%%%%%%%%%%%%%%%%%%%%%%%%%%%%%%%%
% By Thor Andersen
% Date 2014-02-14
clc
% close all
clear all
%%%%%%%%%%%%%%%%%%%%%%%%%%%%%%%%%%%%%%%%%%%%%%%%%%%%%%%%%%%%%%%%%%%%%%%%%%%
%% Inputs                                                                %%
%%%%%%%%%%%%%%%%%%%%%%%%%%%%%%%%%%%%%%%%%%%%%%%%%%%%%%%%%%%%%%%%%%%%%%%%%%%
    m = 800; %[kg] single person on board
% b = 1.43; % [m]
    b = 0.96938;
    LCG = 1.675; % [m]
    VCG = 0.4; %[m]
beta = 15; %[deg]
Vk = 30; %[knots]
Vk_min = 7;
Vk_array = linspace(Vk,Vk_min,Vk-(Vk_min-1));
V_array = Vk_array*0.514444; %[m/s]
    epsilon = 0; % Inclination of thrust.
    f = VCG -0.150; %Distance between VCG and Trust output.
%Gravitational constant
g = 9.82; %[m/s^2]
%Density of water at 20 degress
rho = 1026.0210; % Density of water at 20[C] see ITTC -
mu = 0.001220;
nu = mu/rho;
%%%%%%%%%%%%%%%%%%%%%%%%%%%%%%%%%%%%%%%%%%%%%%%%%%%%%%%%%%%%%%%%%%%%%%%%%%%
%% Savitsky's 30 steps                                                   %%
%%%%%%%%%%%%%%%%%%%%%%%%%%%%%%%%%%%%%%%%%%%%%%%%%%%%%%%%%%%%%%%%%%%%%%%%%%%
%Initial trim angle.

for j = 1:length(V_array)
```

```
tic
V = V_array(j);
disp('————————————————————')
disp(' Velocity in knots')
disp(Vk_array(j))
tau = 10; %[degrees]
Mtot = —10000;
go = 1;
it = 1;
while go == 1;
    tau = tau+0.001;
    %Planing Coefficients
    Cv = V/sqrt(g*b);
    Clb = (m*g)/(1/2 * rho * V^2 * b^2);

    %Step 1 & 2:
    Cl0 = 0.01; %initial guess
    error = 1;

    while abs(error) >Clb/100%less than 1% error
        Clb_it = Cl0 — 0.0065 * beta * Cl0^0.6;
        error = Clb—Clb_it;
        Cl0 = Cl0 + 0.00001;
    end

    %step 4

    error2 = 1;
    lambda = 0;
    while abs(error2) >0.001
        Cl0_it = tau^1.1 *(0.0120 *lambda^(1/2) +...
            0.0055*lambda^(5/2)/Cv^2);
        error2 =  Cl0—Cl0_it;
        lambda = lambda +0.001;
    end

    %Step 5: Average planing surface velocity.
    Vm = V * sqrt(1 —(0.0120 * lambda^(1/2) * tau^1.1 — ...
        0.0065*beta*(0.00120 * lambda^(1/2) * tau^1.1)^0.6)...
        /(lambda*cosd(tau)));

    % Step 6: Reynolds number
    Re = Vm*lambda*b/nu;

    % Step 7:
    Cf = 0.075/(log10(Re)—2)^2;

    % Step 8:
    dCf = 0.0004;

    % Step 9 &10
    Df = rho*Vm^2*lambda*b^2*(Cf+dCf)/(2*cosd(beta));
```

```
        % Step 11-16
        D = m*g*tand(tau)+Df/cosd(tau);

        % Step 17 Cp figure 17
        Cp = 0.75-1/(5.21*Cv^2/lambda^2 +2.39);

        % Step 18 +19

        c =LCG - Cp*lambda*b;

        %step 20 +21
        a = VCG -b/4*tand(beta);

        % Step 22-30

        Mtot = m*g*( c/cosd(tau) *(1-sind(tau)*sind(tau+epsilon))...
            -f*sind(tau))+Df*(a-f);

        if Mtot >10
%             disp('Too high tau, tau reduced by 0.05 degree')
            tau = tau - 0.05;

        end

        %     figure(1)
        %     hold on
        %     plot(tau,Mtot,'xr')

        if Mtot >-5 && Mtot<10
            go =0;
            disp('Number of iterations')
            disp(it)
            disp('Cl0')
            disp(Cl0)
            disp('--------------------')
        end
        it = it+1;
    end
    %Negative value found

    % Positive value and linear interpolation!
    % tau_0 = interp1q(Mtot_array',tau_array',0);
    %Figure 18
    value(j) = sqrt(Clb/2);
    D_plot(j) = D;
    Mtot_plot(j) = Mtot;
    tau_plot(j) = tau;
    Lk(j) = lambda*b+b*tand(beta)/(2*pi*tan(tau));
    d(j) = Lk(j)*sind(tau);
    CLB(j) = Clb;
    CL0(j) =Cl0;
    Lambda_plot(j) = lambda;
    Cf_plot(j) = Cf;
```

```
    toc
end

figure()
plot(Vk_array,D_plot*10^(-3),'x')
title('Thrust Curve - script 2,2')
xlabel('Vessel Speed [knots]')
ylabel('Resistance,[kN]')

figure()
plot(Vk_array,tau_plot,'-x')
title('Planing Angle at Speed - script 2,2')
xlabel('Vessel Speed [knots]')
ylabel('planing angle')

% %Adding bullard push condition
Vk_array(end+1) = 0;
V_array(end+1) =0;
D_plot(end+1) = 4000;
tau_plot(end+1) =0;
Mtot_plot(end+1) = 0;
%%%%%%%%%%%%%%%%%%%%%%%%%%%%%%%%%%%%%%%%%%%%%%%%%%%%%%%%%%%%%%%%%%%%%%%%%%%%%%%
%                          Production of output file
%%%%%%%%%%%%%%%%%%%%%%%%%%%%%%%%%%%%%%%%%%%%%%%%%%%%%%%%%%%%%%%%%%%%%%%%%%%%%%%
disp('Printing to file')
fileName = strcat('RC2.txt');  % NAME OF txt file is defined here.
fileID = fopen(fileName,'w');

for i = 1: length(D_plot)
    fprintf(fileID,' %3.2f %3.2f %3.2f %3.2f %3.2f \n'...
        ,Vk_array(i),V_array(i),D_plot(i),tau_plot(i),Mtot_plot(i));
end


fclose(fileID);
```

B Mathematical Model Matlab Script

```
%%%%%%%%%%%%%%%%%%%%%%%%%%%%%%%%%%%%%%%%%%%%%%%%%%%%%%%%%%%%%%%%%%%%%%%%%%%%%%%
% Mathematical model of waterjet propulsion system
% By Thor Peter Andersen – 2014
% version 3.
%%%%%%%%%%%%%%%%%%%%%%%%%%%%%%%%%%%%%%%%%%%%%%%%%%%%%%%%%%%%%%%%%%%%%%%%%%%%%%%
 clear all
clc
 close all
 %definition of opeation points modelled in CFD
tab_index = ( [25 12 11 10 9 8 7 6 5 ]);
sea_margin = 1.2; % 20% seamargin
load RC2.txt % Input from Resistance_curve_2.m
RC = RC2;
%The input from the resistance curve are now devided into arrays.
Vk = RC(:,1);
U = RC(:,2);
T = RC(:,3) ; % resistance or Thrust needed.
T(1:end-1) = T(1:end-1) *sea_margin;
T(end) = 4180;
tau = RC(:,4);
Mtot = RC(:,5);

%%%%%%%%%%%%%%%%%%%%%%%%%%%%%%%%%%%%%%%%%%%%%%%%%%%%%%%%%%%%%%%%%%%%%%%%%%%%%%%
%Constants & Dimensions
%%%%%%%%%%%%%%%%%%%%%%%%%%%%%%%%%%%%%%%%%%%%%%%%%%%%%%%%%%%%%%%%%%%%%%%%%%%%%%%
d_imp = 0.195; % Maximum impeller diamter – general pipe diameter.
n = 9; %Suggested in ITTC_validation of waterjet test procedures page 488
                x = 2.5; %Length til the ramp start. point 1. ITTC
                r_st = 1.35*d_imp/2; % Streamtube radius.
                L = 1.5; %[m] Length of duct.
                f_nozzle = 0.8;%ratio between nozzle outlet and inlet
                %diameter. (%changed to 0.8 on the 21st of March)
d_nz = d_imp*f_nozzle; % Nozzle outlet diameter
                z =0.15; % Elevation of the waterjet nozzle
      %The draught of the craft. (Assumed to be close to zero when planing.
                draft =fliplr([linspace(0.5,0,12) linspace(0,0,13)])';
```

```
                e = 0.046*10^(-3); % roughness of commercial steel.
g = 9.82; %[m/s^2]

%Fresh water for simulations%
                rho = 998;
                mu = 0.001002;   %[20C]
nu = mu/rho;
                P_atm = 103*10^3; %[pa]
                rpm = 3500;

%%%%%%%%%%%%%%%%%%%%%%%%%%%%%%%%%%%%%%%%%%%%%%%%%%%%%%%%%%%%%%%%%%%%%%%%%%%%%%%
%Cross sectional areas
%%%%%%%%%%%%%%%%%%%%%%%%%%%%%%%%%%%%%%%%%%%%%%%%%%%%%%%%%%%%%%%%%%%%%%%%%%%%%%%
A_pipe = d_imp^2/4 * pi; % Cross sectional area of pipe.
A_nz = d_nz^2/4 * pi; % Cross sectional areba of nozzle outlet


%%%%%%%%%%%%%%%%%%%%%%%%%%%%%%%%%%%%%%%%%%%%%%%%%%%%%%%%%%%%%%%%%%%%%%%%%%%%%%%
% Point 1. according to ITTC - Velocity in stream tube
%%%%%%%%%%%%%%%%%%%%%%%%%%%%%%%%%%%%%%%%%%%%%%%%%%%%%%%%%%%%%%%%%%%%%%%%%%%%%%%
P_1 = P_atm + rho*g*draft;
Rex =  x * U ./ nu;    %Reynolds number at point 1.
delta = 0.16./Rex.^(1/n); % Equation 6-70 page 434 Frank M. White
% Area of boundary layer estimated as a ritangular box
A_delta = r_st.*delta;
m_dot_stdelta = ones(size(T));

for i = 1:length(U)
    %Equation 9.24 page 405: Robert W. Fox or eq.6-69 Frank M. White
    u =@(y) (y/delta(i)).^(1./n).*U(i);
    % Flow through the boundary layer part of the stream tube
    m_dot_stdelta(i) = integral(u,0,delta(i)).*rho.*r_st;
end


%%%%%%%%%%%%%%%%%%%%%%%%%%%%%%%%%%%%%%%%%%%%%%%%%%%%%%%%%%%%%%%%%%%%%%%%%%%%%%%
% Point 6. Vena Contraction of jet after nozzle exit.
%%%%%%%%%%%%%%%%%%%%%%%%%%%%%%%%%%%%%%%%%%%%%%%%%%%%%%%%%%%%%%%%%%%%%%%%%%%%%%%
 c_c = 1; % Vena contraction factor set to 1 effectively removes the effect
d_jet = d_nz * c_c;
%%%%%%%%%%%%%%%%%%%%%%%%%%%%%%%%%%%%%%%%%%%%%%%%%%%%%%%%%%%%%%%%%%%%%%%%%%%%%%%
% Point 7.
%%%%%%%%%%%%%%%%%%%%%%%%%%%%%%%%%%%%%%%%%%%%%%%%%%%%%%%%%%%%%%%%%%%%%%%%%%%%%%%
A_7 = d_jet^2/4*pi;
P_7 = P_atm;
% The initial guess of the jet velocity is equal to the vessel velocity
V_7 = U;

% Iterative solver of the required jet velocity and the mass flow rate.
it = 0;
T_it = T;
error = 100*ones(size(V_7));
m_dot = ones(size(T));
```

```
V_1 = zeros(size(T));
m_dot_stf = ones(size(T));
A_stf= ones(size(T));
A_st= ones(size(T));
delta_st= zeros(size(T));
tic
for i = 1:length(V_7)
    disp('velocity')
    disp(Vk(i))

    if i == length(V_7)
        V_1(i) = 0;
        V_7(i) = sqrt(T(i)/(rho*A_7));
        m_dot(i) = rho * A_7*V_7(i);
        disp('test')


    else

        while error(i) >0.1%T(i)/1000
            it = it +1;
            V_7(i) = V_7(i) +0.001;

            m_dot(i) = rho * A_7*V_7(i);

            %Evaluation of the stream tube size and average velocity...
            %as it is dependent of the mass flow in the pipe.
            % ergo it is dependet on the thrust of the system.
                m_dot_stf(i) = (m_dot(i) - m_dot_stdelta(i));
                A_stf(i) = m_dot_stf(i)./(rho *U(i));
                A_st(i) = A_stf(i) + A_delta(i);
                delta_st(i) = A_stf(i)/r_st;
                V_1(i) = m_dot(i)./(rho*A_st(i));
            T_it(i,1) = m_dot(i) *(V_7(i)-V_1(i));
            error(i) = T(i)-T_it(i);
        end
    end

    disp(it)
    it = 0;

end
toc
Q_dot = m_dot/rho;

V_6 = m_dot./(rho*A_nz);



%%%%%%%%%%%%%%%%%%%%%%%%%%%%%%%%%%%%%%%%%%%%%%%%%%%%%%%%%%%%%%%%%%%%%%%%%%%%%%%
% Point 5. 4. 3. & 2.  Velocity in the pipe and through the pump.
%%%%%%%%%%%%%%%%%%%%%%%%%%%%%%%%%%%%%%%%%%%%%%%%%%%%%%%%%%%%%%%%%%%%%%%%%%%%%%%
V_3 = m_dot./(rho*A_pipe);
```

```
V_3_shaft = m_dot./(rho*(A_pipe-0.03^2*pi));
V_diff = V_3_shaft(tab_index)-V_3(tab_index)
V_4 = V_3;
V_5 = V_4;
V_2 = V_3;


%%%%%%%%%%%%%%%%%%%%%%%%%%%%%%%%%%%%%%%%%%%%%%%%%%%%%%%%%%%%%%%%%%%%%%%%%%%%%%%
% Pressure losses - Leads to determination of pressure before pump.
%%%%%%%%%%%%%%%%%%%%%%%%%%%%%%%%%%%%%%%%%%%%%%%%%%%%%%%%%%%%%%%%%%%%%%%%%%%%%%%
% Goal - energy equation from 1 to 7 including the pressure losses.

%%%%%%%%%%%%%%%%%%%%%%%%%%%%%%%%%%%%%%%%%%%%%%%%%%%%%%%%%%%%%%%%%%%%%%%%%%%%%%%
% Inlet
%%%%%%%%%%%%%%%%%%%%%%%%%%%%%%%%%%%%%%%%%%%%%%%%%%%%%%%%%%%%%%%%%%%%%%%%%%%%%%%
% The velocity ratio between the stream tube and the duct.
lambda = V_1./V_3;
%Inlet loss factor - See CFR-62.pdf page 12-ish
          grid_loss = 0.05; % Suggested grid loss from Reima - see email.
xi = XXXXXXXXXXXXXXXXXXXXXXXXXXXXXXXXXXXXXXXX; %IP of Rolls-Royce

%The pressure at point 3 is estimated using equation 2, 3 and 4 from
%CFR-62.pdf (internal Rolls-Royce Document.
E1 = (1/2*rho*V_1.^2).*Q_dot; %Energy input to the system

%E_3 found using equation 2.
E3 = E1-xi*1/2*rho.*Q_dot.*V_3.^2; % /V_1 taken out of the equation
dE = E1-E3;
H_inlet = dE./(m_dot*g);

%%%%%%%%%%%%%%%%%%%%%%%%%%%%%%%%%%%%%%%%%%%%%%%%%%%%%%%%%%%%%%%%%%%%%%%%%%%%%%%
% Reynolds number
%%%%%%%%%%%%%%%%%%%%%%%%%%%%%%%%%%%%%%%%%%%%%%%%%%%%%%%%%%%%%%%%%%%%%%%%%%%%%%%
% Using formular 6-54 from advanced fluid mechanics and Darcy-Weisbach
% equation - see introduction to fluid mechanics eq. 8.34.
% Reynolds number in pipe - from page 426 advanced fluid mechanics
Re = d_imp * V_3 ./ nu; % The flow is turbulent.


%%%%%%%%%%%%%%%%%%%%%%%%%%%%%%%%%%%%%%%%%%%%%%%%%%%%%%%%%%%%%%%%%%%%%%%%%%%%%%%
%Nozzle elevation head loss as a function ofthe vessel speed.
%%%%%%%%%%%%%%%%%%%%%%%%%%%%%%%%%%%%%%%%%%%%%%%%%%%%%%%%%%%%%%%%%%%%%%%%%%%%%%%
hz = rho*g*z;
Hz = z-draft;
Hz(find(Hz<0)) = 0;
% The elevation of the nozzle is assumed
% zero when the nozzle is below water level



%%%%%%%%%%%%%%%%%%%%%%%%%%%%%%%%%%%%%%%%%%%%%%%%%%%%%%%%%%%%%%%%%%%%%%%%%%%%%%%
% Head Rise delivered by pump.
```

```
%%%%%%%%%%%%%%%%%%%%%%%%%%%%%%%%%%%%%%%%%%%%%%%%%%%%%%%%%%%%%%%%%%%%%%%%%%%%%%%%

% The amount of energy transfered to the water that results in a head rise.
H_duct = H_inlet  ;
% H_duct = zeros(size(Hsf));
%P_3 found using the energy equation
 P_3 =(E1./Q_dot + P_1) - 1/2*rho*V_3.^2 - (H_duct + Hz)*rho*g;

%equation 2.2  from main.pdf ---- eqution 16.3 Carlton:2007
% H_ideal = (V_7.^2-V_1.^2)/(2*g) + Hz+ H_duct;
H_ideal = ((P_7 + 1/2*rho*V_7.^2) - (P_3 + 1/2*rho*V_3.^2))/(g*rho);
H_loss = H_duct-Hz;




%%%%%%%%%%%%%%%%%%%%%%%%%%%%%%%%%%%%%%%%%%%%%%%%%%%%%%%%%%%%%%%%%%%%%%%%%%%%%%%%
% Power needed to produce thrust.
%%%%%%%%%%%%%%%%%%%%%%%%%%%%%%%%%%%%%%%%%%%%%%%%%%%%%%%%%%%%%%%%%%%%%%%%%%%%%%%%

P_ideal = m_dot.*g.*H_ideal./1000; %[kW]
% Work done by the waterjet.
W = T.* V_1./1000;

omega = rpm/60*2*pi;
P_engine = 132*omega/1000;
P_diff = P_engine - P_ideal

E_input_min = ((P_7 + 1/2*rho*V_7.^2) - (P_3 + 1/2*rho*V_3.^2)) .* Q_dot;
tau_min = E_input_min/omega;
%%%%%%%%%%%%%%%%%%%%%%%%%%%%%%%%%%%%%%%%%%%%%%%%%%%%%%%%%%%%%%%%%%%%%%%%%%%%%%%%
% Turbo Design input
%%%%%%%%%%%%%%%%%%%%%%%%%%%%%%%%%%%%%%%%%%%%%%%%%%%%%%%%%%%%%%%%%%%%%%%%%%%%%%%%

Q = m_dot/rho;
d_hub = 0.06; %60 mm
A_hub = d_hub^2/4*pi;
Q_design = Q/A_pipe *(A_pipe -A_hub);


Uref = omega*d_imp/2;
Uref2 = 20.562;
rVt = H_ideal/(Uref^2/g);
rVt2 = H_ideal/(Uref2^2/g);
disp([Vk(tab_index) V_3(tab_index)])
% Propulsion efficiency


eta_propulsion = W./P_ideal;

%Specific speed of the pump
N = omega * Q.^(1/2)./(g * H_ideal);
disp(N(tab_index(5)))
```

```
% Norndimensianaised flow rate.
Qe = Q/(rpm/100*d_imp^3);

%%
%%%%%%%%%%%%%%%%%%%%%%%%%%%%%%%%%%%%%%%%%%%%%%%%%%%%%%%%%%%%%%%%%%%%%%%%%%%%%%%%
%                          Production of output file                            %
%%%%%%%%%%%%%%%%%%%%%%%%%%%%%%%%%%%%%%%%%%%%%%%%%%%%%%%%%%%%%%%%%%%%%%%%%%%%%%%%

disp('Printing table to file')
fileName = strcat('/home/results_math_v3.txt');
    fileID = fopen(fileName,'w');
for i = tab_index
    fprintf(fileID,'%3.0f %3.2f %3.2f %3.2f %3.2f  %3.2f %3.2f %3.2f\n'...
        ,Vk(i),V_1(i),V_3(i),V_7(i),P_3(i),Q(i),H_ideal(i),Qe(i));
end
    fclose(fileID);




%%
%%%%%%%%%%%%%%%%%%%%%%%%%%%%%%%%%%%%%%%%%%%%%%%%%%%%%%%%%%%%%%%%%%%%%%%%%%%%%%%%
%                          Production of output file                            %
%%%%%%%%%%%%%%%%%%%%%%%%%%%%%%%%%%%%%%%%%%%%%%%%%%%%%%%%%%%%%%%%%%%%%%%%%%%%%%%%

disp('Printing table to file')
fileName = strcat('/hometable_input_v3.tex');  % NAME OF txt file is defined here.
    fileID = fopen(fileName,'w');
fprintf(fileID,'\\begin{table}[!ht] \n');
fprintf(fileID,'\\centering \n');
fprintf(fileID,...
    '\\caption{\\textit{The operational points of the pump.}}\n');
fprintf(fileID,'\\begin{tabular}{ccc} \n'); % Defininf the table dimensions
fprintf(fileID,'\\hline \n');
fprintf(fileID,...
    'Vessel speed ($V_0$)& Vessel speed ($V_0$)& Thrust predicted\\\\ \n');
fprintf(fileID,'$[\\si{knots}]$ & [$\\si{m/s}$] & [kN] \\\\\n');
fprintf(fileID,'\\hline\n');
for i = tab_index
    fprintf(fileID,'%3.0f & %3.2f & %3.2f\\\\ \n',Vk(i),U(i),T(i)/1000);
end
fprintf(fileID,'\\hline \n');
fprintf(fileID,'\\hline \n');
 fprintf(fileID,'\\end{tabular} \n');
 fprintf(fileID,'\\label{tab:math_in} \n'); % THE LABEL
 fprintf(fileID,'\\end{table}  \n');
    fclose(fileID);
%  edit '/home/thor/Documents/Master Thesis/Thesis Report/table_input.tex'


figure()
```

```
bar(Qe(tab_index), H_ideal(tab_index),0.5,'stacked','w','EdgeColor','black')
hold on
bar(Qe(tab_index), H_duct(tab_index),0.5,'stacked','w','EdgeColor','blue')
bar(Qe(tab_index), Hz(tab_index),0.5,'stacked','w','EdgeColor','red')
xlim([1.07 1.33])
xlabel('Flow rate factor (Qe) [-]','Interpreter','latex')
ylabel('Head rise [m]','Interpreter','latex')
set(gcf, 'Position', [100 100 800 400], 'Color', 'w')
 set(findall(gcf,'type','text'),'FontSize',20,'fontWeight','bold')
 legend('Thrust', 'Duct loss', 'Elevation')
 %Printing the eps file to figure folder.
```

This page is intentionally left blank.

C Meshing Settings

The setting used in Ansys model maker to create the computational grid used for the CFD modelling are displayed in figure C.1, C.2 and C.3.

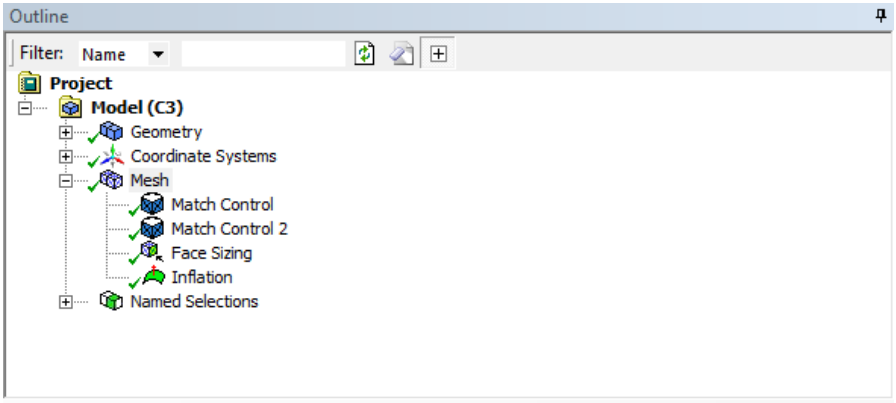

Details of "Mesh"

Defaults	
Physics Preference	CFD
Solver Preference	Fluent
Relevance	0
Sizing	
Use Advanced Size Fun...	On: Curvature
Relevance Center	Coarse
Initial Size Seed	Active Assembly
Smoothing	Medium
Transition	Slow
Span Angle Center	Fine
Curvature Normal A...	12.0 °
Min Size	0.13030 mm
Max Face Size	2.88430 mm
Max Size	26.070 mm
Growth Rate	1.20
Minimum Edge Length	0.17370 mm
Inflation	
Assembly Meshing	
Method	None
Patch Conforming Options	
Triangle Surface Mesher	Program Controlled
Advanced	
Defeaturing	
Statistics	

Figure C.1: Grid settings for the general mesh sizing.

Details of "Inflation" - Inflation	
Scope	
Scoping Method	Geometry Selection
Geometry	1 Body
Definition	
Suppressed	No
Boundary Scoping Method	Named Selections
Boundary	Multiple Entities
Inflation Option	First Layer Thickness
First Layer Height	0.1 mm
Maximum Layers	8
Growth Rate	1.2
Inflation Algorithm	Pre

Figure C.2: Grid settings for the inflation layer.

Details of "Face Sizing" - Sizing	
Scope	
Scoping Method	Named Selection
Named Selection	rotor-blade
Definition	
Suppressed	No
Type	Element Size
Element Size	3. mm
Behavior	Soft
Curvature Normal Angle	Default
Growth Rate	Default

Figure C.3: Grid settings for the face sizing on the blade.

This page is intentionally left blank.

D CFD Convergence Study

The convergence study is presented in the following table and figures. Note that the study of convergence of the transient analysis is plotted with the number of time steps the convergence study is based on (figure D.4). The actual number of time steps vary as the convergence is much faster reached by the higher flow rates.

Table D.1: The standard deviation as permille of the mean torque value, see figure D.1

Case 1.										
Volume flow (Q_e)	[-]	1.09	1.11	1.13	1.16	1.18	1.21	1.24	1.27	1.30
Standard deviation	‰	0.21	0.15	0.01	0.01	0.04	0.03	0.36	0.91	0.61
Case 2.										
Volume flow (Q_e)	[-]	1.03	1.11	1.13	1.16	1.18	1.21	1.24	1.27	1.30
Standard deviation	‰	0.01	0.01	0.01	0.01	0.01	0.01	0.01	0.67	2.55
Case 3.										
Volume flow (Q_e)	[-]	1.10	1.11	1.13	1.16	1.18	1.21	1.24	1.27	1.30
Standard deviation	‰	0.01	0.01	0.04	0.03	0.03	0.06	0.04	0.02	0.02
Case 1.										
- Transient										
Volume flow (Q_e)	[-]	1.09	1.11	1.13	1.16	1.18	1.21	1.24	1.27	1.30
Standard deviation	‰	2.43	1.59	0.40	0.52	0.46	0.40	0.35	0.35	0.31
Case 1.										
- Cavitation										
Volume flow (Q_e)	[-]	1.09	1.27							
Standard deviation	‰	0.17	0.28							

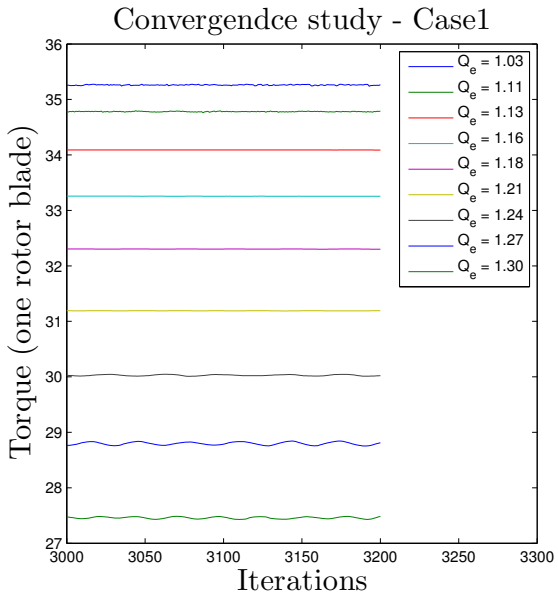

Figure D.1: Plot of convergence study of Case 1. It is clear from the figure that the torque of the system is constant with minor fluctuations.

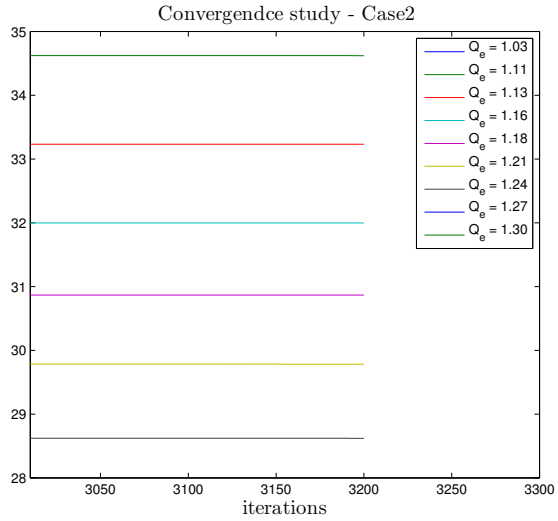

Figure D.2: Plot of convergence study of Case 2. It is clear from the figure that the torque of the system is constant with minor fluctuations.

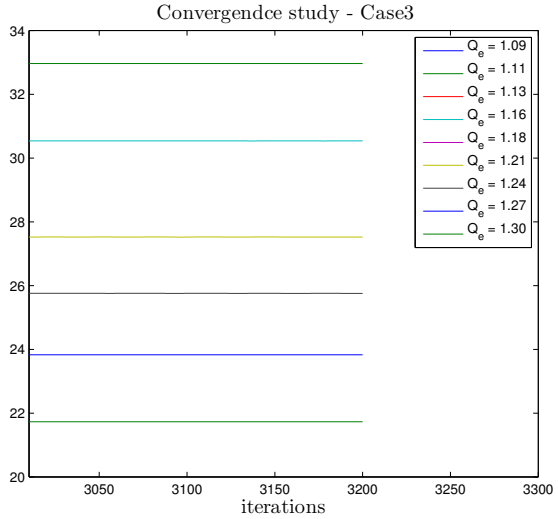

Figure D.3: Plot of convergence study of Case 3. It is clear from the figure that the torque of the system is constant with minor fluctuations.

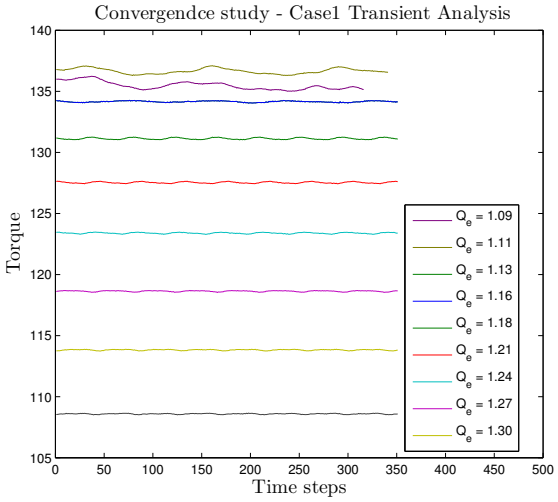

Figure D.4: Plot of convergence study of Case 1. transient analysis. The x-axis displays the time steps the study is based on. The actual number of time steps is displayed in table D.2

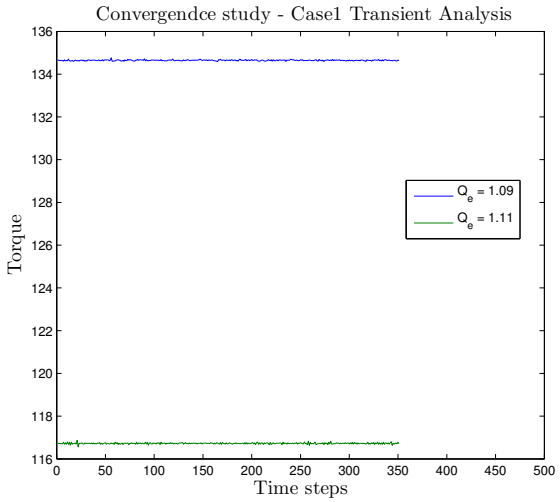

Figure D.5: Plot of convergence study of Case 1. transient cavitation analysis. Note that the $Q_e = 1.09$ condition is not converged fully.

Table D.2: The number of time steps used for each transient analysis.

Transient - Time steps	
Flow rate	No. Time step
$Q_e = 1.09$	4110
$Q_e = 1.11$	3604
$Q_e = 1.13$	1943
$Q_e = 1.16$	2548
$Q_e = 1.18$	780
$Q_e = 1.21$	530
$Q_e = 1.24$	1247
$Q_e = 1.27$	1157
$Q_e = 1.30$	1247